EXCESS ARGON ($^{40}Ar_E$) IN MELT INCLUSION BEARING QUARTZ AND SANIDINE FROM THE BISHOP AND BANDELIER TUFFS

by

Jeffrey A. Winick

Submitted in Partial Fulfillment of the Requirements of the Degree of

Masters of Science in Geochemistry

October 2000

Department of Earth and Environmental Science

New Mexico Institute of Mining and Technology

Socorro, New Mexico, USA

ABSTRACT

$^{40}Ar/^{39}Ar$ experiments on melt inclusion bearing quartz (MIBQ) from the Bishop and Bandelier plinian pyroclastic fall deposits indicate high concentrations of excess argon ($^{40}Ar_E$) in trapped melt inclusions. Two rhyolite-glass melt-inclusion populations are present in quartz: exposed melt inclusions (EMI) and trapped melt inclusions (TMI). Air-abrasion mill grinding and hydrofluoric acid treatments progressively remove EMI while leaving TMI unaffected. Laser step-heating of MIBQ yields apparent ages which increase with progressive removal of EMI, providing evidence of high $^{40}Ar_E$ concentrations hosted in TMI. TMI-only quartz from the Bishop Tuff yield a total gas age of 3.70 ± 1.00 Ma. Total gas ages for similar TMI-only MIBQ from the Upper and Lower Bandelier Tuffs are 11.54 ± 0.87 Ma and 14.60 ± 1.50 Ma respectively. Single-crystal laser-fusion analyses of MIBQ represent mixtures of EMI and TMI argon reservoirs, yielding spuriously old ages that are significantly older than any crystallization or eruption event in the Bishop and Bandelier magma systems determined from Rb/Sr and ε_{Nd} isotopic data, but are younger than apparent ages of TMI.

Single-crystal laser-fusion $^{40}Ar/^{39}Ar$ analyses of sanidine from the Bishop, Upper Bandelier and Lower Bandelier Tuff plinian deposits yield weighted mean ages of 0.768 ± 0.004 Ma, 1.294 ± 0.010 Ma, and 1.607 ± 0.011 Ma respectively. The Bishop Tuff and Lower Bandelier Tuff weighted mean ages presented here are consistent with previously published $^{40}Ar/^{39}Ar$ single-crystal laser-fusion sanidine apparent ages (0.772 ± 0.010 Ma

and 1.629 ± 0.022 Ma respectively; Izett and Obradovich, 1994). However, sanidine from the Upper Bandelier Tuff plinian deposit displays a weighted mean age that is both imprecise and ~20 ka older than previously determined $^{40}Ar/^{39}Ar$ ages for this deposit (1.235 ± 0.032 Ma; Izett and Obradovich, 1994). Trapped melt inclusions in Bishop and Bandelier sanidine phenocrysts may contain $^{40}Ar_E$ concentrations similar to those in MIBQ. Models based on $^{40}Ar_E$ concentrations in MIBQ, observed trapped melt inclusion abundances in sanidines, and published single-crystal laser-fusion sanidine data show that as a result of $^{40}Ar_E$, sanidine apparent ages of the Bishop, Upper Bandelier, and Lower Bandelier Tuff plinian deposits can be increased by 4 k.y., 38 k.y., and 27 k.y. respectively. The modeling results are consistent with the presented $^{40}Ar/^{39}Ar$ single-crystal laser-fusion sanidine age data and suggest that apparent $^{40}Ar/^{39}Ar$ ages of young sanidines (<100 ka) are particularly sensitive to $^{40}Ar_E$.

ACKNOWLEDGEMENTS

This manuscript would not have been possible without the countless hours of help and seemingly endless patience of the people at the New Mexico Geochronology Research Laboratory and the New Mexico Bureau of Mines and Mineral Resources. In particular, I wish to thank my advisors Bill McIntosh and Nelia Dunbar whose friendship and guidance have been invaluable to me and who allowed this project to evolve on my terms while managing to keep me on track. Many thanks are also due to Rich Esser and Lisa Peters who took an interest in this project and were always willing to help, as well as to Matt Heizler for his sharing his objectivity, ideas, and insightful discussions regarding excess argon. I would also like to thank Phil Kyle for his time and guidance and for providing me with the volcanological background that helped me to more fully understand the implications of my data. Last but certainly not least, I am grateful to Jeremy Boyce and the people at UCLA (Marty Grove and Oscar Lovera) for their diffusion data on melt inclusion bearing quartz, as well as for providing a stimulating and productive discourse on the implications of excess argon in melt inclusion bearing quartz.

TABLE OF CONTENTS

LIST OF FIGURES

LIST OF TABLES

LIST OF APPENDICES

This Thesis is accepted on behalf of the faculty
of the Institute by the following committee:

William C McIntosh

Academic Adviser

William C McIntosh

Research Advisor

Nelia W. Dunbar

Committee Member

Philip R Kyle

Committee Member

Committee Member

10/17/00

Date

CHAPTER 1. INTRODUCTION

Isotopic data from the eruptive products of high-silica rhyolite magma systems can offer insights into their crustal residence times. The 0.772 ± 0.010 Ma Bishop Tuff in Long Valley, California, and the Upper (1.235 ± 0.032 Ma) and Lower (1.629 ± 0.022 Ma) Bandelier Tuffs of the Jemez Mountains in New Mexico were erupted from two such magma systems, which have been the subject of numerous isotopic studies (Hildreth, 1979; Izett and Obradovich, 1994; Self et al., 1996; Davies and Halliday, 1998; Wolff et al., 1999). These two magma systems are similar in age, chemical composition, and volume, but differ in many isotopic aspects; they are therefore well suited to a comparative study of melt-inclusion-hosted argon isotopes.

The residence time of the Bishop Tuff magma chamber has been a subject of much debate (van den Bogaard and Schirnick, 1995; Davies and Halliday, 1998, and references therein; Reid and Coath, 2000). A $^{40}Ar/^{39}Ar$ single-crystal laser-fusion study yielded an isochron age of 1.93 ± 0.12 Ma for melt inclusion bearing quartz (MIBQ) phenocrysts of the Bishop Tuff plinian pumice (van den Bogaard and Schirnick, 1995). This $^{40}Ar/^{39}Ar$ age agrees closely with Rb/Sr model ages of similar MIBQ (1.9 ± 0.3 Ma; Christensen and Halliday, 1996). These ages have been interpreted as a record of a ~2 Ma differentiation event in parts of the Bishop Tuff magma chamber, necessitating a long-lived (>1 m.y.) magma body prior to eruption at 0.76 Ma.

A residence time of >1 m.y. is difficult to reconcile with isotopic and thermal modeling (Huppert and Sparks, 1988; Christensen and DePaolo, 1993). Differences in ε_{Nd} values between the 2.1 to 0.79 Ma pre-caldera rhyolites of Glass Mountain and the Bishop Tuff have been interpreted to imply a maximum residence time of ~0.5 Ma for the Bishop Tuff magma chamber (Halliday et al., 1989). This residence time is consistent with that determined by modeling Sr isotopic disequilibrium between Bishop Tuff sanidine and glass (Christensen and DePaolo, 1993; Davies and Halliday, 1998). Reid and Coath (2000) show that zircon was a liquidus phase throughout crystallization of the Bishop Tuff magma chamber. Plinian and early ignimbrite zircon interiors record a U-Pb age of 0.823 ± 0.011 Ma, suggesting that the Bishop Tuff magma chamber erupted shortly (<100 k.y) after it began to crystallize.

Because the data of van den Bogaard and Schirnick (1995) display well defined isochrons with $^{40}Ar/^{36}Ar$ intercepts of an atmospheric composition, they interpreted MIBQ apparent ages as representative of closed system behavior with respect to radiogenic argon at magmatic temperatures. This interpretation led van den Bogaard and Schirnick (1995) to conclude that the apparent ages of MIBQ reflect the age of a crystallization event in the Bishop Tuff magma chamber. Major and trace element compositions in quartz melt inclusions from both the Bishop and Bandelier Tuff plinian deposits are identical to those in their host matrix pumice (Dunbar and Hervig, 1992a,b), suggesting that little magmatic differentiation occurred after quartz crystallization. This indicates that MIBQ may have been in equilibrium with the surrounding melt. Quantitative electron microprobe analyses of MIBQ are presented here that are consistent with those of Dunbar and Hervig (1992a,b). While these data alone do not demand argon isotopic equilibrium, recent diffusion data suggests that MIBQ are non-retentive of argon at magmatic temperatures and should not record closed system behavior of radiogenic argon (Boyce et al., 2000).

Two populations of rhyolite glass have been recognized in MIBQ and are potential hosts of excess argon ($^{40}Ar_E$): 1) trapped melt inclusions (TMI) contained completely within quartz phenocrysts; and 2) exposed melt inclusions (EMI), consisting of hourglass inclusions that are connected by narrow necks to non-vesicular glass on the exterior of quartz (Fig. 1). For a complete description of MIBQ from rhyolite, see Anderson (1991).

Presented here are new $^{40}Ar/^{39}Ar$ data on plinian MIBQ from the Bishop and Bandelier Tuffs. These data indicate that TMI and EMI represent distinct argon reservoirs formed upon eruptive depressurization and degassing of MIBQ. Treatment of MIBQ with an air-abrasion mill (Goldich and Fischer, 1986) and hydrofluoric acid removes EMI, thereby isolating TMI. Analysis of these treated samples yields unreasonably old apparent ages, indicating that TMI contain substantial amounts of $^{40}Ar_E$. Step-heating and single-crystal laser-fusion analyses of minimally treated MIBQ homogenize TMI and EMI reservoirs, resulting in apparent ages that represent neither eruption nor crystallization events.

Compositionally identical trapped melt inclusions hosted in sanidines of the Bishop and Bandelier Tuffs may also contain $^{40}Ar_E$. Excess argon concentrations in MIBQ TMI, trapped melt inclusion abundance in sanidines, and single-crystal laser-fusion $^{40}Ar/^{39}Ar$ sanidine analyses presented in this paper, as well as those of Izett and Obradovich (1994), are used to create a quantitative model of the potential effects that

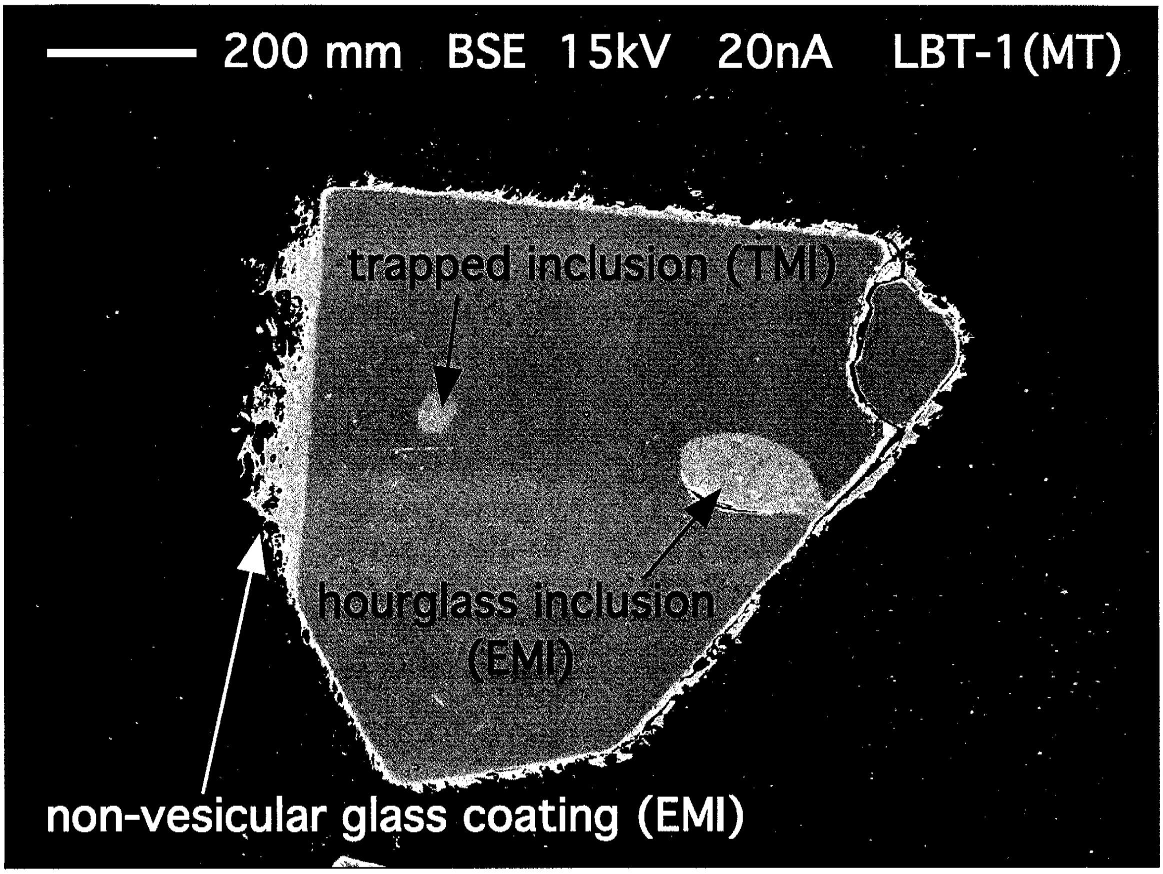

Figure 1. Backscattered electron image of a minimally treated MIBQ crystal. Crystal exhibits two populations of rhyolite glass that are potential hosts of excess argon (see text).

trapped melt inclusion-hosted-$^{40}Ar_E$ can have on single-crystal laser-fusion sanidine analyses. The modeled data suggest that $^{40}Ar_E$ in trapped melt inclusions may increase apparent ages of Bishop, Upper Bandelier, and Lower Bandelier Tuff plinian sanidines by as much as 4 k.y., 38 k.y, and 27 k.y. respectively. Furthermore, as a function of randomly distributed trapped melt inclusion abundances and their respective $^{40}Ar_E$ concentrations, modeled populations of sanidine display increased scatter of apparent age among individual analyses of the analytical population. Moreover, these individual sanidine analyses tend toward older apparent ages as a result of $^{40}Ar_E$. Depending on $^{40}Ar_E$ concentrations, the sum of $^{40}Ar_E$-induced apparent age effects on a population of sanidines is to both increase the weighted-mean apparent age of that population and to yield uncertainties on the weighted-mean apparent age that may or may not be statistically distinct from analytical error on an otherwise melt-inclusion-free (and $^{40}Ar_E$-free) population of sanidines. For young sanidines (<100 ka) in particular, increased uncertainties on a weighted-mean apparent age (due to $^{40}Ar_E$-laden trapped melt inclusions) can comprise a significant percentage of a true eruption age. The potential for $^{40}Ar_E$ to affect $^{40}Ar/^{39}Ar$ analyses of young sanidine holds important implications for a variety of applications of the $^{40}Ar/^{39}Ar$ dating method.

CHAPTER 2. BACKGROUND

2.1. Geologic Setting

The Bandelier and Bishop Tuffs are found in the Jemez Mountains Volcanic Field and the Long Valley Volcanic Field respectively (Figs. 2 and 3). Both volcanic fields are located in extensional tectonic regimes: i.e., the Long Valley Volcanic Field lies on the western-most margin of the Basin and Range province and the Jemez Mountains Volcanic Field straddles the western edge of the Rio Grande Rift in northern New Mexico (Fig. 4).

2.1.1. The Rio Grande Rift and the Jemez Mountains

The Rio Grande Rift physiographic province stretches from Leadville, Colorado at its most northern extent, into New Mexico; where it bifurcates near Socorro, and then merges with the Basin and Range province further south (Fig. 4). The rift is characterized by a series of en-echelon, north-northeast trending structural basins which separate the Colorado plateau on the west from the stable interior craton on the east (Cather et al., 1994; Chapin and Cather, 1994). Extension within the Rio Grande rift occurred in two main episodes: a late Oligocene phase of punctuated deformation that produced accumulations of silicic volcanics and volcaniclastic sediments within narrow half grabens; and a late Miocene episode of strong regional deformation responsible for producing the topography seen in the Rio Grande Rift today (Cather et al., 1994).

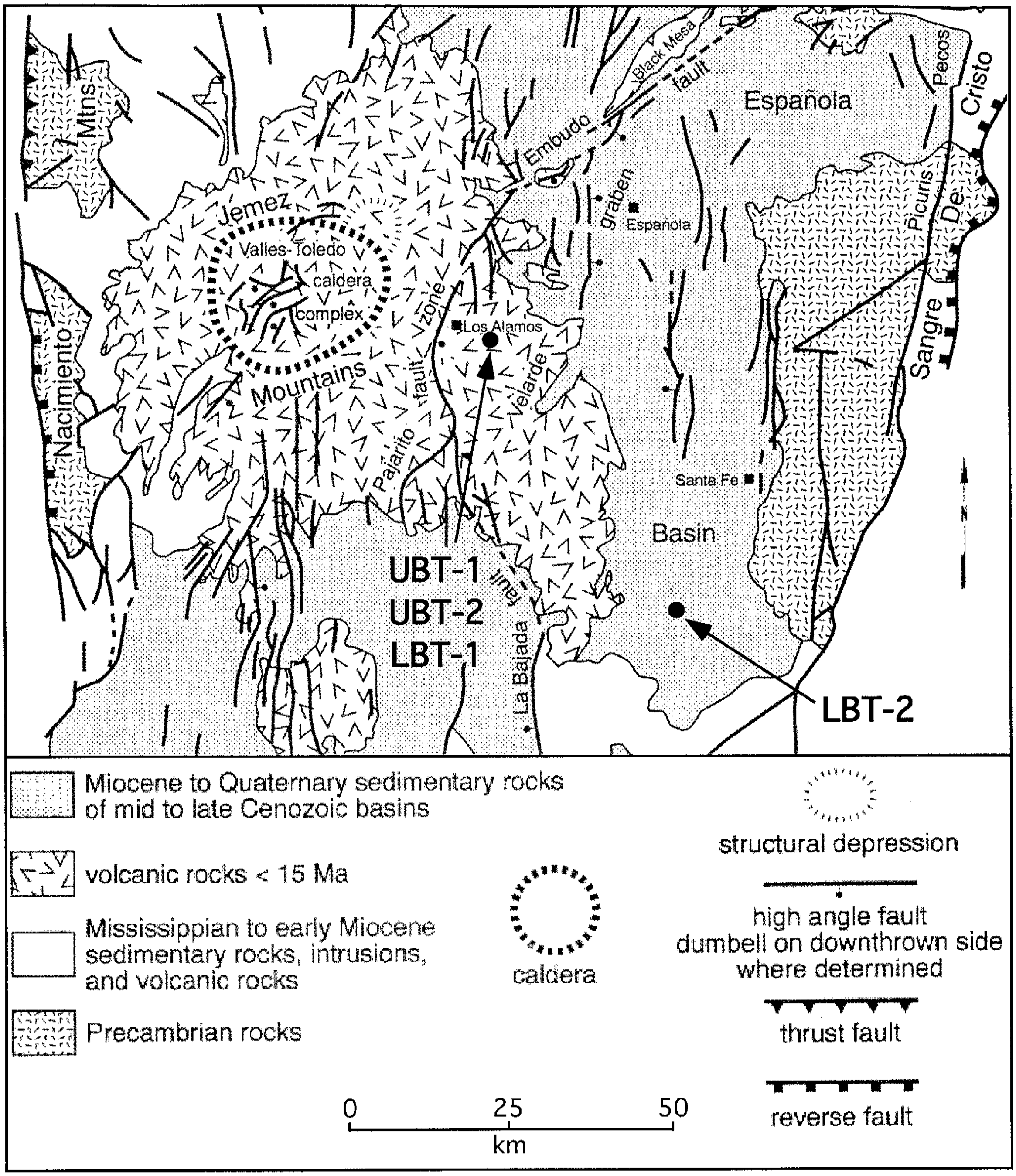

Figure 2. Map of the distribution of late Tertiary volcanic rocks in the Jemez Mountains Volcanic Field, northern New Mexico (after Self et al., 1996). The respective sources of the Upper and Lower Bandelier Tuffs are the nested caldera complexes of the Valles and Toledo calderas, indicated by a thick dashed ellipse. Sample locations of plinian fall deposits from the Upper and Lower Bandelier Tuffs are indicated on map.

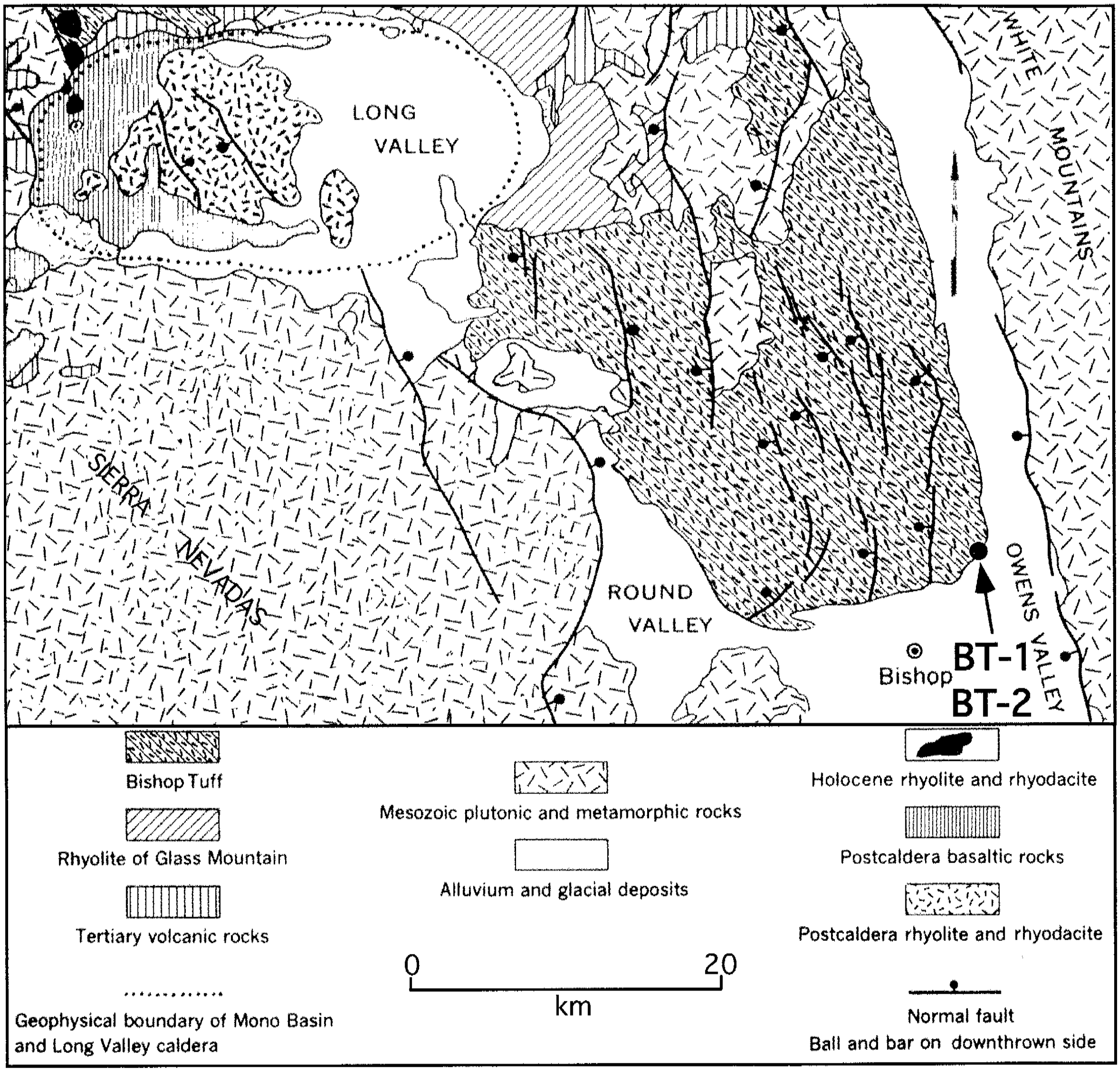

Figure 3. Map of the distribution of Pliocene to Holocene volcanic rocks in the Long Valley Volcanic Field, eastern California (after Bailey et al., 1989). The source of the 500 km^3 Bishop Tuff is the Long Valley caldera, indicated by dashed ellipse. The 2.1 to 0.79 Ma pre-caldera rhyolites of Glass Mountain are located on the northeastern edge of the Long Valley caldera. Sample locations of plinian fall deposits from the Bishop Tuff are indicated on map.

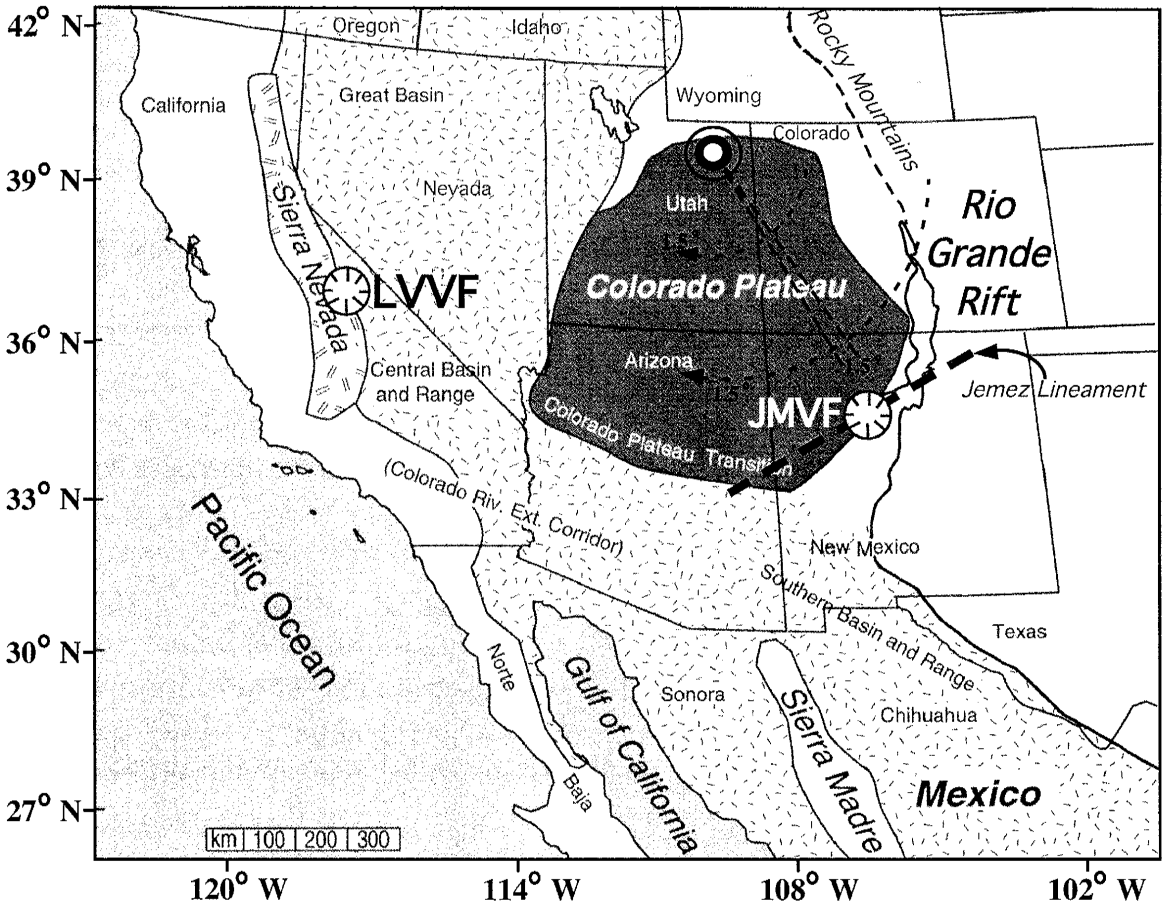

Figure 4. Map of the western United States showing major physiographic provinces (after Parsons, 1995). The Long Valley Volcanic Field (LVVF) and the Jemez Mountains Volcanic Fields (JMVF) are indicated. The Colorado plateau is shown with its Euler pole of rotation fixed in northeastern Utah (Chapin and Cather, 1994). A clockwise rotation of the Colorado plateau in the Miocene played a major role in the formation of the Rio Grande Rift and Jemez Lineament (both indicated on map). The Jemez Mountains Volcanic Field is located at the intersection of the Rio Grande Rift and the Jemez Lineament. The westernmost margin of the Basin and Range Province is the site of major range-front faults of the Sierra Nevadas. Tectonic stresses associated with this faulting may have helped to allow magma to reach shallow levels in the Long Valley Volcanic Field.

Late Oligocene extension in the Rio Grande Rift was coeval with subduction of the East Pacific Rise and initiation of San Andreas transform motion (Atwater and Stock, 1998; Atwater, 1970). The dextral shear stresses associated with these major plate tectonic events propagated deep into the southwestern United States continental lithosphere causing it to act as a series of deformable schollen (Livaccari, 1979). The result is a region of pull-apart basins termed the Basin and Range province (Fig. 4). In partial response to these stresses during Miocene times, the Colorado Plateau experienced a 1.0 to 1.5° clockwise rotation causing it to separate from the stable interior craton of the United States, and creating the Rio Grande Rift in its wake. This movement occurred about an Euler pole of rotation fixed in northeastern Utah (Chapin and Cather, 1994). Strain associated with this rotation is manifested as structural accommodation zones that lie on small circles about the Miocene Euler pole and define the margins of several structural basins in the Rio Grande Rift (Fig. 4; Chapin and Cather, 1994).

Miocene extension in the Rio Grande Rift and rotation of the Colorado Plateau is responsible for the development of a broad transition zone adjacent to the plateau's southern and southeastern margins (Baldridge et al., 1995; Parsons, 1995). This transition zone is characterized by northeast trending normal faults and is separated from the less deformed and more central regions of the Colorado Plateau by a linear array of late Tertiary volcanic fields. Together, these volcanic fields define what is often referred to as the Jemez lineament (Fig. 4). Roughly coincident with the Jemez lineament is a northeast-southwest trending zone of structural weakness in the continental lithosphere. While there is no obvious upper-crustal structure or surficial expression, such as a fracture zone, that would necessarily correspond to this zone of crustal weakness, it is believed to strongly influence the magmatic evolution along the Jemez lineament (Baldridge et al., 1995). Among the numerous volcanic centers that trace the Jemez lineament are the: White Mountains, Mt. Taylor, Jemez Mountains, Taos Plateau, Ocate, and the Raton-Clayton volcanic fields.

The Jemez Mountains Volcanic Field is located at the intersection of the Jemez lineament and the Rio Grande Rift. This province was a center of intense volcanism from the middle Miocene to the latest Pleistocene (Figs. 2 and 4). A complete overview of the volcanic development of the Jemez Mountains Volcanic Field can be found in Self et al. (1996). Although magmatism in the Jemez Mountains has been long lived and compositionally diverse since ~15 Ma, by far the largest and most explosive volcanological events to have occurred in this province were the 1.629 ± 0.022 Ma and the 1.235 ± 0.032 Ma eruptions of the Upper and Lower Bandelier Tuffs respectively (Izett and Obradovich, 1994). Together these events represent the extrusion of ~650 km^3 dense rock equivalent (DRE) of high-silica rhyolite (Self et al., 1996). The basal pyroclastic fall deposits from eruptions similar to those of the Bandelier Tuffs were deposited out of a plinian eruption column (Fisher and Schminke, 1984) and are referred to throughout this manuscript as "plinian deposits."

The Valles and Toledo nested calderas of the Jemez Mountains Volcanic Field (Fig. 2) are the respective sources of the Upper and Lower Bandelier Tuffs (Self et al., 1996 and references therein). The magma chambers which erupted to form the Upper and Lower Bandelier Tuffs resided in Proterozoic (~1.4 Ga) granites. During both eruptions, caldera subsidence occurred in a trap-door style, hinged on the western side (Nielson and Hulen, 1984). The Lower Bandelier Tuff eruption is estimated to have emplaced roughly 400 km^3 DRE of high silica rhyolite in the ignimbrite phase of the eruption, while the smaller, Upper Bandelier Tuff eruption produced an estimated 250 km^3 DRE (Stix and Gordon, 1993). Lower Bandelier Tuff plinian fall deposits exhibit dispersal axes to the east-southeast while the Upper Bandelier Tuff plinian fall deposits were dispersed largely to the northwest (Self et al., 1996; Stix and Gordon, 1993). Both eruptions are known to have dispersed ash throughout New Mexico, as well as deposits found as far east as Lubbock, Texas (Self et al., 1996; Izett et al., 1972). A detailed description of the geochemical characteristics of the Bandelier Tuffs are provided by Smith and Bailey (1966); and Dunbar and Hervig (1992 a,b).

2.1.2. The Long Valley Volcanic Field

The Long Valley Volcanic Field (Figs. 3 and 4), situated on the eastern margin of Sierra Nevadan Cretaceous granitic plutons and just north of the town of Bishop, California, has been the focus of intense Pliocene to Holocene volcanism (Bailey et al., 1989). Range front faults of the Sierra Nevadas mark the western extent of the Basin and Range physiographic province (Bierman et al., 1991). Due to their close proximity to the San Andreas transform fault system, Sierran range-front faults experience motions transitional between true Basin and Range extension and San Andreas motion. Lithospheric extension associated with these tectonic stresses has created a zone of crustal weakness which may have helped to allow magma to reach shallow levels in the Long Valley Volcanic Field (Bierman et al., 1991).

Initial volcanism in the Long Valley Volcanic Field was widespread and mafic in composition (Bailey et al., 1989). From 3.6 Ma to about 2.1 Ma, deep crustal magmatic accumulation may have become focused in an extensive, evolved, and shallow magma system which resided in Jurassic-aged granites of the Sierra Nevadas (Metz and Mahood, 1991). After 2.1 Ma, this system became the source of 2.1 to 0.79 Ma Glass Mountain Rhyolitic volcanism followed closely by the Bishop Tuff eruption at 0.772 ± 0.010 Ma (Fig. 3). This single, cataclysmic, caldera-forming eruption produced roughly 500 km^3 DRE of high silica rhyolite (Izett, 1981; Izett and Obradovich, 1994). Plinian deposits of the Bishop Tuff were dispersed largely to the east and have been found as far as Nebraska (Izett, 1981). The geochemical characteristics of the Bishop Tuff have been described in detail by Hildreth (1979).

2.2. Magma Residence Times: Insights from Radiogenic Isotopes

The generation and storage of silicic magmas that eventually erupt catastrophically, such as those of the Bishop and Bandelier magma systems, is a complex and poorly understood phenomenon. A number of models have been proposed to explain the evolution of these silicic systems (Smith, 1979; Hildreth, 1981; Huppert and Sparks, 1988, DePaolo and Perry, 1992). One fundamental difference among these models is in the upper-crustal residence times proposed for the resultant magma bodies. While no one paradigm exists to adequately explain the features of all silicic systems, two general models have gained favor over the years.

In the first model of silicic magma genesis and storage, proposed by Huppert and Sparks (1988), basaltic magma acts as a heat source for partial melting of the lower or middle crust to produce discrete and short-lived batches of evolved magma (Figs. 5A and 5B). Based on experiments using polyethylene glycol waxes to simulate countryrock and

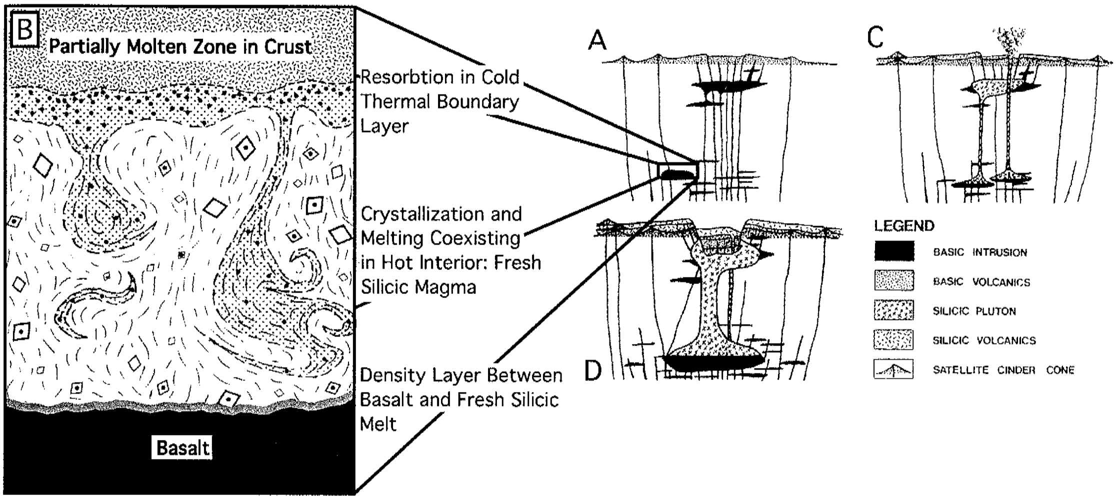

Figure 5. Cartoon model of silicic magma genesis (after Huppert and Sparks, 1988). A) Basalt intrudes lower to middle crust facilitating partial melting of large granite source lithology. B) Detail of zone of partial melting. Basalt rapidly melts granite host rock and produces liquid interior of fresh silicic magma. Both crystallization and melting processes coexist here because the extremes of hot basalt and relatively cold granite host rock bracket either side of this magma production layer. In this way, Rb/Sr isotopic data, from volcanic rocks (rhyolites in particular) of these magma systems, trace their evolutionary histories back to the host rock that partially melted to form the silicic magma (see text). C) Discrete batches of magma rise through the upper crust and are emplaced in ephemeral magma chambers. The magnitude of this mass-transport process and the subsequent residence times of the resultant larger-volume magma chambers differ here from the ideas of Hildreth (1981) and Smith (1979). Once a partially molten zone is established in the lower or middle crust, density contrasts restrict rising basalts to peripheral regions of the the volcanic field. D) Magma chambers coalesce to form a large volume of silicic magma that erupts catastrophically, similar to the Bishop and Bandelier Tuff magma systems.

aqueous solutions of different densities and temperatures to simulate magmas, Huppert and Sparks (1988) develop a theoretical paradigm in which batches of silicic magma are generated in 10^3 years.

Huppert and Sparks (1988) propose that once extensive partial melting of the lower and middle crust occurs, a zone of ductile and partially molten crust is created. Density contrasts between rising basalt and this partially molten zone eventually prohibit basic magmas from penetrating the upper crust. Huppert and Sparks (1988) point out that rapid and extensive crystallization can take place in the zone of partial melting (Fig. 5B). According to their model, crystallization need not necessarily occur in shallow magma chambers. In fact, the experimental evidence of Huppert and Sparks (1988) indicates that both partial melting and crystallization processes coexist in the lower to middle crust (Fig. 5B).

As the system evolves, the crust becomes an increasingly effective trap of basalt, causing it to pond at the base of the partially molten zone (Figs. 5C and 5D). Each new flux of basaltic magma can trigger partial melting episodes and subsequent inputs of silicic magma into the upper crust (Huppert and Sparks, 1988). These batches of magma are ephemeral and are stored in magma chambers that erupt on short timescales (10^4 years). Therefore, a direct basaltic heat source is not necessarily required for an upper crustal magma chamber to be maintained in a liquid state. Furthermore, Sparks et al. (1990) propose that evolved lavas extracted from a partially molten granitic source preserve a record of the isotopic evolutionary history of that source rock. This contrasts the ideas of Halliday et al., (1989), where such data are instead representative of the lava's isotopic evolution since the time of extraction from the partially molten zone.

Therefore, Sparks et al. (1990) propose that the presence of a long-lived, large-volume silicic magma chamber in the upper crust is unlikely and a non-essential mechanism in producing the isotopic data observed from a variety of rhyolitic systems.

Aside from the requirement of an extensive basaltic fractional crystallization mechanism, the second model of silicic magma genesis (DePaolo and Perry, 1992) shares many similarities with Huppert and Sparks (1988) in the partial melting processes that produce evolved magmas (Figs. 5A and 5B). However, the two models differ in their rates of mass transport from the partially molten zone into the upper crust, as well as in the timescales that the resultant magma chambers reside in the upper crust. This second model has evolved largely from the ideas of Hildreth (1981) that explain the zoned nature of many magma systems such as the Bishop and Bandelier Tuffs.

In order to establish such a well zoned magma system, the existence of a long-lived, large-volume, upper crustal silicic magma chamber is required. Such a magma chamber can either develop from a coalescence of smaller discrete chambers (via Huppert and Sparks, 1988), or it can result from a single-stage, massive input of silicic magma from the lower or middle crust (Hildreth, 1981). Once emplaced in the upper crust, a large volume of silicic magma can be maintained in a molten state for long periods of time (on the order of 10^5 years) by basalt ponded at its base. In response to complex thermal gradients across the magma chamber and its adjacent host-rock, layered convection cells develop in the magma chamber which facilitate chemical and isotopic differentiation (Hildreth, 1979; Hildreth, 1981). Furthermore, to achieve crystal rich and extremely evolved magmas, the bulk of crystallization and isotopic differentiation processes are restricted to the upper crustal magma chamber. This model also differs from that of Huppert and Sparks (1988) in that basalt acts as a heat source for a magma chamber, effectively keeping it molten for protracted periods of time.

This second model has gained favor in explaining the magmatic evolution of the Long Valley Volcanic Field because of an abundance of Rb/Sr and ε_{Nd} isotopic data that supports long magma residence times in the years preceding the Bishop Tuff eruption. In particular, Halliday et al., (1989) used Rb/Sr and ε_{Nd} data to deduce magma residence times of 10^5-10^6 years in the Long Valley Volcanic Field. Furthermore, Metz and Mahood (1991) pointed out that the Huppert and Sparks (1988) model has difficulty explaining extremely high Rb/Sr concentrations (>500) observed in the Bishop Tuff (Halliday et al., 1989). Multi-stage partial melting of a large granitic source, via Huppert and Sparks (1988), is incapable of producing the large volumes of Sr-depleted rhyolite in the Glass Mountain rhyolites and the Bishop Tuff (Fig. 6A). Instead, extensive fractional crystallization must be involved, which Halliday et al. (1989) interpret to imply a long residence time for the Bishop Tuff magma chamber. The following section provides a review of existing Rb/Sr and ε_{Nd} isotopic data that has been used to support long magma residence times in the Long Valley Volcanic Field.

2.2.1 Rb/Sr and ε_{Nd} evidence for long magma residence times in the Long Valley Volcanic Field

A change from early mafic volcanism to more focused and shallow silicic volcanism in the Long Valley Volcanic Field was manifested by the onset of Glass Mountain rhyolite volcanism (Fig. 3; Bailey et al., 1989). Rb/Sr and ε_{Nd} data from these pre-caldera rhyolites provide significant insight into the magmatic plumbing system

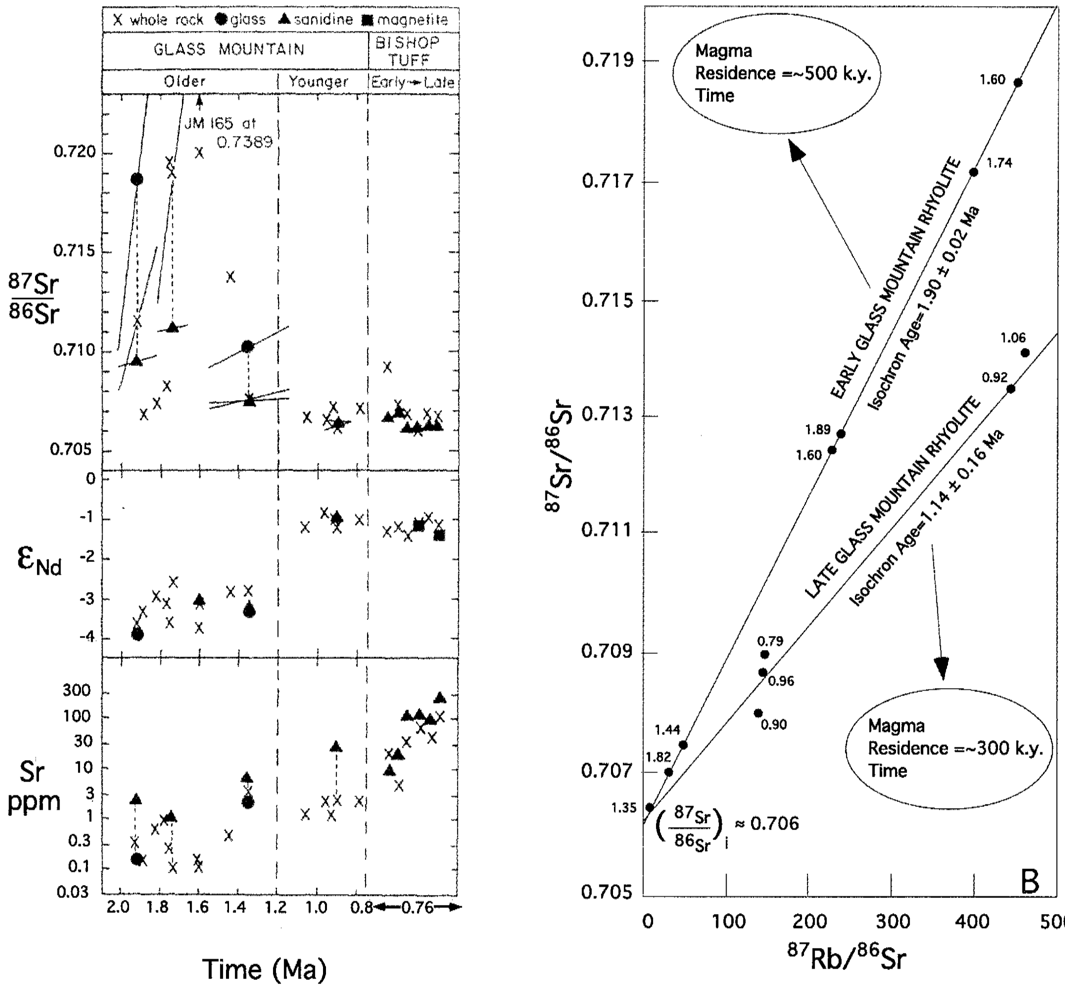

Figure 6. A) Neodymium and strontium isotopic compositions and strontium concentrations from Early and Late Glass Mountain rhyolites and Early to Late erupted Bishop Tuff. Dashed vertical lines represent samples for which mineral separates were analyzed (in addition to glass and whole rock separates). For these samples, the effect of maximum uncertainty in age on the calculated Sr isotopic compositions at the time of eruption are shown at the 1σ confidence limits. Early Glass Mountain rhyolites are isotopically and chemically distinct from Late Glass Mountain rhyolites which are in many ways similar to the Bishop Tuff (particularly early-erupted fractions). B) Rb/Sr isotopic evolution diagram showing the two isochrons formed by lavas compositionally, isotopically, and temporally associated with the Early and Late Glass Mountain rhyolites. Numbers next to data points are K/Ar eruption ages of Metz and Mahood (1995). These isochron ages have been taken as ages of major magma differentiation events that took place in the Long Valley magmatic system (Halliday et al., 1989). Diagrams modified from Halliday et al. (1989).

which evolved into the Bishop Tuff magma chamber. Chemically, isotopically, and temporally, the Glass Mountain rhyolites are divided into two groups. The first group, referred to as Early Glass Mountain rhyolites, were erupted between about 2.1 Ma and 1.4 Ma and are characterized by a variable range of incompatible element concentrations, a range in ε_{Nd} values around –3, and high $^{87}Sr/^{86}Sr$ ratios (Fig. 6A; Bailey et al., 1989; Halliday et al., 1989). These chemical and isotopic characteristics indicate an upper crustal source for Early Glass Mountain rhyolite lavas (Halliday et al., 1989). Following an eruptive hiatus from 1.4 Ma to 1.2 Ma the second group of Glass Mountain rhyolites, termed the Late Glass Mountain rhyolites, were erupted from 1.2 Ma to 0.79 Ma (Bailey et al., 1989). In contrast to the Early lavas, Late Glass Mountain rhyolites show a much more uniform and less evolved composition. These lavas exhibit more homogeneous and depleted ε_{Nd} values of –1, with a tight spread of low $^{87}Sr/^{86}Sr$ compositions (Halliday et al., 1989). Such isotopic and geochemical characteristics have been interpreted to indicate a deep, primitive, and "mantle-like" source for the Late Glass Mountain Rhyolites (Halliday et al., 1989; Metz and Mahood, 1991).

Isochronous whole-rock Rb/Sr data are believed to yield ages corresponding to a time of isotopic homogenization with respect to $^{87}Sr/^{86}Sr$. On a Rb/Sr isochron, the slope of an isochron yields the age of isotopic homogenization, and the intercept with the y-axis gives the initial $^{87}Sr/^{86}Sr$ ratio. This initial $^{87}Sr/^{86}Sr$ ratio is representative of the isotopic composition of the system at the time of its homogenization. (Faure, 1986). A major differentiation or fractional crystallization event in a magma chamber is capable of homogenizing Rb/Sr isotopic systematics. Therefore isochronous whole-rock Rb/Sr data hold the potential to yield age information pertaining to such events (Halliday et al., 1989). In the case of Glass Mountain rhyolites, highly evolved lavas periodically tapped both the Early and Late magma systems. Collectively, these lavas define Rb/Sr isochrons whose ages are coeval with eruption ages of the oldest extrusives from each of the respective systems. This has been interpreted as strong evidence that Rb/Sr isochrons truly represent differentiation events in the magma chambers from which the lavas were erupted (Halliday et al., 1989; Christensen and Halliday, 1996).

Magma residence times in Long Valley Volcanic Field have been modeled as the difference between an Rb/Sr derived differentiation age on a suite of co-magmatic rocks and the youngest K/Ar (or $^{40}Ar/^{39}Ar$) determined eruption age from that suite (Metz and Mahood, 1985). For example, an Rb/Sr whole-rock isochron age of 1.90 ± 0.04 Ma was obtained on the Early Glass Mountain rhyolites (Fig. 6B; Halliday et al., 1989). The difference between this Rb/Sr isochron age and the age of the youngest erupted rhyolites that are chemically and isotopically identifiable with the Early Glass Mountain rhyolites (~1.4 Ma) yields ~500 m.y. of time. This span of time is interpreted to represent a residence time of the silicic magma body from which the Early Glass Mountain rhyolites erupted (Halliday et al., 1989). In the same way, an Rb/Sr whole-rock isochron of 1.14 ± 0.16 Ma is indicative of a ~300 k.y. residence time for 0.8 Ma Late Glass Mountain rhyolites (Fig. 6B; Halliday et al., 1989).

Halliday et al. (1989) offer a number of explanations for why their data are robust and truly representative of such differentiation ages. Among these are: 1) the Rb/Sr ages are different than a large body of internally consistent K/Ar eruption ages, indicating that Rb/Sr isotopic systematics must be dating a non-eruptive event; 2) the Sr and Nd isotopic compositions do not systematically vary with respect to each other, especially in the older lavas, ruling out the possibility of crustal contamination as an explanation for the observed $^{87}Sr/^{86}Sr$ ratios (Fig. 6). Furthermore, these $^{87}Sr/^{86}Sr$ ratios are strongly correlative with respect to Rb/Sr indicating the robust nature of the isochrons; and 3) the isochrons cannot represent simple partial melting of a host rock because it is impossible to generate the observed low Sr concentrations by this method alone. From these observations, Halliday et al. (1989) deduce that well defined Rb/Sr isochrons date the time at which a range of high Rb/Sr ratios were created as a result of a differentiation event in a magma chamber.

The Bishop Tuff has many chemical and isotopic affinities to Glass Mountain rhyolites (Halliday et al., 1989). Much of the chemically zoned Bishop Tuff shares whole-rock ε_{Nd} and $^{87}Sr/^{86}Sr$ values with those of the Late Glass Mountain rhyolites (Fig. 6A; Halliday et al., 1989; Davies and Halliday, 1998). Moreover, sanidine from the Bishop Tuff display Sr-Nd isotopic systematics that are identifiable with lavas erupted from both the Early and Late Glass Mountain rhyolites (Halliday et al., 1989; Davies and Halliday, 1998). These data suggest that significant portions of the Bishop Tuff magma chamber may have resided in the crust for more than 500 k.y. (Halliday et al., 1989).

Strontium isotopic systematics offer further support of a long magma residence time for the Bishop Tuff magma chamber. Christensen and DePaolo (1993) integrated Sr isotopic disequilibrium from glass and sanidine with thermodynamic parameters to calculate a 500 k.y. minimum on the time required to generate and subsequently chemically and isotopically zone the Bishop Tuff magma chamber. They support their conclusions by pointing out that if 7000 km^3/m.y. of basalt were added to the system, the

Bishop Tuff magma chamber could have resided in a molten state within the upper crust for more than 500 k.y. (Christensen and DePaolo, 1993).

2.2.2. *Implications of single-crystal $^{40}Ar/^{39}Ar$ and Rb/Sr studies for magma residence times*

Existing Rb/Sr isotopic data from the Long Valley Volcanic Field indicate that prior to the Bishop Tuff eruption, large volumes of silicic magma stagnated in the upper crust for protracted periods of time. However, it has long been known that whole-rock and bulk mineral Rb/Sr isotopic data can only provide information on the state of the magma upon eruption (Knesel et al., 1999 and references therein). Much of the existing Rb/Sr isotopic data is therefore a mixed record of the compositional and isotopic changes that occur during crystal growth. In an effort to address this problem, more recent isotopic studies have placed a greater emphasis on single crystal techniques.

In 1995, a $^{40}Ar/^{39}Ar$ single-crystal laser-fusion study on melt inclusion bearing quartz (MIBQ) phenocrysts from the Bishop Tuff seemingly provided an alternative method for determining magma residence times (van den Bogaard and Schirnick, 1995). This study yielded an $^{40}Ar/^{39}Ar$ isochron age of 1.93 ± 0.12 Ma on MIBQ from plinian tephra that has been used in support of a residence time (>1 Ma) for the Bishop Tuff magma chamber that is even longer than those indicated by previous Rb/Sr isotopic studies (van den Bogaard and Schirnick, 1995). The interpretations and conclusions drawn from this robust $^{40}Ar/^{39}Ar$ MIBQ dataset have been based on the assumption that phenocrysts of MIBQ are retentive of radiogenic argon at magmatic temperatures. MIBQ should therefore record closed system behavior of the K-Ar isotopic system from the time of MIBQ crystal growth. The 1.93 ± 0.12 Ma $^{40}Ar/^{39}Ar$ apparent age has been interpreted to represent a major crystallization and differentiation event in plinian parts of the Bishop Tuff magma chamber.

A subsequent detailed Rb/Sr study on single crystals of MIBQ yielded variable ages ranging from 1.420 ± 0.080 Ma to 2.500 ± 0.200 Ma (Christensen and Halliday, 1996). Analysis of bulk MIBQ from the same study yielded a Rb/Sr model age of 1.9 ± 0.3 Ma. These data are broadly consistent with the $^{40}Ar/^{39}Ar$ MIBQ data of van den Bogaard and Schirnick (1995). A 1998 study on strontium isotopic zoning in single crystals of sanidine from the Bishop Tuff offers even more evidence in favor of a >1 Ma residence time for the Bishop Tuff magma chamber (Davies and Halliday, 1998). Together, these two Rb/Sr studies lend significant credibility to the $^{40}Ar/^{39}Ar$ single-crystal laser-fusion data of van den Bogaard and Schirnick (1995).

Recently, studies of isotopic systematics pertaining to magma residence times tell a different story than studies published prior to 1998. Data from a study on Taylor Creek Rhyolite show that apparent isochrons can be constructed from whole-rock and mineral Rb/Sr isotopic data. These data are more consistent with mixing among multiple isotopic reservoirs via open-system processes (e.g., crustal contamination) than actual differentiation events (Knesel et al., 1999). This study casts doubt on the ability of bulk or even single-crystal Rb/Sr isotopic systematics to yield a time of isotopic homogenization and thus an age of differentiation. Complicating the story further, new U-Pb data from zircons of the Bishop Tuff provide evidence to suggest that the Bishop Tuff magma chamber did *not* reside in the crust for extended periods of time (Reid and Coath, 2000). Furthermore, Boyce et al. (2000), indicate that MIBQ are non-retentive of argon at magmatic temperatures. This paper presents new evidence that $^{40}Ar_E$ hosted in TMI and EMI of MIBQ yield spuriously old apparent ages from both single-crystal laser-fusion and laser step-heating $^{40}Ar/^{39}Ar$ analyses. Based on the data presented here, as well as those of Boyce et al. (2000), Reid and Coath, (2000), and Knesel et al. (1999), the notion of a long magma residence time for the Bishop Tuff Magma chamber can now be questioned on multiple grounds. Furthermore, if $^{40}Ar_E$ concentrations that are similar to those in MIBQ are hosted in sanidine trapped melt inclusions, effects on $^{40}Ar/^{39}Ar$ apparent age determinations of young sanidines would be expected and should be addressed.

CHAPTER 3. GEOCHEMICAL AND GEOCHRONOLOGICAL ANALYSES OF MELT INCLUSION BEARING QUARTZ AND SANIDINE FROM THE BISHOP AND BANDELIER TUFFS

3.1. Introduction

To better characterize $^{40}Ar/^{39}Ar$ compositions in MIBQ, quartz separates from plinian fall deposits of the Bishop and Bandelier Tuffs were laser step-heated. Prior to laser step-heating, MIBQ were treated with an air-abrasion mill grinder and hydrofluoric acid to progressively remove EMI and thereby isolate TMI. Both EMI and TMI are suspected of hosting $^{40}Ar_E$, and therefore the combined use of these sample treatments with the laser step-heating method affords a better characterization and a more precise assessment of the argon isotopic distributions in MIBQ than would be obtainable through single-crystal laser-fusion techniques. Any potentially distinct reservoirs of argon that might be contained within MIBQ are completely homogenized when heated by the single-crystal laser-fusion method, such as that used by van den Bogaard and Schirnick (1995). In contrast, age spectra results of laser step-heated MIBQ provide laser-power-controlled argon release information, capable of identifying the potential isotopic reservoirs otherwise disguised in traditional single-crystal laser-fusion $^{40}Ar/^{39}Ar$ analyses.

In addition to laser step-heating of MIBQ, single-crystal laser-fusion analyses allowed comparison with the results of van den Bogaard and Schirnick (1995). However, the laser step-heating results are a more informative and important contribution of this paper in that they strongly indicate the presence of distinct argon isotopic reservoirs in MIBQ and furthermore implicate melt-inclusion-hosted $^{40}Ar_E$ as the culprit in producing old apparent ages from MIBQ. Sanidine phenocrysts of the Bishop and Bandelier Tuffs that grew and erupted simultaneously with MIBQ in plinian deposits contain compositionally identical trapped melt inclusions that are suspected of hosting similar concentrations of $^{40}Ar_E$. Based on measured $^{40}Ar_E$ concentrations in MIBQ, $^{40}Ar_E$ can potentially to add from ~4 k.y. to ~40 k.y. to individual $^{40}Ar/^{39}Ar$ single-crystal laser-fusion sanidine analyses of the Bishop and Bandelier Tuffs. Moreover, depending on the siting of this $^{40}Ar_E$ in sanidines, it may not be detectable by the isochron method of analyzing a population of $^{40}Ar/^{39}Ar$ data for excess argon. As a function of variable $^{40}Ar_E$ concentrations in trapped melt inclusions and their respective abundances in sanidines, $^{40}Ar_E$ can add uncertainty to a $^{40}Ar/^{39}Ar$ weighted-mean apparent age in ways such that predicted ~4 k.y. to ~40 k.y. age increases may or may not be resolvable within the analytically achievable weighted-mean age uncertainty on a population of $^{40}Ar_E$-free sanidines. If unaccounted for, this $^{40}Ar_E$-induced uncertainty can comprise a large percentage of the weighted-mean apparent age on a population of young sanidines from plinian fall deposits.

3.2. *Methods*

3.2.1. *Samples and sample preparation*

With one exception, all samples were collected from localities of the Bishop and Bandelier plinian pumice deposits (Table 1; Figs. 2 and 3). Sample BT-1 (Fig. 3) was collected from a 110 cm thick plinian pumice fall deposit of the Bishop Tuff (unit F7, location 94; Wilson and Hildreth, 1997). Sample BT-2 (Fig. 3) was collected from a 20 cm thick plinian deposit of the Bishop Tuff (unit F2, location 94; Wilson and Hildreth, 1997) that is earlier in the eruptive sequence than sample BT-1. Sample UBT-1 (Fig. 2) was collected from a 90 cm thick plinian pumice deposit of the Upper Bandelier Tuff (Section 6-12; Stix et al., 1988). Another sample of the Upper Bandelier Tuff plinian deposit (Fig. 2; UBT-2) was collected from the 70 cm thick unit B of Self et al. (1996). A sample of the Lower Bandelier Tuff (Fig. 2; LBT-1) was collected from a 460 cm thick plinian pumice deposit (Unit A; Self et al., 1996, and references therein). In addition to samples collected from plinian fall deposits, pumice clasts from a conglomerate (sample LBT-2) were collected in the southern Espanola basin of the Rio Grande Rift and is chemically correlated to the Lower Bandelier Tuff (P. Bauer, 1999, pers. comm.; N. Dunbar, 2000, pers. comm.).

Table 1. Summary of sample locations and stratigraphic nomenclature.

Sample	Material	Unit	Stratigraphic Name	Location/Reference
Bishop Tuff				
BT-1	MIBQ	Bishop Tuff Plinian Pumice	Bishop Tuff Pumice	unit F7, location 94; Wilson and Hildreth (1997)
BT-2	Sanidine	Bishop Tuff Plinian Pumice	Bishop Tuff Pumice	unit F2, location 94; Wilson and Hildreth (1997)
Upper Bandelier Tuff				
UBT-1	MIBQ	Upper Bandelier Tuff Plinian Pumice	Tsankawi Pumice	section 6, Stix et al. (1989)
UBT-2	Sanidine	Upper Bandelier Tuff Plinian Pumice	Tsankawi Pumice	unit B, Smith et al. (1979); Stop 1 Self et al. (1996)
Lower Bandelier Tuff				
LBT-1	MIBQ	Lower Bandelier Tuff Plinian Pumice	Guaje Pumice	unit A, Smith et al. (1979); Stop 1 Self et al. (1996)
LBT-2	Sanidine	un-named	Correlates by age and chemistry to Guaje Pumice	Intersection of I-25 and Richards Ave., Seton Village Quadrangle, Espanola Basin, P. Bauer (Pers. Com.)

Sample preparation was performed at the New Mexico Geochronology Research Laboratory (NMGRL). MIBQ separates were obtained from samples BT-1, UBT-1, and LBT-1, while sanidine was separated from samples BT-2, UBT-2, and LBT-2. Both sanidine and MIBQ were separated from crushed pumice and ultrasonically cleaned of their adhering pumiceous glass in 15% hydrofluoric acid for 10 minutes. Sanidine separates were irradiated for seven hours in the D-3 position of the Nuclear Science Center reactor, College Station, TX. Separates of MIBQ were irradiated for one hour in the L-67 position of the University of Michigan Ford reactor facility, and subsequently, sample splits were treated to progressively remove EMI. Three splits of each MIBQ sample were prepared for $^{40}Ar/^{39}Ar$ analysis: "MT" (minimally treated) splits were left with the original 10 minute HF treatment that all samples received; "MG" (millground) splits were milled in an air-abrasion mill (Goldich and Fischer, 1986) for one hour; and "HF" (hydrofluoric acid leached) splits were ultrasonically treated in 15% hydrofluoric acid for one hour. MIBQ of each split were imaged using the electron microprobe prior to $^{40}Ar/^{39}Ar$ analysis.

3.2.2. Electron microprobe methods

Quantitative major-element electron microprobe analyses were performed on EMI, TMI, and matrix quartz from minimally treated MIBQ. All microprobe analyses were performed using a CAMECA SX-100 operating with a beam current of 20 nA and an acceleration voltage of 15 kV. Beam size ranged from 10 to 25 μm to minimize Na volatilization. Counts of 20 sec. on peak were used for all elements with the exception of Na (40 sec.), F (100 sec.), and Cl (40 sec.). The following elements were analyzed with their associated precisions based on 12 replicate analyses of Smithsonian standard reference material VG-568: P_2O_5 ± 0.01 wt%, SiO_2 ± 0.60 wt%, SO_2 ± 0.02 wt%, TiO_2 ± 0.03 wt%, Al_2O_3 ± 0.09 wt%, MgO ± 0.03 wt%, CaO ± 0.01 wt%, MnO ± 0.02 wt%, FeO ± 0.06 wt%, Na_2O ± 0.59 wt%, K_2O ± 0.07 wt%, F ± 0.08 wt%, and Cl ± 0.01 wt%. For comparison of analyzed and certified values of VG-568, see Appendix A. A number of standard reference materials, including selected amphiboles, feldspars, and natural and synthetic glasses were run as part of every analytical session to monitor accuracy of probe calibration.

3.2.3. $^{40}Ar/^{39}Ar$ methods

All samples were analyzed for $^{40}Ar/^{39}Ar$ isotopic compositions using the NMGRL fully-automated argon extraction system. Bulk MIBQ were step-heated with a 50 W CO_2 laser equipped with a beam integrator to facilitate homogeneous step-heating. Individual phenocrysts of sanidine and MIBQ were fused with a focused 10 W CO_2 laser. Reactive gasses were removed by a one minute reaction with two SAES GP-50 getters. Gas was also exposed to a W filament operated at ~2000°C and a cold finger operated at –140°C. Subsequent to gettering, the gas was expanded into a MAP 215-50 mass spectrometer. Argon isotopes were measured in electron multiplier mode operating at a net sensitivity ranging from 1×10^{-16} to 8.6×10^{-17} mol/pA. Analytical results and age selection criteria are compiled in Appendices B, C, and D. Detailed analytical methods and summaries of the analytical results are provided in Tables 2, 3, and 4. Unless otherwise stated, all errors are reported at the 2σ confidence level.

Table 2. Summary results of MIBQ electron microprobe analyses.

Sample	n	SiO_2	TiO_2	Al_2O_3	MgO	CaO	MnO
Bishop Tuff							
BT-1 MIBQ Qtz Matrix avg	20	99.86 (0.38)	0.02 (0.02)	0.01 (0.01)	0.01 (0.02)	0.01 (0.01)	0.02 (0.02)
BT-1 MIBQ TMI avg	8	77.54 (0.47)	0.05 (0.02)	12.92 (0.09)	0.03 (0.02)	0.43 (0.03)	0.02 (0.02)
BT-1 MIBQ EMI avg	18	77.69 (1.20)	0.06 (0.03)	12.79 (0.26)	0.02 (0.02)	0.42 (0.03)	0.01 (0.02)
Avg MIBQ Melt Inclusion*	48	77.40		12.80	0.02	0.40	
Avg Matrix Pumice†	8	77.10		13.00	0.03	0.40	
Upper Bandelier Tuff							
UBT-1 MIBQ Qtz avg	8	99.90 (0.46)	0.01 (0.02)	0.01 (0.01)	0.02 (0.02)	0.01 (0.01)	0.01 (0.02)
UBT-1 MIBQ TMI avg	12	76.60 (0.63)	0.05 (0.03)	12.37 (0.17)	0.00 (0.00)	0.25 (0.02)	0.06 (0.04)
UBT-1 MIBQ EMI avg	12	76.42 (0.61)	0.05 (0.02)	12.36 (0.07)	0.01 (0.01)	0.27 (0.02)	0.05 (0.05)
Avg MIBQ Melt Inclusion§	21	76.10		12.60		0.30	0.10
Avg Pumice Composition#		76.20		12.30		1.30	0.10
Lower Bandelier Tuff							
LBT-1 MIBQ Qtz avg	11	99.84 (0.31)	0.01 (0.01)	0.01 (0.01)	0.02 (0.03)	0.01 (0.01)	0.01 (0.01)
LBT-1 MIBQ TMI avg	15	77.08 (0.56)	0.05 (0.03)	12.49 (0.09)	0.01 (0.03)	0.24 (0.02)	0.05 (0.04)
LBT-1 MIBQ EMI avg	14	76.90 (0.53)	0.04 (0.03)	12.38 (0.15)	0.00 (0.00)	0.24 (0.02)	0.06 (0.04)
Avg MIBQ Melt Inclusion§	41	77.50		12.10		0.30	0.10
Avg Pumice Composition**		77.10		12.20		0.30	0.10

Sample	n	FeO	Na_2O	K_2O	F	Cl	Total
Bishop Tuff							
BT-1 MIBQ Qtz Matrix avg	20	0.01 (0.02)	0.01 (0.01)	0.01 (0.01)	0.02 (0.04)	0.01 (0.01)	100.00
BT-1 MIBQ TMI avg	8	0.64 (0.04)	3.61 (0.08)	4.57 (0.03)	0.08 (0.04)	0.08 (0.01)	100.00
BT-1 MIBQ EMI avg	18	0.63 (0.04)	3.24 (0.31)	4.92 (0.44)	0.09 (0.07)	0.08 (0.01)	100.00
Avg MIBQ Melt Inclusion*	48	0.60	3.70	4.90			
Avg Matrix Pumice†	8	0.50	3.90	4.90			
Upper Bandelier Tuff							
UBT-1 MIBQ Qtz avg	8	0.00 (0.01)	0.01 (0.01)	0.01 (0.01)	0.01 (0.02)	0.00 (0.00)	100.00
UBT-1 MIBQ TMI avg	12	1.38 (0.07)	4.22 (0.13)	4.44 (0.08)	0.32 (0.08)	0.29 (0.02)	100.00
UBT-1 MIBQ EMI avg	12	1.38 (0.06)	4.43 (0.16)	4.45 (0.16)	0.29 (0.07)	0.28 (0.02)	100.00
Avg MIBQ Melt Inclusion§	21	1.10	3.80	5.60			
Avg Pumice Composition#		1.30	3.40	5.40			
Lower Bandelier Tuff							
LBT-1 MIBQ Qtz avg	11	0.01 (0.01)	0.00 (0.01)	0.01 (0.01)	0.05 (0.07)	0.01 (0.01)	100.00
LBT-1 MIBQ TMI avg	15	1.25 (0.05)	4.03 (0.32)	4.29 (0.09)	0.26 (0.09)	0.22 (0.02)	100.00
LBT-1 MIBQ EMI avg	14	1.27 (0.04)	4.51 (0.31)	4.07 (0.17)	0.27 (0.12)	0.22 (0.02)	100.00
Avg MIBQ Melt Inclusion§	41	1.30	4.20	4.40			
Avg Pumice Composition**		1.20	4.30	4.40			

Notes:
Analyses made by electron microprobe and are reported as water-free for data comparison purposes.
Numbers in parentheses represent the standard deviation of the mean.
Analytical uncertainty, based on 12 replicate analyses of standard reference material VG-568, are as follows: SiO_2 ± 0.60 wt%, TiO2 ± 0.03 wt%, Al2O3 ± 0.09 wt%, MgO ± 0.03 wt%, CaO ± 0.01 wt%, MnO ± 0.02 wt%, FeO ± 0.06 wt%, Na_2O ± 0.59 wt%, K2O ± 0.07 wt%, F ± 0.08 wt%, and Cl ± 0.01 wt%.
*From Dunbar and Hervig (1992a).
†From Hildreth (1981).
§From Dunbar and Hervig (1992b).
#From Balsley (1988).
**From Kuentz (1986).

Table 3. Summary results of $^{40}Ar/^{39}Ar$ MIBQ analyses.

Sample	Sample Treat-ment †	Argon Extraction Method §	Unit **	L#	Plateau Steps	Plateau Age (Ma)	±2σ	Total Gas Age (Ma)	±2σ	Weighted Mean Age (Ma)	±2σ
Bishop Tuff											
5810, 8411*	UD	SCLF	BTP							1.89	0.06
BT-1-MT	MT	SCLF	BTP	50588						2.52	0.27
BT-1-MT	MT	LSH	BTP	50401-04	A-J	1.85	0.06	1.90	1.01		
BT-1-MG	MG	LSH	BTP	50584-01	A-G	2.43	0.05	2.58	0.43		
BT-1-HF	HF	LSH	BTP	50582-01	A-J	3.70	0.16	3.70	1.00		
Upper Bandelier Tuff											
UBT-1-MT	MT	SCLF	UBTP	50606						5.20	0.64
UBT-1-MT	MT	LSH	UBTP	50402-01	A-C	4.09	0.07	4.54	0.48		
UBT-1-MG	MG	LSH	UBTP	50601-01	A-E	8.66	0.14	8.70	1.20		
UBT-1-HF	HF	LSH	UBTP	50600-01	E-H	11.41	0.16	11.54	0.87		
Lower Bandelier Tuff											
LBT-1-MT	MT	SCLF	LBTP	50597						6.59	1.59
LBT-1-MT	MT	LSH	LBTP	50400-01	No Plateau			6.02	0.86		
LBT-1-MG	MG	LSH	LBTP	50593-01	A-F	11.69	0.16	11.90	1.20		
LBT-1-HF	HF	LSH	LBTP	50591-01	E-J	15.92	0.87	14.60	1.50		

Sample	Sample Treat-ment †	Argon Extraction Method §	Unit **	L#	Isochron Age (Ma)	±2σ	$(^{40}Ar/^{36}Ar)t$	±2σ	MSWD
Bishop Tuff									
5810, 8411*	UD	SCLF	BTP		1.93	0.12	290.0	7.0	2.2
BT-1-MT	MT	SCLF	BTP	50588	1.73	0.18	312.1	8.0	6.7
BT-1-MT	MT	LSH	BTP	50401-04	1.89	0.07	291.3	4.0	2.4
BT-1-MG	MG	LSH	BTP	50584-01	2.46	0.06	297.1	4.4	7.2
BT-1-HF	HF	LSH	BTP	50582-01	3.66	0.09	306.0	25.2	1.3
Upper Bandelier Tuff									
UBT-1-MT	MT	SCLF	UBTP	50606	7.45	0.28	917.0	106.0	13.3
UBT-1-MT	MT	LSH	UBTP	50402-01	4.83	0.05	284.2	2.8	62.2
UBT-1-MG	MG	LSH	UBTP	50601-01	7.56	0.11	318.8	8.6	12.1
UBT-1-HF	HF	LSH	UBTP	50600-01	11.05	0.32	632.8	137.8	2.6
Lower Bandelier Tuff									
LBT-1-MT	MT	SCLF	LBTP	50597	2.18	0.14	283.6	7.6	81.8
LBT-1-MT	MT	LSH	LBTP	50400-01	6.98	0.05	254.0	3.8	151.6
LBT-1-MG	MG	LSH	LBTP	50593-01	11.72	0.26	300.6	8.4	8.9
LBT-1-HF	HF	LSH	LBTP	50591-01	16.15	0.22	164.2	20.4	8.6

Table 3 continued.

Notes:

Irradiation Procedures: Samples and flux monitors of Fish Canyon Tuff sanidine (27.84 Ma; Deino and Potts, 1990) were interspersed evenly at 1 cm intervals and stacked vertically in evacuated 3/4 inch quartz tubes. Tubes were irradiated for 1 hour at the University of Michigan in the L-67 position of the Ford Reactor facility. J-factors were determined to ± 0.10% by analyzing four crystals from each flux monitor position. Correction factors determined from long term monitoring of the reactor facility, and values used are given in Appendecies B and C.

NMGRL Analytical Procedures and Specifications: A 50 W CO_2 laser was used to step-heat MIBQ. Affixed to the laser was a beam integrator to achieve a flat 6 mm^2 power distribution across grains and facilitate even step-heating. Gas was cleaned with a SAES GP-50 getter and expanded into a MAP-215-50 mass spectrometer. For single-crystal laser-fusion analyses, a 10 W focused CO2 laser was used. Argon isotopes were measured in electron multiplier mode at a net sensitivity ranging from 1×10^{-16} to 8.6×10^{-17} mol/pA. Total system blank values were: 2.9×10^{-16}, 4.8×10^{-18}, 7.0×10^{-19}, 2.1×10^{-18}, 2.7×10^{-18} at masses 40, 39, 38, 37, and 36 respectively.

Plateau age selection criteria: Plateaus are selected as the flattest portion of the age spectra that meet or approach the MSWD (mean standard weighted deviates) criteria of Mahon (1996). Plateau and weighted mean ages are calculated by weighting each analysis by the inverse of its variance. Errors are assigned to ages using the calculations of Taylor (1982). Where MSWD values lie outside the 95% confidence limits for n-1 degrees of freedom, the error is multiplied by the square root of the MSWD (Mahon, 1996).

*From van den Bogaard and Schirnick (1995).

†Three sample treatments applied to all MIBQ in this study as well as the ultrasonic disintegration treatment reported by van den Bogaard and Schirnick (1995). Treatments are as follows: UD, ultrasonic disintegration (van den Bogaard and Schirnick, 1995); MT, minimally treated; MG, millground in an air abrasion mill for 1 hour; and HF, treated in hydrofluoric acid for 1 hour. The UD of van den Bogaard and Schirnick (1995) and the MT reported in this study are nearly identical and are therefore directly comparable.

§Methods of heating sample are as follows: SCLF, single-crystal laser-fusion; and LSH, laser step-heating.

**Units sampled are as follows: BTP, Bishop Tuff pumice; UBTP, Upper Bandelier pumice; and LBTP, Lower Bandelier pumice.

Table 4. Summary results of $^{40}Ar/^{39}Ar$ single-crystal laser-fusion sanidine analyses.

Sample	Unit	L#	n	Weighted Mean Age (Ma)	±2σ	Isochron Age (Ma)	±2σ	$(^{40}Ar/^{36}Ar)t$	±2σ	MSWD
Bishop Tuff										
BT-2	Bishop Tuff Plinian	9487	11	0.768	0.004	0.762	0.020	302.7	21.5	3.1
79G14, 85G50a*	Bishop Tuff Plinian		11	0.772	0.010					
79G94*	Bishop Tuff Ignimbrite		12	0.764	0.018					
Upper Bandelier Tuff										
UBT-2	Upper Bandelier Tuff Plinian	9775, 9776	19	1.294	0.010	1.289	0.028	293.6	41.7	4.7
8/27†	Upper Bandelier Tuff Plinian		8	1.209	0.006	1.225	0.008	288.0	14.0	0.2
91G36*	Upper Bandelier Tuff Plinian		4	1.235	0.032					
20-55, 22-50§	Upper Bandelier Tuff Ignimbrite		16	1.171	0.008					
Lower Bandelier Tuff										
LBT-2	Lower Bandelier Tuff Plinian	9778, 9779, 9780	35	1.607	0.011	1.606	0.022	299.3	16.6	3.0
17-31†	Lower Bandelier Tuff Plinian		8	1.605	0.008	1.608	0.010	297.0	2.0	1.6
91G35*	Lower Bandelier Tuff Plinian		4	1.629	0.022					
18-42, 17-31§	Lower Bandelier Tuff Ignimbrite		19	1.564	0.010					

Notes:

Irradiation Procedures: Samples and flux monitors of Fish Canyon Tuff sanidine (27.84 Ma; Deino and Potts, 1990) were interspersed evenly at 1 cm intervals and stacked vertically in evacuated quartz tubes. Tubes were irradiated for 1 hour at the University of Texas, Austin in the D-3 position of the Nuclear Science Center Reactor. J-factors were determined to ± 0.10% by analyzing four crystals from each flux monitor position. Correction factors determined from long term monitoring of the reactor facility, and values used are given in Appendix D.

NMGRL Analytical Procedures and Specifications: A 10 W focused CO_2 laser was used. Gas was cleaned with a SAES GP-50 getter and expanded into a MAP-215-50 mass spectrometer. Argon isotopes were measured in electron multiplier mode at a net sensitivity ranging from 1×10^{-16} to 8.6×10^{-17} mol/pA. Total system blank values were: 2.9×10^{-16}, 4.8×10^{-18}, 7.0×10^{-19}, 2.1×10^{-18}, 2.7×10^{-18} at masses 40, 39, 38, 37, and 36 respectively.

Weighted mean ages are calculated by weighting each analysis by the inverse of its variance. Errors are assigned to ages using the calculations of Taylor (1982). Where MSWD values lie outside the 95% confidence limits for n-1 degrees of freedom, the error is multiplied by the square root of the MSWD (Mahon, 1996).

*From Izett and Obradovich (1994), adjusted to Fish Canyon Tuff sanidine (27.84 Ma; Deino and Potts, 1990)

†From Spell et al. (1996), adjusted to Fish Canyon Tuff sanidine (27.84 Ma; Deino and Potts, 1990)

§From Spell et al. (1990), adjusted to Fish Canyon Tuff sanidine (27.84 Ma; Deino and Potts, 1990)

3.3. Results

3.3.1. Electron microprobe analyses of MIBQ

Electron microprobe major element analyses are summarized in Table 2 and compiled in Appendix A. Quantitative analyses of EMI and TMI in split MT are homogeneous in major element composition with respect to each other and the MIBQ host matrix pumice (Table 2). These results concur with measurements made by Dunbar and Hervig (1992a,b). No systematic variation in major element chemistry was observed as a function of melt inclusion size. Lastly, analyses of the quartz indicates that it is devoid of any measurable concentrations of potassium, such as might be expected from quartz of rhyolitic magmatic systems.

Backscattered electron images illustrate the progressive removal of EMI from MIBQ with sample treatment (Fig. 7). Crystals in split MT contain both EMI and TMI, as well as ~80 μm thick coatings of non-vesicular glass surrounding the crystal (Fig. 7A). These quartz crystals are directly comparable with those of van den Bogaard and Schirnick (1995). Outer margins of EMI were removed from the MIBQ of split MG; trapped inclusions remained unaffected (Fig. 7B). EMI were completely removed from split HF, leaving only TMI (Fig. 7C).

3.3.2. $^{40}Ar/^{39}Ar$ laser step-heating analyses of MIBQ

For all samples, laser step-heating apparent ages (Table 3; Appendix B) vary with the progressive removal of EMI. K/Qtz ratios were calculated using the $^{40}Ar/^{39}Ar$ data and sample weights to give the fraction of rhyolite glass present in MIBQ. As expected, these ratios decrease with progressive EMI removal. This trend is consistent with electron microprobe observations that sample treatment removes EMI, thereby isolating TMI (Fig. 7). The age spectra of HF and MG splits of BT-1 are relatively flat, whereas those of samples UBT-1 and LBT-1 display significantly more structure (Fig. 8). MT splits of all samples display climbing age spectra similar to that noted by Boyce et al. (2000). For all three samples, apparent ages increase with removal of EMI as shown in the age spectra of Figure 8 and in a plot of K/Qtz against total gas age (Fig. 9). Hydrofluoric-acid-treated splits of BT-1, UBT-1, and LBT-1 contain only TMI and yield total gas ages of 3.70 ± 1.00, 11.54 ± 0.87, and 14.60 ± 1.50 Ma, respectively (Table 3).

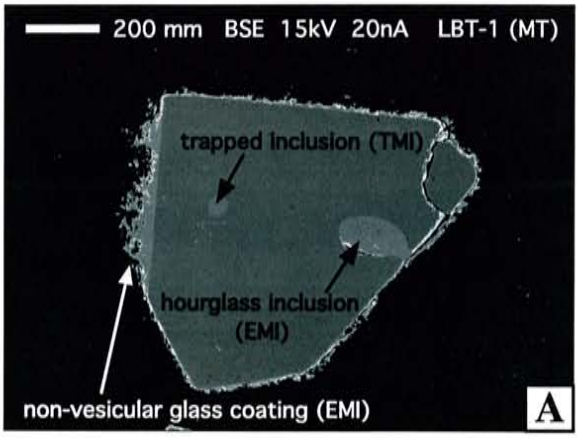

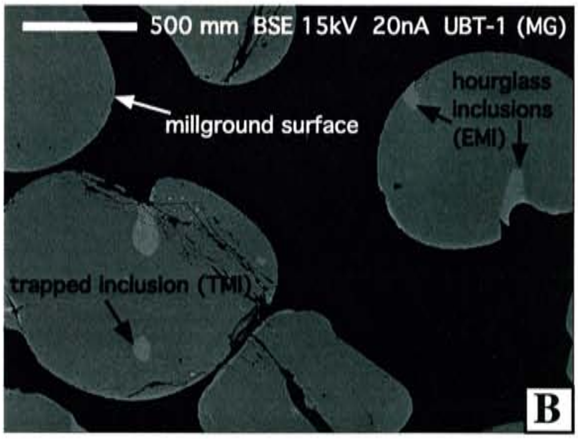

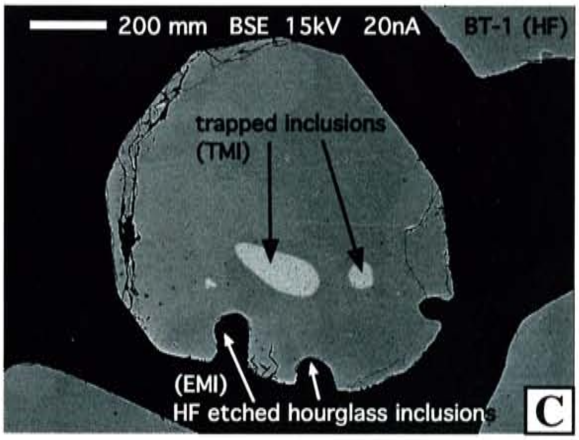

Figure 7. Backscattered electron images of quartz crystals subjected to three sample treatments. A) MT-minimally treated MIBQ received the same treatment of 15% hydrofluoric acid for 10 minutes that all samples received. B) MG-milled for one hour with an air-abrasion mill grinder (Goldich and Fischer, 1986). C) HF-treated with 15% hyrofluoric acid for one hour. See text for detailed discussion of treatment effects.

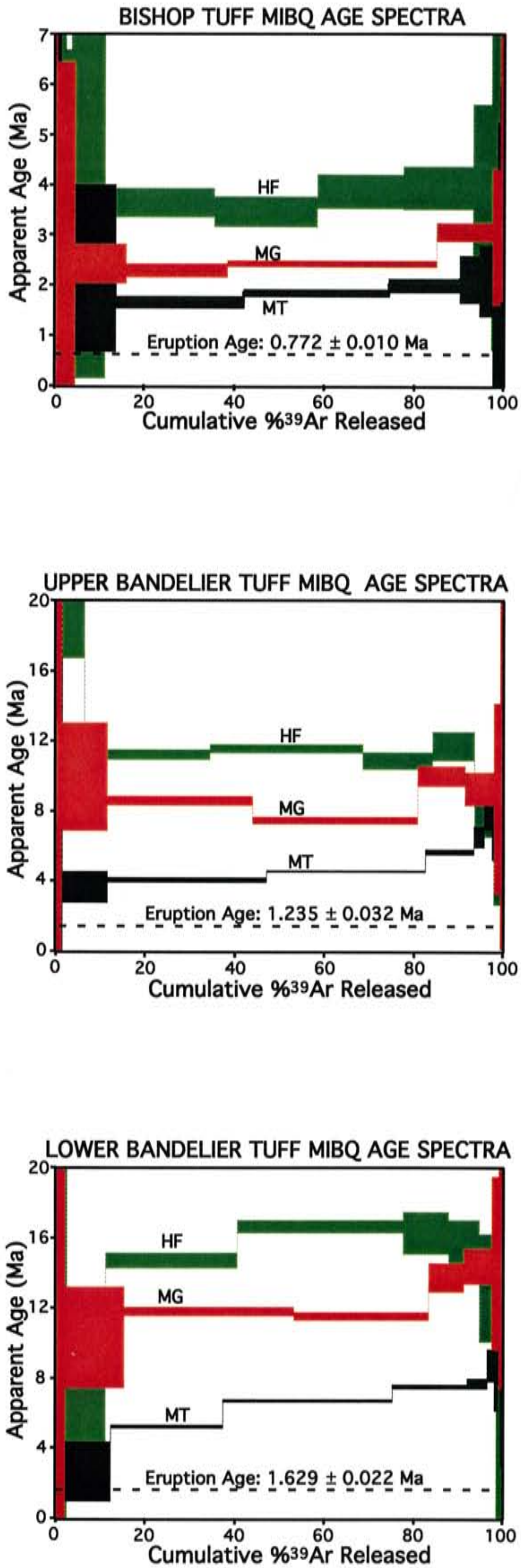

Figure 8. Bishop and Bandelier MIBQ laser step-heating age spectra. Treatment splits MT, MG, and HF are represented by black, gray and hatched patterns respectively. Eruption ages shown as dashed reference line (Izett and Obradovich, 1994).

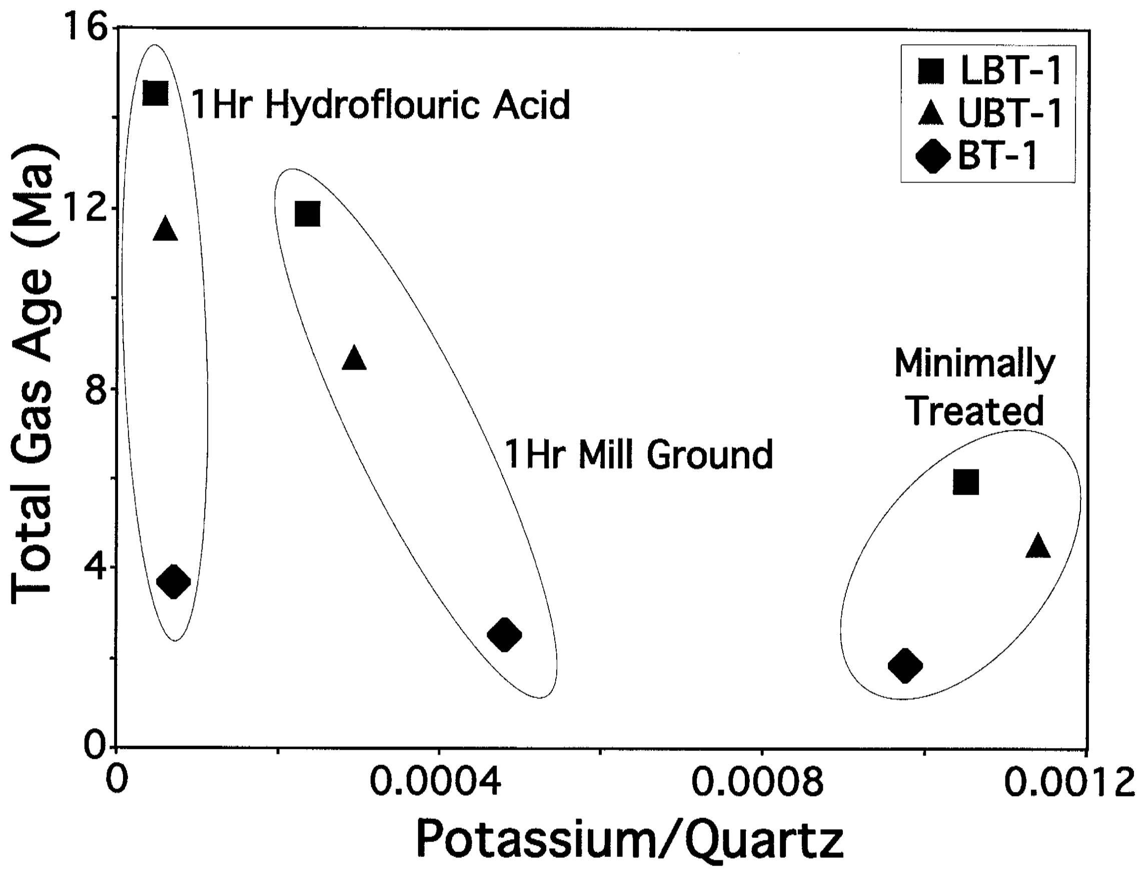

Figure 9. Variation of MIBQ total gas age as a function of the K/Qtz weight ratio. K/Qtz is used as a proxy for the amount of rhyolite glass present relative to quartz.

With the exception of low-precision steps, the apparent ages of all samples are significantly older than their respective eruption ages (Fig. 8; Appendix B).

All isochron ages agree with the respective plateau and total gas ages. Isochrons tend to be well defined for BT-1 splits and poorly defined for UBT-1 and LBT-1 splits (Fig. 10; see MSWD value, Table 3). BT-1 splits display $^{40}Ar/^{36}Ar$ intercepts consistently within error of atmospheric argon composition (Table 3). In contrast, $^{40}Ar/^{36}Ar$ intercepts of UBT-1 and LBT-1 samples are highly variable with values ranging from as low as 164 ± 20 for LBT-1(HF), to as high as 633 ± 138 for UBT-1(HF) (Table 3).

3.3.3. $^{40}Ar/^{39}Ar$ single-crystal laser-fusion analyses of MIBQ

Single-crystal laser-fusion analyses of MIBQ were performed on MT splits of each sample. The analytical results are summarized in Table 3 and compiled in Appendix C. Minimally treated MIBQ phenocrysts containing both TMI and EMI are similar to the quartz analyzed by van den Bogaard and Schirnick (1995), enabling direct comparisons to be made between the data presented here. Glass abundances in MIBQ were calculated from $^{39}Ar_K$ concentrations determined during single-crystal laser-fusion analysis and from the melt inclusion K contents which were determined by electron microprobe analysis. Minimally treated splits of LBT-1 and UBT-1 both exhibit narrow spreads in glass contents, ranging from ~0.007 to ~0.034 mg of rhyolite glass per mg crystal. Minimally treated MIBQ of BT-1 indicate a larger range of glass contents (~0.006 to ~0.063 mg of glass per mg of crystal), reflecting the more abundant EMI (hourglass inclusions in particular) in BT-1 MIBQ which have also been observed by

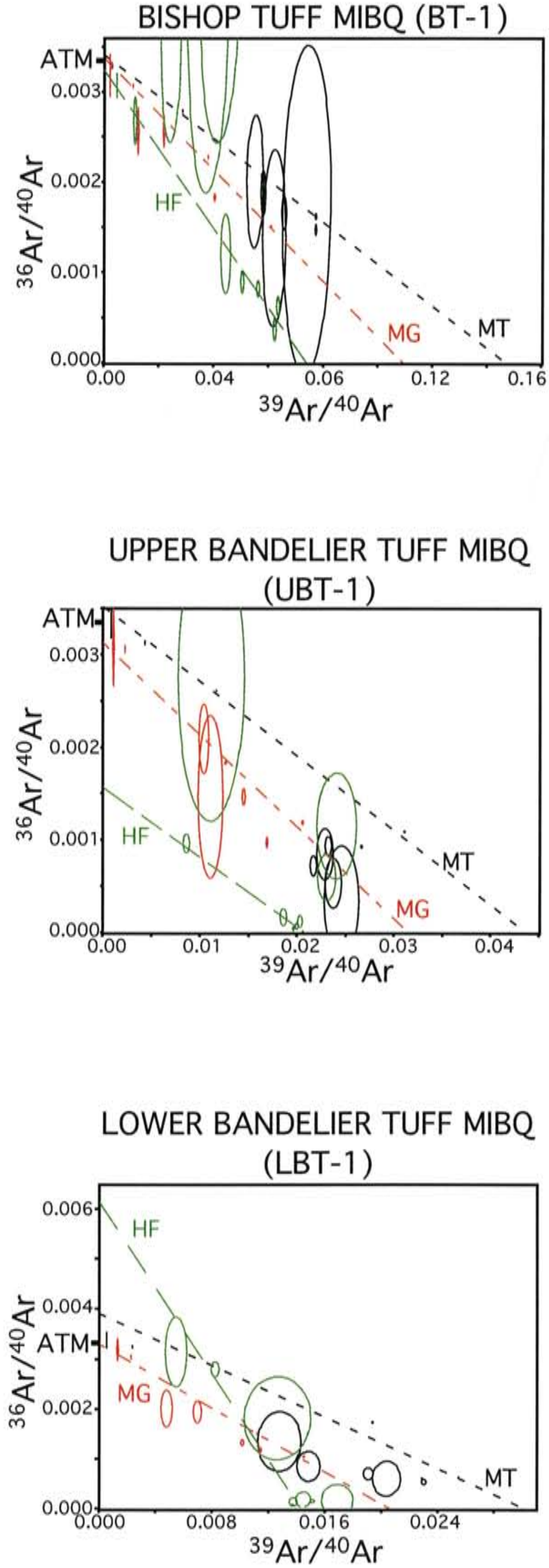

Figure 10. Isotope correlation diagrams for laser step-heated Bishop and Bandelier MIBQ. Isochron lines of treatment splits MT, MG, and HF are represented by black, red, and green respectively as as well as by different dash patterns. Error ellipses corresponding to MT, MG, and HF share the same color scheme as isochron lines. Ellipses are displayed at the 1σ confidence limits. Isochrons are fairly well defined for Bishop samples and poorly defined for Bandelier samples. Isochron ages increase with EMI removal, mimicking the behavior of corresponding age spectra in Figure 8.

point counting. These glass contents are consistent with those determined previously on Bishop Tuff plinian MIBQ (van den Bogaard and Schirnick, 1995).

The single-crystal laser-fusion $^{40}Ar/^{39}Ar$ apparent ages of all MIBQ samples are significantly older than their respective eruption ages (determined by $^{40}Ar/^{39}Ar$ analyses of sanidine from both Bishop and Bandelier plinian deposits; Izett and Obradovich, 1994). Minimally treated BT-1 MIBQ yield a poorly defined isochron with an age of 1.73 ± 0.18 Ma and an MSWD of 6.7 (Fig. 11; Table 3). Both isochron and weighted-mean ages of BT-1 are broadly consistent with the MIBQ ages reported by van den Bogaard and Schirnick (1995). Samples LBT-1 and UBT-1 also display poorly defined isochrons with high MSWD values of 81.8 and 13.3 respectively (Table 3). UBT-1 exhibits an isochron age of 7.45 ± 0.28 Ma with a trapped $^{40}Ar/^{36}Ar$ composition of 917.0 ± 106.0, while LBT-1 yields an isochron age of 2.18 ± 0.14 Ma with a trapped $^{40}Ar/^{36}Ar$ composition of 283.6 ± 7.6 (Fig. 11; Table 3).

3.3.4. $^{40}Ar/^{39}Ar$ single-crystal laser-fusion analyses of sanidine

Single-crystal laser-fusion age determinations of sanidine are summarized in Table 4 and Appendix D. Eleven sanidine crystals of BT-2 give highly variable ^{40}Ar radiogenic yields ranging from 63.5% to 82.9%. K/Ca values range from 39.9 to 77.6. A weighted-mean age of 0.768 ± 0.004 Ma is obtained for the 11 analyses (Fig. 12A; Table 4). An isochron yields an age of 0.762 ± 0.020 Ma, with a $^{40}Ar/^{36}Ar$ intercept of 302.7 ± 21.5 and an MSWD of 3.11 (Fig. 12B; Table 4). Both weighted-mean and isochron ages are consistent with a previously reported $^{40}Ar/^{39}Ar$ sanidine age of 0.772 ± 0.010 Ma (Table 4) from the Bishop Tuff plinian deposit (Izett and Obradovich, 1994).

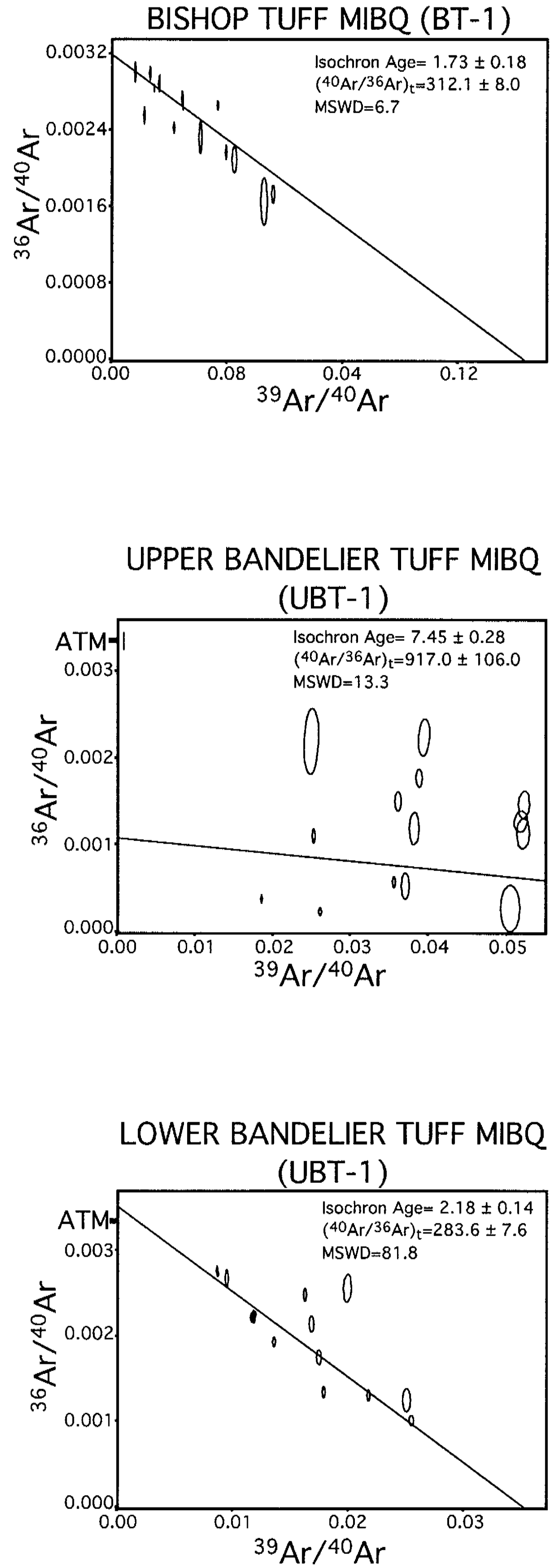

Figure 11. Isotope correlation diagrams for single-crystal laser-fusion Bishop and Bandelier MIBQ. Analyses performed on minimally treated MIBQ that are nearly identical to those of van den Bogaard and Schirnick (1995). Isochron ages, $(^{40}Ar/^{36}Ar)_t$ compositions, and MSWDs are indicated in upper right of diagrams. Error ellipses are displayed at the 1σ confidence limits. Bishop MIBQ displays a statistically well defined isochron relative to those of the Bandelier Tuffs. The isochron of BT-1 is broadly consistent with that formed by MIBQ single-crystal laser-fusion analyses of van den Bogaard and Schirnick (1995).

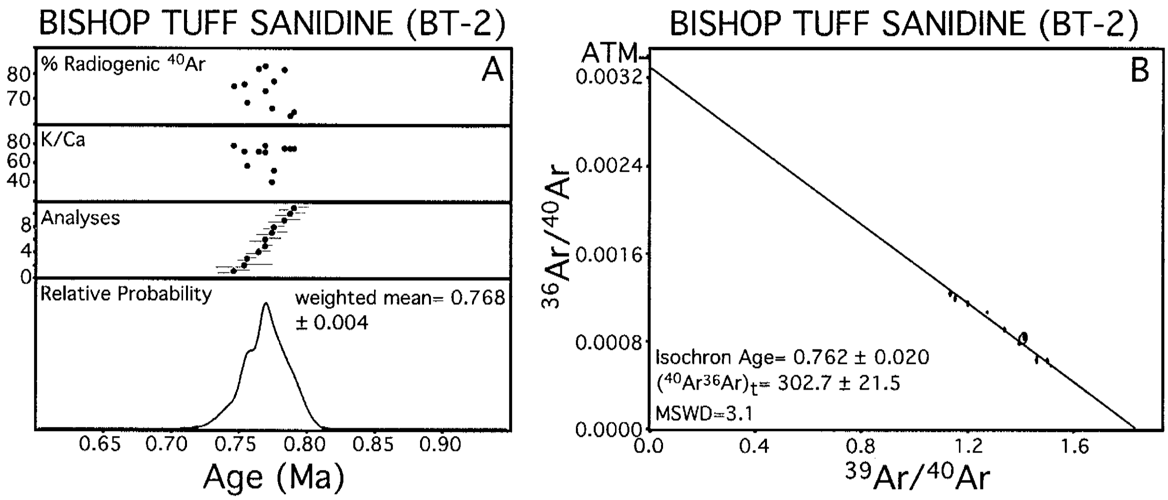

Figure 12. A) Ideogram of single-crystal laser-fusion sanidine results for BT-2. Values plotted against age include % Radiogenic ^{40}Ar, K/Ca, and ideogram curve. Ideogram curve represents the sum of the gaussian probability distributions for individual analyses (Deino and Potts, 1992). B) Isotope correlation diagram of BT-2 single-crystal laser-fusion analyses. Isochron age, $(^{40}Ar/^{36}Ar)_t$ composition, and MSWD are shown in bottom left corner of diagram. Error ellipses are displayed at the 1σ confidence limits.

Single-crystal laser-fusion analyses were performed on 19 sanidine crystals of UBT-2. Percent yield of radiogenic ^{40}Ar is scattered, ranging from 68.7% to 98.7%. K/Ca is also variable, ranging from 46.0 to 61.8 and averaging around 58. A weighted-mean age of the sample is 1.294 ± 0.010 Ma corresponding to a precision of ~0.4% at 1σ (Table 4). An ideogram of UBT-2 (Figure 13A) indicates significant spread in age among the 19 analyses. At 1σ, achievable analytical error from the NMGRL for a population of 19 sanidines of similar age is ~0.2%. Isochron analysis of this sample gives an age of 1.289 ± 0.028 Ma with a $^{40}Ar/^{36}Ar$ intercept of 293.6 ± 41.69 and an MSWD of 4.71 (Fig. 13B; Table 4). At the 2σ confidence interval, the weighted-mean age is older than previously published $^{40}Ar/^{39}Ar$ sanidine analyses of the Upper Bandelier Tuff plinian deposit (Table 4; 1.235 ± 0.032 Ma; Izett and Obradovich, 1994)

Single-crystal laser-fusion analyses were performed on 35 sanidine crystals from the pumice clast conglomerate of LBT-2. Radiogenic yield ranges from 48.5% to 98.6%. Most samples display >90% radiogenic yields. K/Ca ranges from 24.6 to 52.6 with an average K/Ca of ~35. A weighted-mean age on 35 analyses is 1.607 ± 0.011 Ma (Fig. 14A; Table 4). An isochron of LBT-2 yields an age of 1.606 ± 0.022 Ma with a $^{40}Ar/^{36}Ar$ intercept of 299.3 ± 16.59 and an MSWD of 2.99 (Fig. 14B; Table 4). Both isochron and weighted-mean ages of LBT-2 are consistent at the 2σ confidence level with previously published $^{40}Ar/^{39}Ar$ plinian sanidine analyses of the Lower Bandelier Tuff (1.629 ± 0.022 Ma; Izett and Obradovich, 1994). These findings agree with the correlation made between LBT-2 and the Lower Bandelier Tuff based on electron microprobe chemical fingerprinting by Dunbar (pers. comm., 2000).

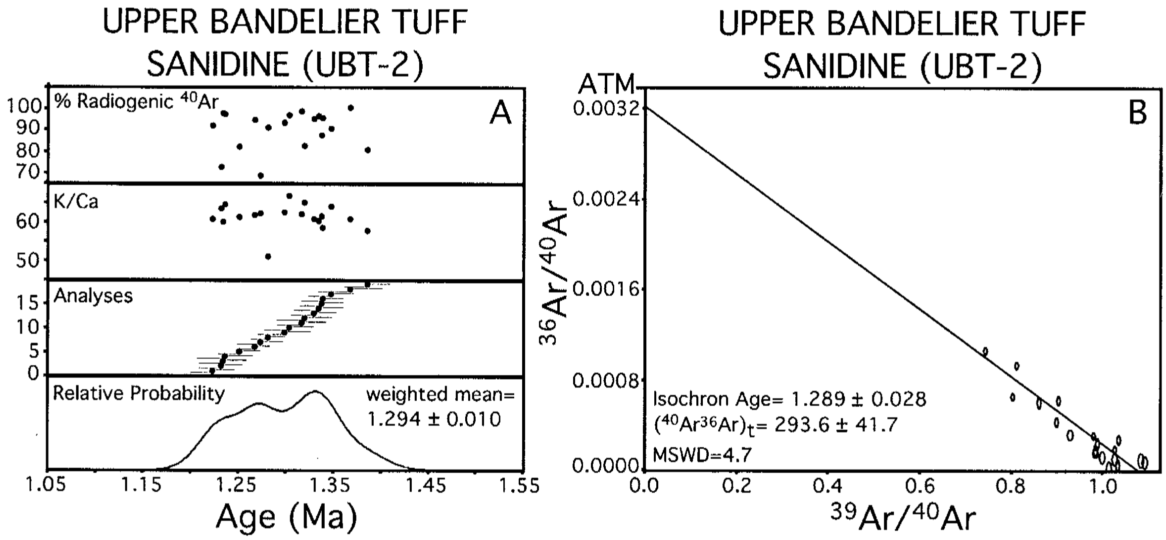

Figure 13. A) Ideogram of single-crystal laser-fusion sanidine results for UBT-2. Values plotted against age include % Radiogenic ^{40}Ar, K/Ca, and ideogram curve. Curve represents the sum of the gaussian probability distributions for individual analyses (Deino and Potts, 1992). B) Isotope correlation diagram of UBT-2 single-crystal laser-fusion analyses. Isochron age, $(^{40}Ar/^{36}Ar)_t$ composition, and MSWD are shown in bottom left corner of diagram. Error ellipses are displayed at the 1σ confidence limits.

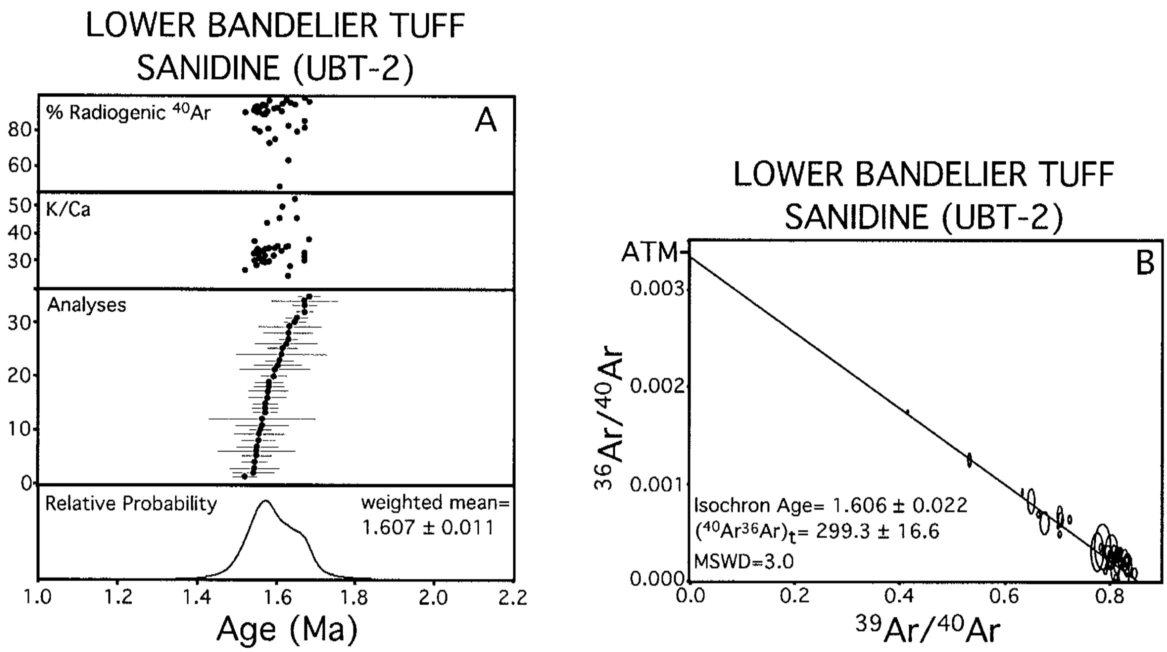

Figure 14. A) Ideogram of single-crystal laser-fusion sanidine results for LBT-2. Values plotted against age include % Radiogenic ^{40}Ar, K/Ca, and ideogram curve. Ideogram curve represents the sum of the gaussian probability distributions for individual analyses (Deino and Potts, 1992). B) Isotope correlation diagram of LBT-2 single-crystal laser-fusion analyses. Isochron age, $(^{40}Ar/^{36}Ar)_t$ composition, and MSWD are shown in bottom left corner of diagram. Error ellipses displayed at 1σ confidence limits.

3.4. Discussion

3.4.1. Evidence for excess argon in MIBQ

EMI-free (TMI-only) quartz crystals from the Bishop and Bandelier Tuff plinian deposits yield laser-step heating ages that are dramatically older than their accepted eruption ages. Plateau and total gas ages for the HF split (TMI-only) of BT-1 are significantly older than apparent ages determined on minimally treated MIBQ by this study and by previous $^{40}Ar/^{39}Ar$ and Rb/Sr studies (van den Bogaard and Schirnick, 1995; Christensen and Halliday, 1996). Furthermore, these TMI-only apparent ages are much older than any crystallization event suggested for the Bishop Tuff magma chamber by previous isotopic studies (Davies and Halliday, 1998, and references therein; Reid and Coath, 2000). The TMI of UBT-1 and LBT-1 MIBQ yield total gas ages (11.54 ± 0.87 Ma and 14.60 ± 1.50 Ma respectively; Table 3) that are an order of magnitude older than their respective eruption ages at 1.235 ± 0.032 Ma and 1.629 ± 0.022 Ma (Table 4). To attribute crystallization age significance to UBT-1 and LBT-1 apparent ages would require magma residence times in excess of 10 m.y.

Apparent $^{40}Ar/^{39}Ar$ ages of MIBQ are interpreted to be a consequence of high $^{40}Ar_E$ concentrations hosted in TMI. As such, these apparent ages do not represent the age of quartz crystallization, and they cannot be used to support or refute long magma residence times for the Bishop Tuff magma chamber.

Numerous studies have documented $^{40}Ar_E$ in volcanic rocks (Allegre et al., 1987; Esser et al., 1997; Renne et al., 1997; McDougall and Harrison, 1999). These findings are indicative of high ^{40}Ar partial pressures in the crust (Esser et al., 1997; Renne et al., 1997). The accumulation of ^{40}Ar in the crust, and the associated increase ^{40}Ar partial pressure, most likely results from the decay of ^{40}K within crustal rocks. Since ^{36}Ar is a stable isotope, with time, it is fixed in concentration relative to an ever-increasing budget of ^{40}Ar. Therefore $^{40}Ar/^{36}Ar$ ratios in the crust are expected to be much higher than that of an atmospheric $^{40}Ar/^{36}Ar$ composition (≈295.5). Elevated argon solubilities in rhyolitic melts (Carroll and Stolper, 1993; Draper and Carroll, 1995) can impart large argon partial pressures and high $^{40}Ar/^{36}Ar$ ratios in rhyolitic magma chambers. This, in turn, can result in high $^{40}Ar_E$ concentrations within melt inclusions of crystallizing phases.

The electron microprobe data presented here (Table 2; Appendix A) indicate that EMI and TMI are compositionally homogeneous with respect to each other and to the matrix glass in host pumice. Furthermore, there is no systematic variation in major element chemistry as a function of melt inclusion siting within quartz or melt inclusion diameter. These data are consistent with the findings of Dunbar and Hervig (1992a,b) and suggest that MIBQ were in chemical equilibrium with their host magma at the time of eruption. While chemical equilibrium does not necessarily require isotopic equilibrium, a recent study of Arrhenius relationships of MIBQ data indicate that, at magmatic temperatures, melt inclusions are non-retentive with respect to argon (Boyce et al., 2000). Collectively these data suggest that, within an active magma chamber, $^{40}Ar_E$ freely diffuses between the rhyolitic melt and quartz-hosted EMI and TMI. This results in homogeneous pre-eruptive concentrations of $^{40}Ar_E$ in all melt inclusions. Upon eruption of MIBQ, EMI apparently fully equilibrate $^{40}Ar_E$ with atmospheric argon ($^{40}Ar_{atm}$; where $^{40}Ar/^{36}Ar$≈295.5) in the plinian eruption column (Fig. 15). Because TMI are surrounded by differing amounts of a more retentive quartz crystal lattice (Boyce et al., 2000), $^{40}Ar_E$ incompletely and heterogeneously equilibrates with $^{40}Ar_{atm}$. This results

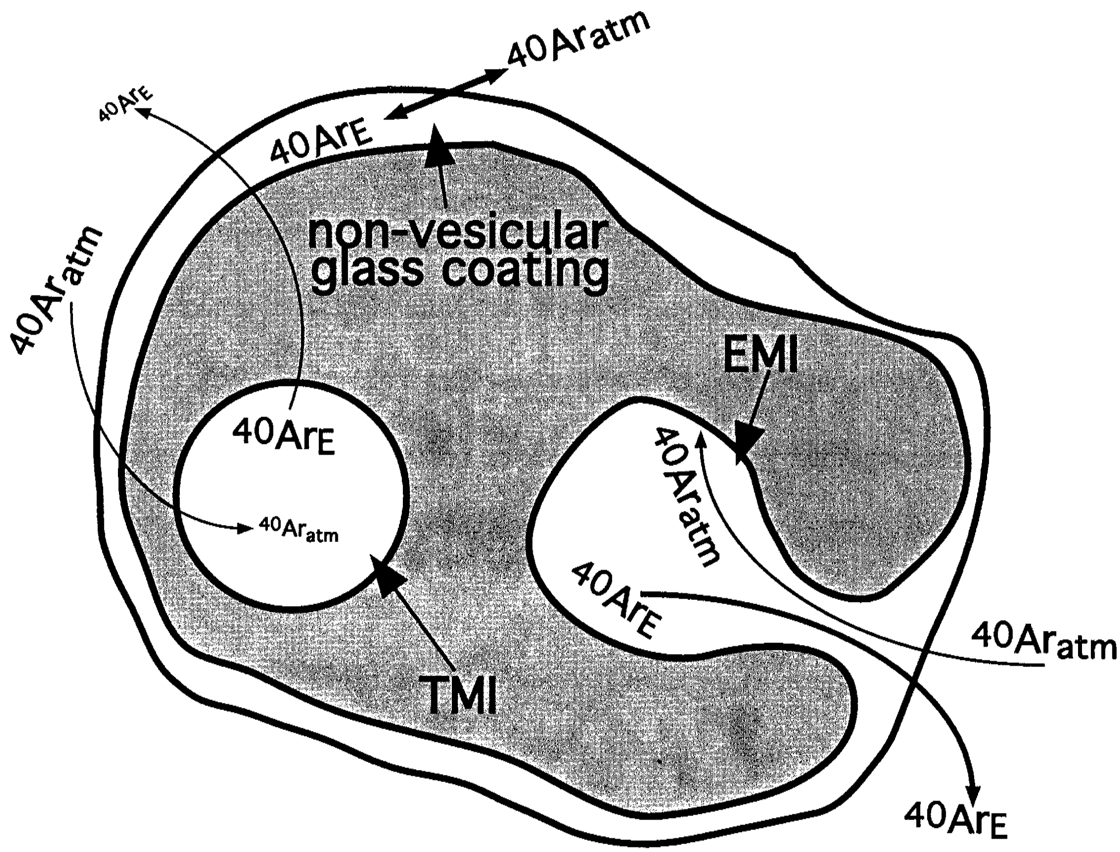

Figure 15. Cartoon of degassing behavior of a hypothetical quartz crystal upon eruption based on data of this study and the diffusion data of Boyce et al. (2000). All glass is assumed to contain a homogeneous distribution of $^{40}Ar_E$ prior to eruption. Thicker flow lines indicate more rapid and larger exchange of argon. Text sizes at beginning and ends of flow arrows indicate relative post-eruptive concentrations of the different types of ^{40}Ar exchanged between reservoirs. Exterior, non-vesicular glass rapidly and completely exchanges its $^{40}Ar_E$ for $^{40}Ar_{atm}$. Hourglass inclusions behave in a similar way and also equilibrate completely, however because of their narrow necks, exchange of $^{40}Ar_{atm}$ for $^{40}Ar_E$ might occur more slowly. Trapped inclusions are surrounded by a more retentive matrix of quartz (Boyce et al., 2000), and therefore exchange of $^{40}Ar_E$ for $^{40}Ar_{atm}$ is slow and limited by the rate of cooling upon eruption. Aging the sample subsequent to eruption will add a radiogenic ^{40}Ar component to all reservoirs. Both single-crystal laser-fusion and step-heating $^{40}Ar/^{39}Ar$ analyses of minimally treated MIBQ such as this will homogenize all of the argon isotopic reservoirs shown.

in a population of TMI that contain variable proportions of their pre-eruptive $^{40}Ar_E$ concentrations (Fig. 15). When EMI are progressively removed from MIBQ, the TMI hosted $^{40}Ar_E$ represents a larger proportion of the total gas released in an analysis. This is manifested in laser step-heating data as older apparent ages from TMI-only (HF-treated and EMI-free) MIBQ. The climbing age spectra observed for MT splits of all MIBQ (Fig. 8) samples reflect the more retentive nature of TMI (Boyce et al., 2000) that release their high $^{40}Ar_E$ concentrations with higher power laser-heating steps.

In both step-heating and total-fusion $^{40}Ar/^{39}Ar$ analyses of minimally treated MIBQ, TMI and EMI argon isotopic reservoirs are partially homogenized. Moreover, because of the heterogeneous and incomplete atmospheric equilibration of TMI upon eruption, $^{40}Ar/^{39}Ar$ apparent ages of TMI-only (HF-treated and EMI-free) MIBQ will represent mixing among TMI hosted variable argon isotopic compositions dominated by $^{40}Ar_E$. Therefore, regardless of whether or not EMI are removed from MIBQ, $^{40}Ar/^{39}Ar$ apparent ages of MIBQ will not reveal crystallization or eruption ages.

A significant contrast between $^{40}Ar_E$ concentrations in the TMI in BT-1 versus those in UBT-1 and LBT-1 is observed. BT-1 TMI contain enough $^{40}Ar_E$ to yield an age 2.9 m.y. older than the Bishop Tuff eruption age at 0.772 ± 0.010 Ma (Izett and Obradovich, 1994). On the other hand, the TMI of UBT-1 and LBT-1 yield ages 10.3 m.y. and 12.9 m.y. older than their respective eruption ages and therefore contain higher concentrations of $^{40}Ar_E$ than BT-1 TMI. HF-treated splits of BT-1, UBT-1, and LBT-1 were used to quantify the moles of $^{40}Ar_E$ per milligram of glass in the TMI of these samples. $^{40}Ar_E$/glass values of 1.83×10^{-14}, 8.03×10^{-14}, and 7.96×10^{-14} moles per milligram are obtained from BT-1(HF), UBT-1(HF), and LBT-1(HF) respectively.

Because some degree of atmospheric equilibration of $^{40}Ar_E$ must occur upon eruption, the calculated $^{40}Ar_E$/glass values represent minimum $^{40}Ar_E$ concentrations in the shallow parts of the pre-eruptive magma chamber and are likely to be underestimates of the true concentrations. I offer two possible explanations for the striking difference in $^{40}Ar_E$ concentrations between these two magma systems: 1) observed discrepancies may result from a difference in pre-eruptive $^{40}Ar_E$ partial pressures in the Bishop and Bandelier magma chambers; and 2) different eruptive processes in the Bishop and Bandelier magma systems may have resulted in different amounts of $^{40}Ar_E$ equilibration with $^{40}Ar_{atm}$.

In support of the first explanation, there is a correlation between the age of magma chamber host-rock and calculated $^{40}Ar_E$ concentrations in the MIBQ of the Bishop and Bandelier Tuffs. The Bishop Tuff magma chamber resided in Jurassic plutons whereas the Bandelier magma chambers were intruded into Precambrian granite. Because ^{40}Ar partial pressures in pre-eruptive magma chambers are ultimately a function of radiogenic ^{40}Ar concentrations in the adjacent crust, older host-rock would be expected to produce higher $^{40}Ar_E$ concentrations in the pre-eruptive MIBQ of such magma chambers.

Argon concentrations in the crust can be incorporated into a magma chamber either by assimilation of wall-rock material or by diffusion of argon. Assuming that 100% of the $^{40}Ar_E$ concentrations observed in the Bishop and Bandelier magmas were to originate from assimilation of their respective wall-rocks, mass balance requires that ~6 km^3 of Jurassic Sierra Nevadan granite and ~2 km^3 of Proterozoic granite were assimilated into the Bishop and Bandelier magma chambers respectively. These volumes of wall-rock assimilation are not unreasonable, however, based on Nd isotopic data from the Bandelier magma system, DePaolo and Perry (1992) suggest that very little, if any, wall-rock assimilation could have occurred in the Bandelier magma chambers.

Diffusion of argon into a magma chamber from K-bearing phases in a wall-rock is a mechanism by which ^{40}Ar concentrations could be increased without significantly modifying other isotopic systems or requiring physical assimilation of crustal material. A pre-eruptive rhyolitic magma body at ~750°C would certainly raise magma chamber wall-rock temperatures to those above the argon closure temperatures of K-feldspar (175°C), biotite (350°C), muscovite (400°C), or hornblende (550°C; M.T. Heizler, 2000, pers. comm.). An argon concentration and/or diffusion gradient between the wall-rock and the crust would likely drive argon diffusion resulting in higher concentrations of ^{40}Ar in a magma chamber.

Conversely, one could also argue in support of the first explanation, that the difference in pre-eruptive $^{40}Ar_E$ concentrations in the Bishop and Bandelier magma chambers are related to differences in their respective geochemical histories. The magma which erupted to form the plinian deposit of the Lower Bandelier Tuff contained higher concentrations of incompatible trace elements, Cl, F, and H_2O than that of the Bishop plinian (Dunbar and Hervig, 1992a,b). This difference could be caused by a greater degree of fractional crystallization in the Lower Bandelier magma chamber than that of the Bishop Tuff. If Ar behaves as an incompatible trace element in rhyolitic magmas, then the higher observed difference in $^{40}Ar_E$ contents of the Bandelier and Bandelier magmas could result from such fractionation processes.

Anderson et al. (1989) suggest that much of the magma that erupted to form the Bishop Tuff may have been saturated with respect to CO_2. The lower concentrations of

$^{40}Ar_E$ in the Bishop Tuff could be related to buffering of Ar by the CO_2-rich vapor phase. However, the portion of the magma that erupted to form the Lower Bandelier Tuff plinian fall deposit appears to have been saturated with respect to an H_2O-rich vapor phase (Dunbar and Hervig, 1992b). Therefore, the difference in $^{40}Ar_E$ concentrations between the Bishop and Bandelier magmas could only be explained if argon fractionated more strongly into a CO_2-rich vapor phase, rather than one dominated by H_2O. There is no data to support this assumption, and hence no evidence to suggest that volatile saturation strongly controlled the observed $^{40}Ar_E$ concentration differences.

Although unlikely, it is possible that the discrepancy in MIBQ $^{40}Ar_E$ concentrations between the Bishop and Bandelier magma systems may be related to differences in the eruptive behavior of these two systems. More rapid quenching of the Upper and Lower Bandelier Tuff plinian eruption columns, relative to that of the Bishop Tuff, might have inhibited diffusive exchange of $^{40}Ar_E$ with $^{40}Ar_{atm}$ in MIBQ. This could result in enhanced preservation of pre-eruptive $^{40}Ar_E$/glass compositions in MIBQ of the Bandelier Tuffs relative to that of the Bishop Tuff. However, examination of Bishop and Bandelier eruption dynamics would suggest otherwise. The plinian column heights of the Bishop and Bandelier eruptions have been modeled from isopach and isopleth maps (Gardner et al., 1991; Self et al., 1996) and detailed stratigraphic comparisons (Wilson and Hildreth, 1997) of their respective plinian deposits. These studies suggest that the Bishop Tuff plinian column reached heights in excess of 45 km compared to the Bandelier plinian columns that in many cases were less than 26 km in height (Self et al., 1996). Dispersal patterns of the Bishop and Bandelier plinian deposits are consistent with higher column heights for the Bishop Tuff relative to that of the Bandelier Tuffs (Sarna-Wojcicki, 1984; Self, 1996).

Assessment of the first-order relationship between column height and plinian cooling would suggest that a higher column height facilitates more rapid quenching of a plinian deposit (Fisher and Schminke, 1984). Therefore the Bishop Tuff would be expected to have cooled more rapidly (albeit on the order of seconds) than that of the Bandelier Tuffs. Considering the diffusion data of Boyce et al. (2000), which suggests that cooling rates on the order of seconds can still allow significant TMI hosted $^{40}Ar_E$ equilibration with $^{40}Ar_{atm}$ in the eruption column, this diffusive exchange should have been greater in the Bandelier Tuffs relative to the Bishop Tuff. If one assumes that both magma systems erupted with the same initial $^{40}Ar_E$ concentrations and that eruption dynamics are the dominant control on observed post-eruptive $^{40}Ar_E$ concentrations in MIBQ TMI, then the Bishop Tuff should exhibit higher $^{40}Ar_E$ concentrations than those of the Bandelier Tuffs. This scenario is inconsistent with the findings presented here. Therefore, although eruption dynamics may play a part in controlling observed $^{40}Ar_E$ concentrations in MIBQ TMI, they must be a second-order effect relative to those imparted by pre-eruptive $^{40}Ar_E$ partial pressures.

Traditionally, isotope correlation diagrams have been used to demonstrate and correct for the presence of $^{40}Ar_E$ in $^{40}Ar/^{39}Ar$ analyses (Heizler and Harrison, 1988; McDougall and Harrison, 1999). There are, however, circumstances where $^{40}Ar_E$ might be undetectable with the isochron method. The $^{40}Ar_E$ identified in MIBQ is correlated to the K and thus $^{39}Ar_K$ released from TMI. In such a scenario, laboratory heating during $^{40}Ar/^{39}Ar$ analyses of MIBQ would release a homogeneous $^{40}Ar_E/^{39}Ar_K$ ratio from TMI.

The addition of $^{40}Ar_{atm}$ to the analyses (e.g. from grain boundaries or cracks) is all that is required to yield a statistically well defined isochron with a trapped $^{40}Ar/^{36}Ar$ composition near atmosphere. An isochron such as this would display a deceptively old apparent age that is not representative of a closed system with respect to radiogenic ^{40}Ar. Such apparently well defined isochrons with low MSWDs caused van den Bogaard and Schirnick (1995) to incorrectly attribute crystallization age significance to their MIBQ laser-fusion data.

3.4.2. Comparison of NMGRL single-crystal laser-fusion MIBQ analyses with the 1995 van den Bogaard and Schirnick study

When performing a comparative study, it is appropriate to demonstrate the reproducibility of a dataset within and among laboratories. Both $^{40}Ar/^{39}Ar$ single-crystal laser-fusion weighted-mean and laser step-heating total gas apparent ages from minimally treated splits of BT-1, UBT-1, and LBT-1 are consistent with each other. The NMGRL uses Fish Canyon Tuff flux monitors (27.84 Ma; Deino and Potts, 1990) that have been calibrated against MMhb-1 (520.4 Ma; Samson and Alexander, 1987). Van den Bogaard and Schirnick (1995) used MMhb-1 as the flux monitor for their MIBQ single-crystal laser-fusion study. Therefore, these two datasets are directly comparable. All else being equal, the NMGRL data is likely to be more precise due to the fact that Fish Canyon Tuff sanidine is a more homogeneous flux monitor when compared to MMhb-1 (Renne et al., 1998). With a minor exception, to be addressed in this section, the MIBQ single-crystal laser-fusion analyses of minimally treated BT-1 are consistent with those of van den Bogaard and Schrinick (1995). This is demonstrative of the interlaboratory reproducibility of the data presented in this paper that would be expected based on flux monitor comparisons and the reasonable assumption of sample similarity between this study and that of van den Bogaard and Schirnick (1995).

The minor inconsistency between the single-crystal laser-fusion MIBQ data presented here and that of van den Bogaard and Schirnick (1995), lies in the trapped $^{40}Ar/^{36}Ar$ compositions of samples represented by these two datasets. The minimally treated split of BT-1 MIBQ presented in this paper yield higher trapped $^{40}Ar/^{36}Ar$ compositions (312 ± 8 in this paper compared to 290 ± 7; van den Bogaard and Schirnick, 1995). Statistically, the isochron defined by the 15 laser-fusion analyses of BT-1 presented here is poorly defined relative to that of van den Bogaard and Schrinick (1995) (MSWD=6.7 vs. 2.2). The larger scatter and lower precision in the single crystal MIBQ data of this paper can result from a number of potential factors. First, more laser-fusion analyses (25) were performed in the van den Bogaard and Schirnick (1995) study. All else being equal, given a normally distributed population with random error, a higher population density will result in a more precise weighted-mean age. On an isotope correlation diagram, a greater population density might serve to lower the MSWD value of the isochron. This can in part account for the observed discrepancy among the two BT-1 MIBQ datasets I present in this paper and that of van den Bogaard and Schirnick (1995). Also, to facilitate fusion of quartz with an Ar ion laser, van den Bogaard and Schirnick (1995) used degassed zero-aged basalt spheres which added ~2.5 x 10^{-15} moles of $^{40}Ar_{atm}$ to each MIBQ single-crystal laser-fusion analysis. This may have helped to anchor the isochron of their single-crystal laser-fusion MIBQ data at an atmospheric $^{40}Ar/^{36}Ar$ intercept. Furthermore, samples from this study were collected from a thicker and more distal fall deposit, later in the Bishop Tuff eruptive sequence than that of van den Bogaard and Schirnick (1995). The parcel of magma that formed the plinian fall deposit from which BT-1 MIBQ were separated spanned potentially deeper and larger depth ranges in the pre-eruptive Bishop Tuff magma chamber. While highly speculative, it is possible that at such depths and ranges of depth, larger temperature, pressure, and isotopic compositional gradients in the pre-eruptive magma chamber imparted greater argon isotopic heterogeneity in TMI and EMI. Given a population of MIBQ crystals, the effect of increased argon isotopic heterogeneity in TMI and EMI would be to introduce a broad distribution of $^{40}Ar/^{36}Ar$ ratios into a dataset and an associated increase in uncertainty on an isochron $^{40}Ar/^{36}Ar$ trapped composition. This may in part account for the discrepancy between the data presented in this study and that of van den Bogaard and Schirnick (1995). However, considering the possibilities outlined above, the single-crystal-laser fusion MIBQ dataset of BT-1 presented here is largely consistent with that of van den Bogaard and Schirnick (1995).

3.4.3. Melt inclusion hosted excess argon and the sanidine problem

The documentation of $^{40}Ar_E$ in MIBQ begs an answer to the question: Are there measurable age effects on melt-inclusion-bearing sanidines known to have crystallized coevally and erupted simultaneously with MIBQ? The Bishop and Bandelier magma systems can potentially answer this question because both are eutectic melt compositions containing abundant sanidine in equilibrium with quartz. Based on the data of Boyce et al. (2000), MIBQ are less retentive of argon than the sanidines (MIBQ E_a = 35 ± 3 kcal/mol; D_o = 0.16; Boyce et al., 2000 vs. sanidine E_a = 43.8 ± 1.0 kcal/mol; D_o =

0.0098; Foland, 1974). Because of this, observed trapped melt inclusions in sanidines of the Bishop and Bandelier plinian deposits may contain similar, if not greater, $^{40}Ar_E$ concentrations compared to those in MIBQ. In fact, $^{40}Ar_E$ concentrations of melt inclusions trapped in sanidines from plinian deposits probably more closely approach those of the pre-eruptive magma chamber than do $^{40}Ar_E$ concentrations in MIBQ TMI. Therefore, $^{40}Ar_E$ concentrations that are derived from MIBQ TMI and are used for sanidine calculations in this section represent minimums and possibly underestimate the true $^{40}Ar_E$ concentrations in post-eruptive plinian sanidine trapped melt inclusions.

To assess the potential effect of $^{40}Ar_E$ on sanidines of the Bishop and Bandelier Tuff plinian deposits, trapped melt inclusion abundances were estimated by point counting. Sanidines from the Bishop, Upper Bandelier, and Lower Bandelier Tuff plinian deposits were found to contain 0.20%, 0.30%, and 0.20% trapped melt inclusions respectively, with a variation of ± 0.16% among different phenocrysts from each unit. Using observed trapped melt inclusion abundances in sanidine from the Bishop and Bandelier plinian deposits, measured $^{40}Ar_E$/glass concentrations in MIBQ TMI, and quoted eruption age best estimates (Izett and Obradovich, 1994); it is estimated that $^{40}Ar_E$ in trapped melt inclusions might increase $^{40}Ar/^{39}Ar$ apparent ages of sanidine by as much as 4 k.y., 38 k.y., and 27 k.y. for the Bishop, Upper Bandelier, and Lower Bandelier Tuffs respectively. These apparent age increases are significantly larger than the 1.2 k.y. apparent age increase ascribed to $^{40}Ar_E$ in sanidines of the 79 A.D. eruption of Mt. Vesuvius (Renne et al., 1997). The magnitudes of $^{40}Ar_E$ induced apparent age increases in sanidine are highly sensitive to the abundance of trapped melt inclusions and K content of both phases. The percent uncertainty on the age of published sanidine data from the

Upper Bandelier Tuff plinian deposit (n=4 yielding a 2.59% uncertainty on an age of 1.235 ± 0.032 Ma; Izett and Obradovich, 1994) is larger than achievable analytical error. Among the three plinian deposits considered here, the Upper Bandelier Tuff has the highest $^{40}Ar_E$/glass ratio in MIBQ. Because of its estimated eruption age and $^{40}Ar_E$ content, rhyolite glass from the Upper Bandelier Tuff MIBQ also has the highest $^{40}Ar_E/^{40}Ar^*$ ratio. Therefore, plinian melt inclusion bearing sanidines of the Upper Bandelier Tuff are the most susceptible to $^{40}Ar_E$-induced age additions in terms of a percent of their true eruption ages.

Figure 16 models the theoretical effects of adding a population of $^{40}Ar_E$-laden trapped melt inclusions to an otherwise $^{40}Ar_E$-free population of 10 sanidines. In this model, the uncertainty on the weighted-mean age of $^{40}Ar_E$-free sanidines is representative of analytical error only, and such sanidines probably best approximate an eruption age. As previously discussed, because $^{40}Ar_E$ is correlated to K and thus $^{39}Ar_K$ in trapped melt inclusions, it will not be observed in the trapped $^{40}Ar/^{36}Ar$ composition on an isochron, but instead will be disguised in a larger error on the weighted-mean or isochron apparent age. However, an increased uncertainty on a weighted-mean or isochron apparent age will only occur if the $^{40}Ar_E$ concentrations in sanidine trapped melt inclusions and/or the melt inclusion abundances in the sanidines are variably distributed among a population of crystals. To model this, the melt inclusion abundances have been randomly distributed among the population of 10 sanidines shown in Figure 16. With a random distribution of trapped melt inclusions, one would expect an equal probability of anywhere from 0% to 100% of some hypothetical maximum abundance. It is stressed here that trapped melt

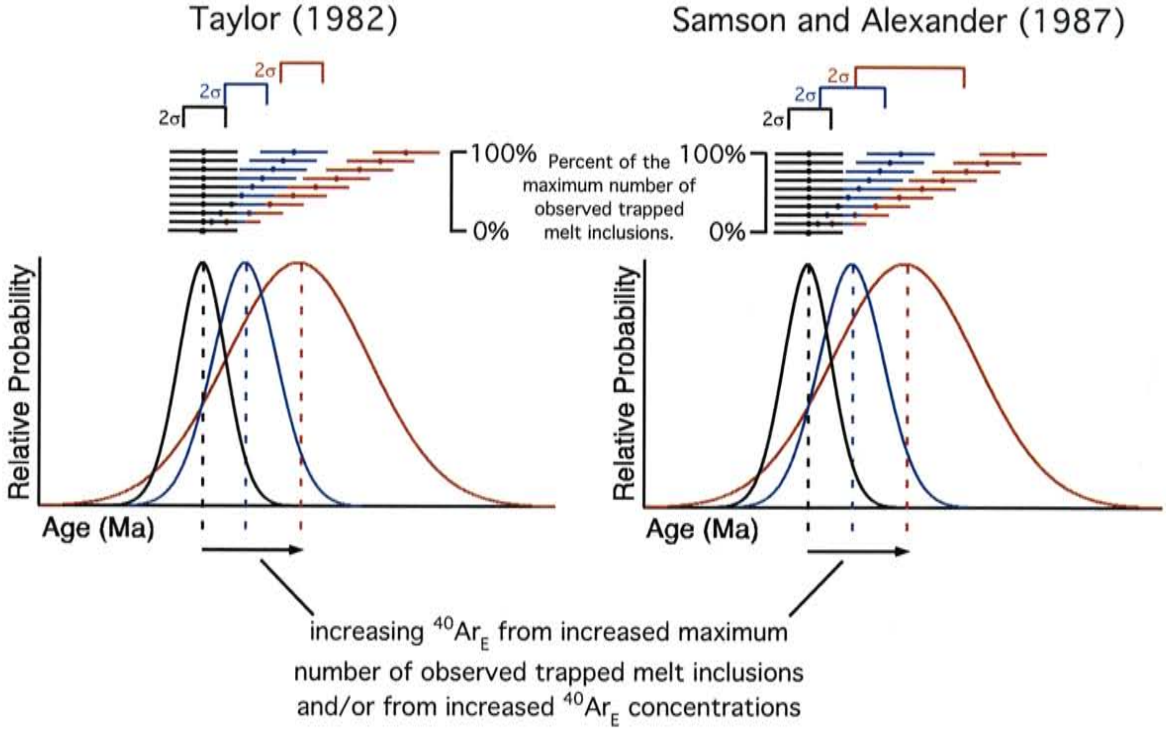

Figure 16. The modeling results (blue and red) of adding a randomly distributed population of trapped melt inclusions, which hosted $^{40}Ar_E$, to a population of melt inclusion-free sanidines (also $^{40}Ar_E$-free) (black). Note that as a function of increasing $^{40}Ar_E$, the analytical error on each analysis is unaffected while the accuracy of the analyses (in their ability to reveal an eruption age) degrades. The amount of scatter introduced among the analyses depends on percentage of a maximum observed abundance of trapped melt inclusions. A randomly distributed population of trapped melt inclusions means there will be an equal probability for all possibilities between 0% and 100% of the maximum observed abundance. The result is an increase in the weighted mean apparent age and also an increase in the width of the gaussian distribution of the weighted mean. Both Taylor (1982) and Samson and Alexander (1987) methods of error regression are shown for comparison. The blue analyses are within 2σ confidence limits of the weighted mean age on $^{40}Ar_E$-free sanidines (black). Red analyses do not display this behavior. Regardless of which method of error regression is used, red analyses apparently surpass a limit at which addition of $^{40}Ar_E$ no longer results in a weighted mean apparent age that is within error of $^{40}Ar_E$-free sanidines.

inclusion-hosted-$^{40}Ar_E$ will not change analytical precision but instead will yield poor accuracy (as well as a shift to older age) on an analysis (Fig. 16).

Consider the sum effects on a weighted-mean (or isochron) apparent age that would result from of a population of sanidine analyses that are shifted to older ages and more broadly distributed as a result of trapped melt inclusion-hosted-$^{40}Ar_E$: one would expect not only an increase in weighted-mean (or isochron) apparent age, but also an increase in the width of the gaussian distribution of apparent age (Fig. 16). Since the uncertainty on individual analyses is unaffected by trapped melt inclusion hosted-$^{40}Ar_E$, the 2σ error limits of the weighted-mean apparent age do not change in terms of absolute uncertainty when the Taylor (1982) method of error regression is applied (Fig. 16). This is because Taylor (1982) assumes that the population in question has already been statistically shown to pass the χ^2 distribution test and to be normally distributed about the mean. In contrast, the Samson and Alexander (1987) method of error regression, accounts for circumstances where the population in question is *not* normally distributed. This is accomplished by increasing the uncertainty on the weighted-mean age (Fig. 16). With either method of error regression, there is a limit to how much $^{40}Ar_E$ can be added to a population of sanidines, before which the uncertainty on the resultant weighted-mean apparent age no longer overlaps at the 2σ confidence limits with the uncertainty on a weighted-mean age of melt inclusion-free ($^{40}Ar_E$-free) sanidines (Fig. 16). Moreover, as the number of analyses (n) in a population increases, there is an associated decrease in the uncertainty on a weighted-mean apparent age or isochron age. Therefore, for a given concentration of $^{40}Ar_E$, the larger the n, the more rapidly uncertainty on an $^{40}Ar_E$-induced weighted-mean apparent age will fall outside the 2σ confidence limits of a weighted-mean age of melt inclusion-free ($^{40}Ar_E$-free) sanidines.

Given the known $^{40}Ar_E$/glass values and melt inclusion abundances in the Bishop and Bandelier Tuffs (determined from MIBQ TMI), as well as for Mt. Vesuvius (Renee et al., 1997) and Mt. Erebus (Esser et al., 1997), a range of effects on populations of sanidine that vary in true eruption age from 1 ka to 100 Ma have been modeled in Figure 17. Melt inclusion abundances for sanidines of the Bishop and Bandelier plinian deposits are bracketed by the point counting determinations quoted in this paper. Mt. Vesuvius and Mt. Erebus trapped melt inclusion abundances are from Esser et al. (1997) and Renee et al. (1997). $^{40}Ar_E$/glass values of high-K phenocrysts (sanidines in all deposits except for Mt. Erebus anorthoclase) were multiplied by their respective ranges in trapped melt inclusion abundances, thereby generating five distinct ranges in absolute $^{40}Ar_E$ concentration. To simplify the model, trapped melt inclusions were assumed to be randomly distributed as was previously discussed. This makes it reasonable to assume an average melt inclusion abundance between 0% and 100% of the maximum number of observed trapped melt inclusions; which translates to an average absolute $^{40}Ar_E$ concentration between 0% and 100% of the maximum concentration. By using the K-Ar age equation, these five different average absolute $^{40}Ar_E$ concentrations have been added to sanidines varying in true eruption age from 1 ka to 100 Ma. The result is the production of $^{40}Ar_E$-induced apparent age additions to the five different 1-ka-to-100-Ma arrays of plinian sanidine populations. Each array of plinian sanidine populations exhibits different amounts of absolute apparent age addition which is a function of its associated absolute $^{40}Ar_E$ concentration. The difference between the $^{40}Ar_E$-induced

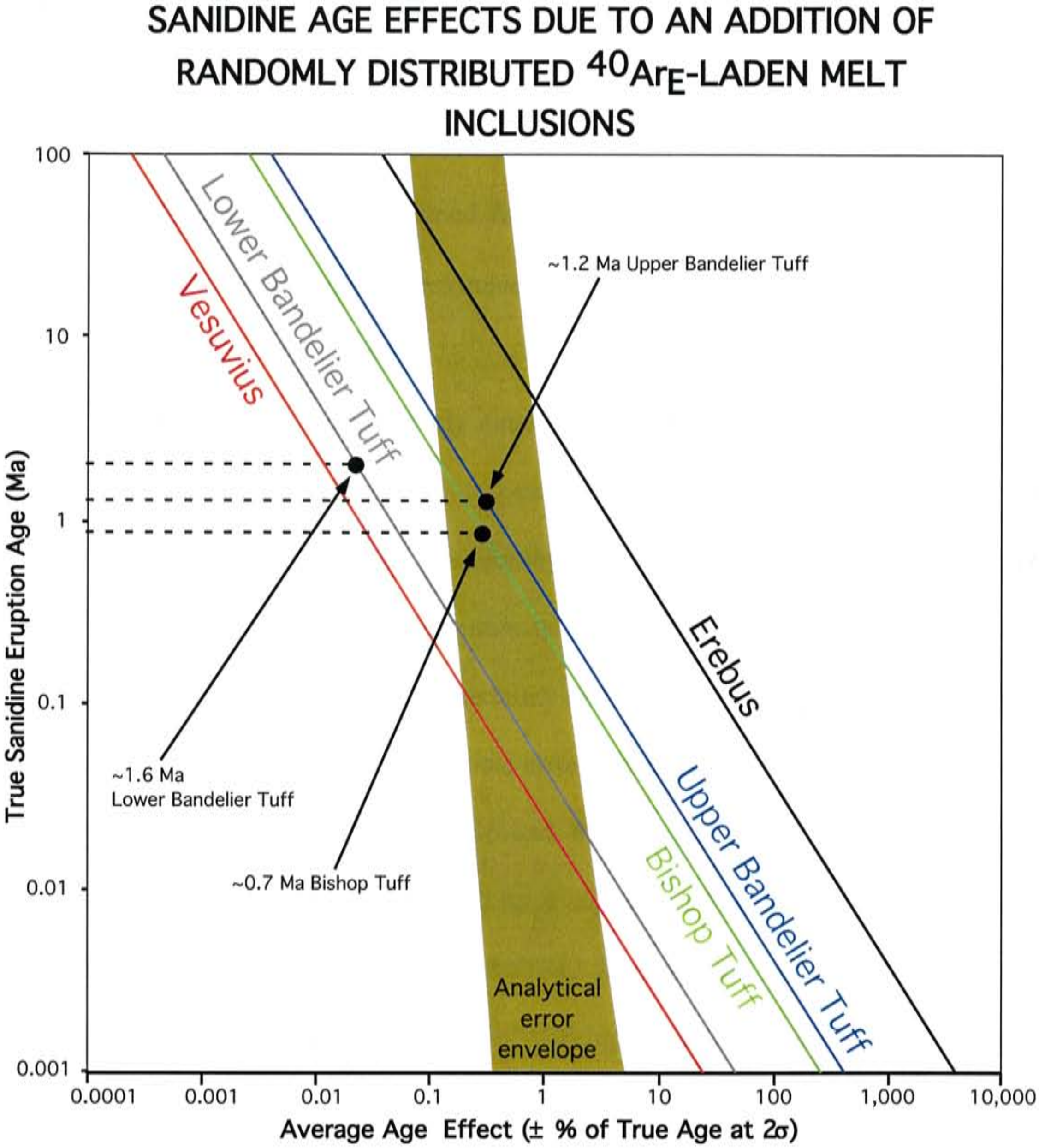

Figure 17. Modeling results of the effect of $^{40}Ar_E$ on sanidines containing a randomly distributed population of $^{40}Ar_E$-laden melt inclusions. Melt inclusion abundances and trapped melt inclusion-hosted-$^{40}Ar_E$ concentrations within sanidines of the Bishop, Upper Bandelier and Lower Bandelier Tuffs, as well as sanidines of Mt. Vesuvius (Renee et al., 1997) and anorthoclase of Mt. Erebus (Esser et al., 1997) were used to generate the modeled data. The curves are labeled with respect to which deposits (and their associated $^{40}Ar_E$ concentrations and melt inclusion abundances) were used. Analytical error envelope estimated from homogeneous and reproducible sanidines of varying ages analyzed at the NMGRL.

apparent age increases and the true sanidine eruption age are represented on the x-axis of Figure 17 as a percent error on the true age. The true sanidine eruption ages are plotted against this on the y-axis. To account for variability which might arise from differing *n*, a population of 15 crystals were assumed for all calculations, and the 1σ errors were divided by the square root of *n* to approximate Taylor (1982) error. The data in Figure 17 are plotted at the 2σ confidence limits.

It is important to quantitatively determine the degree to which increases in a sanidine weighted-mean age due to trapped melt inclusion-hosted-$^{40}Ar_E$ can be distinguished from analytical error. Depending on the achievable analytical precision from the NMGRL facility (which also varies as a function of age; with larger errors on younger analyses), the increased age uncertainty due to $^{40}Ar_E$-laden melt inclusions may or may not be distinguishable from analytical error on an isochron or weighted-mean age of otherwise $^{40}Ar_E$-free sanidines (Figs. 16 and 17). Such $^{40}Ar_E$-free sanidines would either contain no melt inclusions or would have degassed all their $^{40}Ar_E$ upon eruption. Achievable analytical error for the NMGRL facility has been estimated from reproducible and homogeneous sanidines of varying ages, and this analytical error is represented as an envelope at the 2σ confidence limits in Figure 17.

Figure 17 highlights several important effects resulting from the addition of inhomogeneous and randomly distributed $^{40}Ar_E$ to a population of sanidines. Where hypothetical sanidine eruption ages lie to the left of the analytical error envelope, apparent age additions due to $^{40}Ar_E$ will be indistinguishable from analytical error. Where these sanidine eruption ages intersect the analytical error envelope, there is the potential to distinguish $^{40}Ar_E$-induced apparent age additions from analytical error. Lastly where the hypothetical sanidine eruption ages are to the right of the analytical error envelope, the apparent age additions due to $^{40}Ar_E$ should be easily distinguishable from analytical error.

Ideally one would test the modeled data presented here by comparing the $^{40}Ar/^{39}Ar$ sanidine analyses in this paper to known eruption ages. Despite the higher argon retentivities of sanidine relative to MIBQ (McDougall and Harrison, 1999; Boyce et al., 2000), and therefore the greater potential for preservation of pre-eruptive $^{40}Ar_E$ concentrations in the trapped melt inclusions of sanidine, sanidines from ignimbrite deposits are probably a better estimate of an eruption age than those of plinian deposits. As previously discussed, $^{40}Ar_E$ in incompletely degassed sanidine trapped melt inclusions, such as might be found in plinian deposits, can skew $^{40}Ar/^{39}Ar$ apparent ages to those older than the eruption age. Sanidines from ignimbrite deposits, on the other hand, are less sensitive to the problems associated with melt inclusion hosted $^{40}Ar_E$ because these sanidines experience elevated temperatures for weeks to years in a post-eruptive volcanic pile. For example non-welded tuffs of the Valley of 10,000 Smokes in Alaska yielded fumarole temperatures of up to 645°C seven years after emplacement (Fisher and Schminke, 1984). Therefore, sanidines from ignimbrite deposits are likely to have completely degassed all $^{40}Ar_E$ from their trapped melt inclusions. Moreover, since ignimbrite cooling times of weeks or months are unresolvable from the age of eruption by modern radiometric techniques, this becomes a trivial error in what is otherwise a robust estimate of an eruption age.

The existing literature provides limited $^{40}Ar/^{39}Ar$ sanidine age data from ignimbrite deposits of the Bishop and Bandelier Tuffs against which a test of the modeled data presented here can be made. Izett and Obradovich (1994) published a weighted-mean age of 0.757 ± 0.018 Ma on 12 sanidines from the Bishop Tuff ignimbrite. Unfortunately, the only sanidine ages for the Upper and Lower Bandelier Tuff ignimbrites are given by Spell et al. (1990). These may have errors due to the use of an inhomogeneous flux monitor (Bern4M muscovite) and an irradiation package geometry that introduced large uncertainties in J (Izett and Obradovich, 1994; Spell et al., 1996).

It is possible to work backwards from the Bishop Tuff sanidine data presented in this paper, and by subtracting away measured melt inclusion abundances and their associated $^{40}Ar_E$, recalculate an apparent age that would better estimate the Bishop Tuff eruption age. A comparison can then be made between the re-calculated apparent age based on the modeled data and previously published $^{40}Ar/^{39}Ar$ ignimbrite sanidine data for the Bishop Tuff (Figure 18). Within 2σ confidence limits, the recalculated weighted-mean apparent age for the Bishop Tuff is indistinguishable from the uncorrected weighted-mean apparent age of the Bishop Tuff using sanidines from the plinian fall deposits. The recalculated weighted-mean apparent age is also indistinguishable from the $^{40}Ar/^{39}Ar$ weighted-mean apparent age on the Bishop Tuff ignimbrite (0.757 ± 0.018 Ma; Izett and Obradovich, 1994). This is what would be expected from the modeling results in Figure 17, which show that hypothetical sanidines of similar age and trapped melt inclusion-hosted-$^{40}Ar_E$ concentrations to sanidines of the Bishop Tuff plinian deposits (~0.7 Ma) fall to the left of the NMGRL analytical error envelope. Therefore, any $^{40}Ar_E$-induced apparent age additions are indistinguishable from analytical error.

Considering their placement relative to the NMGRL analytical error envelope in Figure 17, modeled sanidines similar in age and trapped melt inclusion-hosted-$^{40}Ar_E$

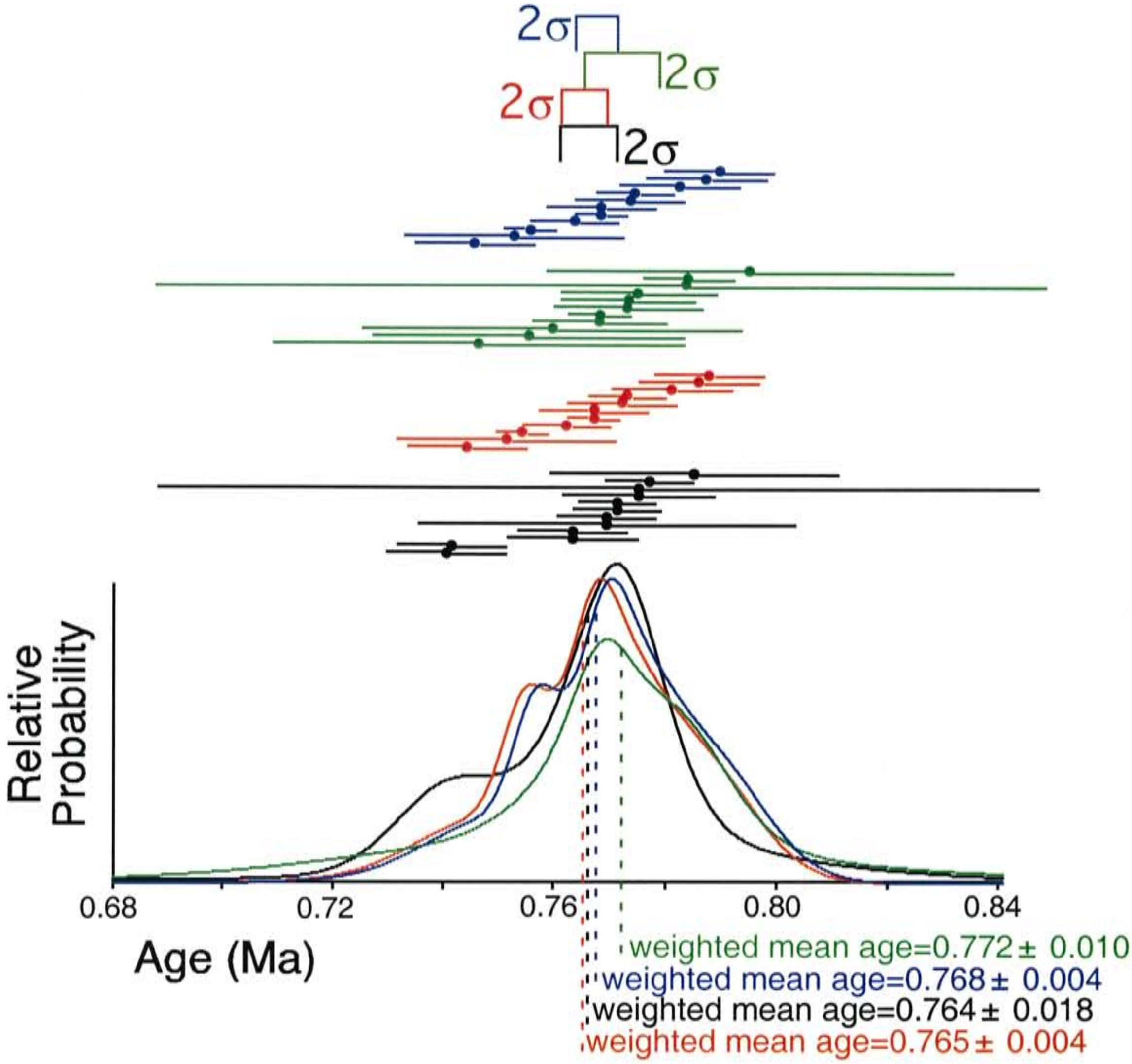

Figure 18. Comparison of the weighted mean age of BT-2 (blue) with the adjusted weighted mean age of BT-2 (red) based on subtraction of $^{40}Ar_E$. This subtraction assumes that BT-2 contains a randomly distributed population of trapped melt inclusions which host $^{40}Ar_E$ concentrations similar to those that have been quantitatively determined by laser step-heating of TMI in BT-1. Melt inclusion abundances in the Bishop Tuff plinian sanidine have been estimated from point counting and are 0.02% with a variation of ± 0.16%. At the 2σ confidence limits, the adjusted weighted mean age of BT-2 is indistinguishable from the raw plinian sanidine data of BT-2. This is consistent with expected behavior of the Bishop Tuff plinian sanidine based on modeled plinian sanidines in Figure 17. Modeled sanidines close to the Bishop Tuff eruption age lie to the left of the NMGRL analytical error envelope, and therefore any apparent age additions due to $^{40}Ar_E$ would not be distinguishable from the analytical error on a population of $^{40}Ar_E$-free sanidines of the Bishop Tuff eruption age. Bishop Tuff plinian (green) and ignimbrite (black) sanidine analyses of Izett and Obradovich (1994) are shown for comparison. All weighted mean ages are within error of each other at 2σ.

concentrations to sanidines of the Lower (~1.6 Ma) and Upper (~1.2 Ma) Bandelier Tuff plinian deposits would be expected to behave differently from those of the Bishop Tuff. Such sanidines that are similar to those of the Upper and Lower Bandelier Tuffs lie on the fringes or within the NMGRL analytical error envelope. Therefore the modeled data in Figure 17 suggest that $^{40}Ar_E$-induced apparent age additions in such sanidines hold the potential to be distinguished from analytical error. This may in part account for the large variability observed among previously published $^{40}Ar/^{39}Ar$ apparent ages of sanidines from the Upper Bandelier Tuff plinian deposits (1.209 ± 0.006 Ma, Spell et al., 1996; 1.235 ± 0.032 Ma, Izett and Obradovich, 1994) and those that are presented here (1.294 ± 0.010 Ma, UBT-2, Table 4). Much of the discrepancy in age between UBT-2 and previously published sanidine analyses of this plinian deposit is larger than what would be expected from melt inclusion-hosted-$^{40}Ar_E$ apparent age additions alone. However it is stressed that MIBQ are less retentive of argon than sanidine, and therefore the model presented here may underestimate actual $^{40}Ar_E$-induced apparent age additions.

It is a strong possibility that the discrepancy in Upper Bandelier Tuff sanidine age is in part due to a population of partially reset xenocrysts. The deposit from which UBT-2 was sampled contains some of the highest crystal contents observed of any pyroclastic deposit in the world (enrichment factor of 7; Self et al., 1996). Many of the phenocrysts are not within the matrix of pumice lapilli, but instead occur as loose crystals in the deposit. These loose phenocrysts might originate in fragments of the eruptive vent-wall that were pulverized and incorporated into the plinian column upon eruption. In such a scenario the xenocrystic sanidines might represent a number of pre-Upper Bandelier Tuff eruptions, such as those of the Cerro Toledo Rhyolite (Spell et al., 1996). Care was taken to exclude these loose crystals and separate sanidines from the pumice lapilli only. However, pumice lapilli were not wire-brushed of crystals adhering to their edges and therefore xenocrystic contamination can not be ruled out as a possibility. Based on the data available, it is difficult to explain the discrepancy among $^{40}Ar/^{39}Ar$ analyses of Upper Bandelier Tuff plinian sanidines.

The observation from the modeled sanidine data (Figs. 16 and 17), that $^{40}Ar_E$ can produce apparent age additions in sanidine that can be larger than analytical error, is extremely important to a variety of dating applications. As shown in Figure 16, for most older sanidines (>100 ka) where the age additions due to $^{40}Ar_E$ are indistinguishable from analytical error, these effects are so small in terms of a percent on the true age, they can be considered negligible (<<0.1%). However young sanidines (<100 ka) hold the potential for large percentages of their true age to be represented in error due to melt inclusion-hosted-$^{40}Ar_E$ (~0.1 to ~1000%). In most of these cases, uncertainties resulting from randomly distributed $^{40}Ar_E$ apparent age additions to a population of sanidines are greater than those of analytical error and can thus be measured. However for the segment of these young sanidines which fall within or below the analytical error envelope of the NMGRL, large errors in age are potentially unresolvable. When one considers that isochron analyses do not readily detect $^{40}Ar_E$ cited within trapped melt inclusions, it is evident that there is a potential to overlook and misguidedly attribute $^{40}Ar_E$-induced errors on a weighted-mean apparent age to analytical uncertainty. In practice, much of this uncertainty might actually be attributable to $^{40}Ar_E$ in melt inclusions.

When performing a study requiring high resolution dating e.g.; a tephrochronologic study or a volcano hazards study on young volcanic sanidines, apparent age increases of 100 ka (for example) that can be manifested as uncertainties unresolvable from analytical error can seriously change such a study's implications and conclusions. $^{40}Ar_E$ in sanidine trapped melt inclusions can be a potential source of large errors; a fact which has not been previously addressed in the literature. Future studies requiring high precision $^{40}Ar/^{39}Ar$ dating of young volcanic rocks need to quantify the effects, where possible, and at least consider the implications of melt inclusion-hosted-$^{40}Ar_E$.

CHAPTER 4. CONCLUSIONS

Laser step-heating $^{40}Ar/^{39}Ar$ analyses of MIBQ from Bishop and Bandelier Tuff plinian fall deposits indicate that significant $^{40}Ar_E$ is present in melt inclusions, particularly those fully trapped within phenocrysts of quartz. The data presented here do not support the interpretations of MIBQ ages from previous $^{40}Ar/^{39}Ar$ or Rb/Sr studies i.e., that the Bishop Tuff magma chamber resided in the crust for >1 Ma (van den Bogaard and Schirnick, 1995; Christensen and Halliday, 1996). MIBQ apparent ages are interpreted to be a consequence of $^{40}Ar_E$ and therefore suggest that they do not represent crystallization or eruption ages. Data presented here are consistent with the findings of Boyce et al. (2000) that melt inclusions in quartz are non-retentive of argon at magmatic temperatures. As a function of melt inclusion siting within retentive quartz phenocrysts, $^{40}Ar_E$ degasses more rapidly from EMI than from TMI upon eruption. This results in inhomogeneous equilibration of $^{40}Ar_E$ with $^{40}Ar_{atm}$ and the formation of multiple argon isotopic reservoirs in MIBQ.

Based on measured $^{40}Ar_E$ concentrations in the TMI of MIBQ, melt inclusions in sanidines from the Bishop and Bandelier Tuffs may also contain $^{40}Ar_E$ capable of increasing sanidine apparent ages by several thousand years relative to actual eruption ages. Modeled age additions are strongly dependent on sanidine melt inclusion abundance, $^{40}Ar_E$ concentrations, and K contents. The potential range of age additions to sanidines of the Bishop, Upper Bandelier, and Lower Bandelier Tuff plinian deposits fall largely within error of their published best eruption age estimates (Izett and Obradovich, 1994). However, in the case of younger (e.g. <100 ka) sanidines, $^{40}Ar_E$ has a much greater potential to significantly affect the accuracy of $^{40}Ar/^{39}Ar$ age determinations.

REFERENCES CITED

ALLEGRE, C.J., Staudacher, T., and Sarda, P., 1987, Rare gas systematics: formation of the atmosphere, evolution and structure of the Earth's mantle: Earth and Planetary Science Letters, v. 81, p. 127-150.

ANDERSON, A.T., Newman, S., Williams, S.N., Druitt, T.H., Skirius, C., Stolper, E., 1989, H_2O, CO_2, Cl, and gas in plinian and ash-flow Bishop rhyolite: Geology, v. 17, p. 221-225.

ANDERSON, A.T., 1991, Hourglass inclusions: Theory and application to the Bishop rhyolitic tuff: American Mineralogist, v. 76, p. 530-547.

ATWATER, T., 1970, Implications of plate tectonics for the Cenozoic tectonic evolution of western North America: Geological Society of America Bulletin, v. 81, p. 3513-3536.

ATWATER, T., and Stock, J., 1998, Pacific-North American plate tectonics of the Neogene southwestern United States: An update: International Geology Review, v. 40, p. 375-402.

BAILEY, R.A., Miller, C.D., and Sieh, K., 1989, Long Valley caldera and Mono-Inyo craters volcanic chain, eastern California: New Mexico Bureau of Mines and Mineral Resources Memoir 47, p. 227-253.

BALDRIDGE, W.S., Keller, G.R., Haak, V., Wendlandt, E., Jiracek, G.R., Olsen, K.H., 1995, The Rio Grande Rift, *in* Olsen, K.H. ed., Continental rifts: Evolution, structure, tectonics: Elsevier, Amsterdam.

BALSLEY, S.D., 1988, The petrology and geochemistry of the Tshirege member of the Bandelier Tuff, Jemez Mountains volcanic field, New Mexico, USA.: M.S. Thesis, Univ. of Tex. Arlington.

BAUER, P., 1999, Personal Communication.

BIERMAN, P.R., Gillespie, A., Whipple, K.X., Clark, D., 1991, Quaternary geomorphology and geochronology of Owens Valley, California; Geological Society of America field trip, *in* Walawender, M.J., Hanan, B.B., eds., Geological excursions in Southern Calilfornia and Mexico, p. 199-223.

BOYCE, J.W., Grove, M., Lovera, O.M., and Reid, M.R., 2000, Argon retentivity of quartz-hosted melt inclusions: Earth and Planetary Science Letters, submitted.

BOYCE, J.W., 2000, Personal Communication.

CARROL, M.R., and Stolper, E.M., 1993, Noble gas solubilities in silicate melts and glasses: New experimental results for argon and the relationship between solubility and ionic porosity: Geochimica et Cosmochimica Acta, v. 57, p. 5039-5051.

CATHER, S.M., Chamberlin, R.M., Chapin, C.E., and McIntosh, W.C., 1994, Stratigraphic consequences of episodic extension in the Lemitar Mountains, central Rio Grande Rift, *in* Keller, G.R., and Cather, S.M., eds., Basins of the Rio Grande Rift: Structure, stratigraphy, and tectonic setting: Boulder, Colorado, Geological Society of America Special Paper 291.

CHAPIN, C.E., and Cather, S.M., 1994, Tectonic setting of the axial basins of the northern and central Rio Grande Rift, *in* Keller, G.R., and Cather, S.M., eds., Basins of the Rio Grande Rift: Structure, stratigraphy, and tectonic setting: Boulder, Colorado, Geological Society of America Special Paper 291.

CHRISTENSEN, J.N., and DePaolo, D.J., 1993, Time scales of large volume silicic magma systems: Sr isotopic systematics of phenocrysts and glass from the Bishop Tuff, Long Valley, California: Contributions to Mineralogy and Petrology, v. 113, p. 100-114.

CHRISTENSEN, J.N., and Halliday, A.N., 1996, Rb-Sr ages and Nd isotopic compositions of melt inclusions from the Bishop Tuff and the generation of silicic magma: Earth and Planetary Science Letters, v. 144, p. 547-561.

DAVIES, G.R., and Halliday, A.N., 1998, Development of the Long Valley rhyolitic magma system: Strontium and neodymium isotope evidence from glasses and individual phenocrysts: Geochimica et Cosmochimica Acta, v. 62, p. 3561-3574.

DEPAOLO, D.J., Perry, F.V., Baldridge, S.W., 1992, Crustal versus mantle sources of granitic magma; a two-parameter model based on Nd isotopic studies, *in* Geological Society of America Special Paper 272, p. 439-446.

DEINO, A., and Potts, R., 1990, Single-Crystal $^{40}Ar/^{39}Ar$ Dating of the Olorgesailie formation, southern Kenya Rift: Journal of Geophysical Research, v. 95, p. 8453-8470.

DEINO, A., and Potts, R., 1992, Age-probability spectra from examination of single-crystal $^{40}Ar/^{39}Ar$ dating results. Examples from Olorgesaille, southern Kenya Rift: Quaternary International, v. 13, p. 47-53.

DRAPER, D.S., and Carroll, M.S., 1995, Argon diffusion and solubility in silicic glasses exposed to an Ar-He gas mixture: Earth and Planetary Science Letters, v. 132, p. 15-24.

DUNBAR, N.W., and Hervig, R.L., 1992a, Petrogenisis and volatile stratigraphy of the Bishop Tuff: Evidence from melt inclusion analysis: Journal of Geophysical Research, v. 97, p. 15129-15150.

DUNBAR, N.W., and Hervig, R.L., 1992b, Volatile and trace element composition of melt inclusions from the Lower Bandelier Tuff: Implications for magma chamber processes and eruptive style: Journal of Geophysical Research, v. 97, p. 15151-15170.

DUNBAR, N.W., 2000, personal communication.

ESSER, R.P., McIntosh, W.C., Heizler, M.T., and Kyle, P.R., 1997, Excess argon in melt inclusions in zero-age anorthoclase feldspar from Mt. Erebus, Antarctica, as revealed by the $^{40}Ar/^{39}Ar$ method: Geochimica et Cosmochimca Acta, v. 61, p. 3789-3801.

FAURE, G., 1986, Principles of Isotope Geology: John Wiley and Sons, New York, 589 p.

FISHER, R.V., and Schmincke, H.U., 1984, Pyroclastic Rocks: Springer-Verlag, Berlin, 472 p.

FOLAND, K.A., 1974, ^{40}Ar diffusion in homogeneous orthoclase and an interpretation of Ar diffusion in K-feldspar: Geochimica et Cosmochimica Acta, v. 38, p. 151-166.

GARDNER, J.E., Sigurdsson, H., and Carey, S.N., 1991, Eruption dynamics and magma withdrawl during the plinian phase of the Bishop Tuff eruption, Long Valley caldera: Journal of Geophysical Research, v. 96, p. 8097-8111.

GOLDICH, S.S., and Fischer, L.B., 1986, Air-abrasion experiments in U-Pb dating of zircon: Chemical Geology, v. 58, p. 195-215.

HALLIDAY, A.N., Mahood, G.A., Holden, P., Metz, J.M., Dempster, T.J., and Davidson, J.P., 1989, Evidence for long residence times of rhyolitic magma in the Long Valley magmatic system: The isotopic record in precaldera lavas of Glass Mountain: Earth and Planetary Science Letters, v. 94, p. 274-290.

HEIZLER, M.T., and Harrison, T.M., 1988, Multiple trapped argon isotope components revealed by $^{40}Ar/^{39}Ar$ isochron analysis: Geochimica et Cosmochimica Acta, v. 52, p. 1295-1303.

HEIZLER, M.T., 2000, personal communication.

HILDRETH, W., 1979, The Bishop Tuff: Evidence for the origin of compositional zonation in silicic magma chambers, *in* Chapin, C.E., and Elston, W.E., eds., Ash-flow tuffs: Geological Society of America Special paper 180, p. 43-70.

HILDRETH, W., 1981, Gradients in silicic magma chambers: Implications for lithospheric magmatism: Journal of Geophysical Research, v. 86, p. 10153-10192.

HUPPERT, H.E, and Sparks, R.S., 1988, The generation of granitic magmas by intrusion of basalt into continental crust: Journal of Petrology, v. 29, p. 599-624.

IZETT, G.A., Wilcox, R.E., and Borchardt, G.A., 1972, Correlation of a volcanic ash bed in Pleistocene deposits near Mount Blanco, Texas, with the Guaje Pumice bed of the Jemez Mountains, New Mexico: Quaternary Research, v. 2, p. 554-578.

IZETT, G.A., 1981, Volcanic ash beds: Recorders of Upper Cenozoic silicic pyroclastic volcanism in the western United States: Journal of Geophysical Research, v. 86, p. 10200-10222.

IZETT, G.A., and Obradovich, J.D., 1994, $^{40}Ar/^{39}Ar$ age constraints for the Jaramillo Normal Subchron and the Matuyama-Brunhes geomagnetic boundary: Journal of Geophysical Research, v. 99, p. 2925-2934.

KNESEL, K.M., Davidson, J.P, and Duffield, W.A., 1999, Evolution of silicic magma through assimilation and subsequent recharge: Evidence from Sr isotopes in sanidine phenocrysts, Taylor Creek Rhyolite, NM: Journal of Petrology, v. 40, p. 773-786.

KUENTZ, D.A., 1986, The Otowi Member of the Bandelier Tuff: A study of the petrology, petrography, and geochemistry of an explosive silicic eruption, Jemez Mountains, New Mexico, M.S. Thesis, Univ. of Tex. Arlington.

LIVACCARI, R.F., 1979, Late Cenozoic tectonic evolution of the western United States: Geology, v. 7, p. 72-75.

METZ, J.M., and Mahood, G.A., 1985, Precursors to the Bishop Tuff eruption: Glass Mountain, Long Valley, California: Journal of Geophysical Research, v. 91, p. 633-652.

METZ, J.M., and Mahood, G.A., 1991, Development of the Long Valley, California, magma chamber recorded in precaldera rhyolite lavas of Glass Mountain: Contributions to Mineralogy and Petrology, v. 106, p. 379-397.

MAHON, K.I., 1996, The New "York" regression: Application of an improved statistical method to geochemistry: International Geology Review, v. 38, p. 293-303.

MCDOUGALL, I., and Harrison, M.T., 1999, Geochronology and Thermochronology by the $^{40}Ar/^{39}Ar$ Method: New York, Oxford University Press, 213 p.

NEILSON, D.L., and Hulen, J.B., 1984, Internal geology and evolution of the Redondo Dome, Valles Caldera, New Mexico: Journal of Geophysical Research, v. 89, p. 8695-8711.

PARSONS, T., 1995, The Basin and Range Province, *in* Olsen, K.H. ed., Continental rifts: Evolution, structure, tectonics: Elsevier, Amsterdam.

REID, M.R., and Coath, C.D., 2000, In situ U-Pb ages of zircons form the Bishop Tuff: No evidence for long crystal residence times: Geology, v. 28, p. 443-446.

RENNE, P.R., Sharp, W.D., Deino, A.L., Orsi, G., and Civetta, L., 1997, $^{40}Ar/^{39}Ar$ dating into the historical realm: Calibration against Pliny the Younger: Science, v. 277, p. 1279-1280.

RENNE, P.R., Swisher, C.C., Deino, A.L., Karner, D.B., Owens, T.L., and DePaolo, D.J., 1998, Intercalibration of standards, absolute ages and uncertainties in $^{40}Ar/^{39}Ar$ dating: Chemical Geology, v. 145, p. 117-152.

SAMSON, S.D., and Alexander, C.E., 1987, Calibration of the interlaboratory $^{40}Ar/^{39}Ar$ dating standard, MMhb-1: Chemical Geology, v. 66, p. 27-34.

SARNA-WOJCICKI, A.M., Bowman, H.R., Meyer, C.E., Russell, P.C., Woodward, M.J., McCoy, G., Rowe, J.J., Baedecker, P.A., Asaro, F., and Michael, H., 1984, Chemical analyses, correlations, and ages of Upper Pliocene and Pleistocene ash layers of east-central and southern California: Geological Survey Professional Paper 1293, 40 p.

SELF, S., Heiken, G., Sykes, M.L., Wohletz, K., Fisher, R.V., and Dethier, D.P., 1996, Field excursions to the Jemez Mountains, New Mexico: New Mexico Bureau of Mines and Mineral Resources, Bulletin 134, 72 p.

SMITH, R.L., and Bailey, R.A., 1966, The Bandelier Tuff--a study of ash-flow eruption cycles from zoned magma chambers: Bulletin of Volcanology, v. 29, p. 83-104.

SMITH, R.L., 1979, Ash-flow magmatism: Geological Society of America Special Paper 180, p. 5-28.

SPARKS, R.S.J., Huppert, H.E., Wilson, C.J.N., 1990, Comment on "Evidence for long residence times of rhyolitic magma in Long Valley magmatic system: the isotopic record in precaldera lavas of Glass Mountain:" Earth and Planetary Science Letters, v. 99, p. 387-389.

SPELL, T.L., Harrison, M.T., and Wolff, J.A., 1990, $^{40}Ar/^{39}Ar$ dating of the Bandelier Tuff and San Diego Canyon ignimbrites, Jemez Mountains, New Mexico: Temporal constraints on magmatic evolution: Journal of Volcanology and Geothermal Research, v. 43, p. 175-193.

SPELL, T.L., McDougall, I., and Doulgeris, A.P., 1996, Cerro Toledo Rhyolite, Jemez Volcanic Field, New Mexico: $^{40}Ar/^{39}Ar$ geochronology of eruptions between two caldera-forming events: Geological Society of America Bulletin, v. 108, p. 1549-1566.

STIX, J., Goff, F., Gorton, M.P., Heiken, G., and Garcia, S., 1988, Restoration of compositional zonation in the Bandelier silicic magma chamber between two caldera-forming eruptions: Geochemistry and origin of the Cerro Toledo Rhyolite, Jemez Mountains, New Mexico: Journal of Geophysical Research, v. 93, p. 6129-6147.

STIX, J., and Gorton, M.P., 1993, Replenishment and crystallization in epicontinental silicic magma chambers: evidence from the Bandelier magmatic system: Journal of Volcanology and Geothermal Research, v. 55, p. 201-215.

TAYLOR, J.R., 1982, An introduction to error analysis: The study of uncertainties in physical measurements: Mill Valley, CA, University Science Books, 327 p.

VAN DEN BOGAARD, P., and Schirnick, C., 1995, $^{40}Ar/^{39}Ar$ laser probe ages of the Bishop Tuff quartz phenocrysts substantiate long-lived silicic magma chamber at Long Valley, United States: Geology, v. 23, p. 759-762.

WEBSTER, J.D., 1992, Water solubility and chlorine partitioning in Cl-rich granitic systems: Effects of melt composition at 2 kbar and 800°C: Geochimica et Cosmochimica Acta, v. 52, p. 679-687.

WILSON, C.J.N., and Hildreth, W., 1997, The Bishop Tuff: New insights from eruptive stratigraphy: Journal of Geology, v. 105, p. 407-439.

WOLFF, J.A., Ramos, F.C., and Davidson, J.P., 1999, Sr isotope disequilibrium during differentiation of the Bandelier Tuff: constraints on the crystallization of a large rhyolitic magma chamber: Geology, v. 27, p. 495-498.

Appendix A. Results of MIBQ electron microprobe analyses.

Sample	SiO_2	TiO_2	Al_2O_3	MnO	FeO	MgO	CaO	Na_2O	K_2O	P_2O_5	SO_2	F	Cl	Total	Beam Size (μm)
Bishop Tuff															
BT-1 QTZ-991101-1	98.96	0.00	0.00	0.02	0.00	0.00	0.01	0.00	0.00	0.04	0.00	0.00	0.01	99.04	25
BT-1 QTZ-991101-2	99.42	0.04	0.00	0.01	0.04	0.02	0.00	0.03	0.01	0.00	0.00	0.00	0.00	99.57	25
BT-1 QTZ-991101-3	99.52	0.00	0.01	0.03	0.00	0.00	0.03	0.00	0.00	0.00	0.00	0.00	0.01	99.60	10
BT-1 QTZ-991101-5	99.28	0.03	0.03	0.00	0.00	0.05	0.03	0.00	0.02	0.00	0.02	0.03	0.00	99.49	25
BT-1 QTZ-991101-6	99.08	0.03	0.02	0.00	0.02	0.01	0.00	0.00	0.00	0.00	0.00	0.00	0.00	99.15	25
BT-1 QTZ-991101-7	99.55	0.00	0.00	0.00	0.05	0.04	0.02	0.00	0.01	0.00	0.04	0.02	0.01	99.74	25
BT-1 QTZ-991101-8	99.18	0.00	0.02	0.06	0.03	0.01	0.01	0.00	0.00	0.00	0.01	0.13	0.00	99.44	25
BT-1 QTZ-991101-16	99.21	0.00	0.01	0.00	0.00	0.00	0.00	0.01	0.01	0.00	0.00	0.00	0.00	99.23	25
BT-1 QTZ-991101-17	98.62	0.05	0.01	0.00	0.00	0.00	0.00	0.00	0.00	0.00	0.04	0.00	0.03	98.75	25
BT-1 QTZ-991101-19	99.88	0.04	0.00	0.00	0.00	0.00	0.01	0.00	0.01	0.00	0.00	0.03	0.01	99.99	25
BT-1 QTZ-991101-20	99.62	0.03	0.00	0.00	0.02	0.00	0.01	0.02	0.01	0.00	0.02	0.06	0.01	99.80	10
BT-1 QTZ-991101-22	99.11	0.00	0.01	0.04	0.00	0.02	0.02	0.00	0.01	0.00	0.06	0.05	0.02	99.33	25
BT-1 QTZ-991101-23	99.49	0.01	0.01	0.03	0.08	0.00	0.02	0.01	0.00	0.02	0.00	0.00	0.01	99.67	25
BT-1 QTZ-991101-24	98.95	0.00	0.02	0.02	0.03	0.05	0.00	0.00	0.00	0.03	0.02	0.03	0.00	99.14	25
BT-1 QTZ-991101-30	99.61	0.06	0.00	0.00	0.00	0.00	0.02	0.02	0.02	0.00	0.00	0.00	0.01	99.75	25
BT-1 QTZ-991101-31	99.56	0.03	0.00	0.03	0.00	0.04	0.00	0.01	0.03	0.00	0.00	0.13	0.00	99.83	25
BT-1 QTZ-991101-32	99.35	0.00	0.02	0.00	0.01	0.00	0.00	0.00	0.02	0.00	0.00	0.00	0.00	99.40	25
BT-1 QTZ-991101-33	99.84	0.00	0.03	0.05	0.00	0.01	0.01	0.00	0.00	0.00	0.01	0.00	0.00	99.95	25
BT-1 QTZ-991101-40	98.41	0.02	0.00	0.04	0.02	0.00	0.01	0.01	0.00	0.02	0.01	0.00	0.00	98.54	25
BT-1 QTZ-991101-51	99.36	0.02	0.01	0.00	0.00	0.01	0.01	0.02	0.00	0.00	0.00	0.00	0.01	99.43	25
BT-1 QTZ avg n=20	**99.30**	**0.02**	**0.01**	**0.02**	**0.01**	**0.01**	**0.01**	**0.01**	**0.01**	**0.01**	**0.01**	**0.02**	**0.01**	**99.44**	
Std. Dev.	**0.38**	**0.02**	**0.01**	**0.02**	**0.02**	**0.02**	**0.01**	**0.01**	**0.01**	**0.01**	**0.02**	**0.04**	**0.01**	**0.38**	
BT-1-1 TMI-991101-9	73.15	0.06	12.13	0.02	0.62	0.00	0.37	3.34	4.32	0.02	0.00	0.03	0.07	94.12	25
BT-1-1 TMI-991101-10	73.61	0.01	12.09	0.00	0.55	0.01	0.40	3.41	4.29	0.05	0.00	0.05	0.08	94.55	25
BT-1-1 TMI-991101-11	72.19	0.05	12.06	0.06	0.55	0.03	0.39	3.46	4.32	0.04	0.00	0.11	0.08	93.34	25
BT-1-1 TMI-991101-12	72.75	0.05	12.13	0.00	0.68	0.05	0.44	3.54	4.29	0.01	0.03	0.09	0.06	94.12	25
BT-1-1 TMI-991101-13	72.95	0.03	12.18	0.00	0.60	0.03	0.42	3.41	4.25	0.02	0.01	0.04	0.07	93.99	25
BT-1-1 TMI-991101-14	72.52	0.06	12.14	0.03	0.63	0.06	0.40	3.28	4.33	0.00	0.00	0.07	0.08	93.59	20
BT-1-1 TMI-991101-38	72.88	0.03	12.16	0.00	0.61	0.06	0.40	3.37	4.33	0.00	0.00	0.15	0.07	94.05	25
BT-1-1 TMI-991101-39	73.44	0.08	12.35	0.05	0.60	0.01	0.45	3.35	4.27	0.01	0.01	0.04	0.10	94.75	25
BT-1 TMI avg n=8	**72.93**	**0.05**	**12.15**	**0.02**	**0.60**	**0.03**	**0.41**	**3.40**	**4.30**	**0.02**	**0.01**	**0.07**	**0.07**	**94.06**	
Std. Dev.	**0.47**	**0.02**	**0.09**	**0.02**	**0.04**	**0.02**	**0.03**	**0.08**	**0.03**	**0.02**	**0.01**	**0.04**	**0.01**	**0.46**	
BT-1 EMI-991101-25	73.48	0.05	12.12	0.00	0.56	0.00	0.43	3.36	4.75	0.01	0.00	0.14	0.05	94.94	25
BT-1 EMI-991101-26	74.76	0.06	12.24	0.00	0.50	0.00	0.43	3.65	4.35	0.03	0.03	0.00	0.08	96.14	20
BT-1 EMI-991101-27	75.77	0.07	12.63	0.01	0.58	0.02	0.41	3.06	3.89	0.00	0.00	0.00	0.09	96.51	10
BT-1 EMI-991101-28	76.43	0.08	12.59	0.02	0.60	0.01	0.40	3.43	3.59	0.00	0.02	0.17	0.08	97.39	10
BT-1 EMI-991101-29	73.09	0.07	12.18	0.07	0.70	0.00	0.43	3.45	4.30	0.04	0.00	0.10	0.08	94.50	25
BT-1 EMI-991101-36	73.93	0.06	11.85	0.00	0.60	0.01	0.35	2.92	5.09	0.03	0.00	0.14	0.09	95.06	20
BT-1 EMI-991101-37	73.93	0.01	11.93	0.00	0.63	0.03	0.39	2.73	4.62	0.00	0.00	0.04	0.09	94.39	20
BT-1 EMI-991101-41	73.19	0.01	12.19	0.00	0.65	0.01	0.37	3.56	4.26	0.00	0.03	0.00	0.08	94.35	25
BT-1 EMI-991101-42	72.97	0.08	12.19	0.00	0.59	0.00	0.36	3.48	4.40	0.00	0.00	0.03	0.08	94.18	25
BT-1 EMI-991101-43	71.91	0.02	11.74	0.07	0.63	0.02	0.39	2.80	4.96	0.00	0.02	0.11	0.09	92.76	20
BT-1 EMI-991101-44	72.69	0.05	11.82	0.01	0.63	0.00	0.41	2.75	5.01	0.06	0.02	0.14	0.08	93.66	25
BT-1 EMI-991101-45	72.94	0.12	11.95	0.00	0.59	0.02	0.45	2.85	4.99	0.00	0.02	0.06	0.07	94.06	25
BT-1 EMI-991101-46	72.57	0.08	11.82	0.00	0.60	0.00	0.39	2.89	5.11	0.00	0.00	0.00	0.06	93.52	25
BT-1 EMI-991101-49	72.72	0.09	12.00	0.01	0.63	0.06	0.42	2.88	4.92	0.00	0.00	0.08	0.07	93.88	25
BT-1 EMI-991101-50	73.02	0.02	12.19	0.05	0.63	0.08	0.41	2.85	4.91	0.02	0.00	0.00	0.07	94.24	25
BT-1 EMI-991101-52	73.60	0.04	12.34	0.01	0.55	0.02	0.39	3.04	4.96	0.00	0.04	0.15	0.09	95.23	25
BT-1 EMI-991101-53	74.12	0.03	12.44	0.01	0.61	0.00	0.41	2.83	5.09	0.03	0.00	0.26	0.08	95.90	25
BT-1 EMI-991101-54	75.37	0.09	12.24	0.01	0.58	0.01	0.42	2.87	4.86	0.00	0.02	0.11	0.07	96.64	20
BT-1 EMI avg n=18	**73.69**	**0.06**	**12.14**	**0.01**	**0.60**	**0.02**	**0.40**	**3.08**	**4.67**	**0.01**	**0.01**	**0.08**	**0.08**	**94.85**	
Std. Dev.	**1.20**	**0.03**	**0.26**	**0.02**	**0.04**	**0.02**	**0.03**	**0.31**	**0.44**	**0.02**	**0.01**	**0.07**	**0.01**	**1.24**	

Appendix A. Results of MIBQ electron microprobe analyses.

Sample	SiO_2	TiO_2	Al_2O_3	MnO	FeO	MgO	CaO	Na_2O	K_2O	P_2O_5	SO_2	F	Cl	Total	Beam Size (μm)
Upper Bandelier Tuff															
UBT-1 QTZ-991101-1	98.89	0.00	0.00	0.00	0.03	0.03	0.00	0.00	0.01	0.01	0.00	0.00	0.00	98.98	25
UBT-1 QTZ-991101-2	99.31	0.05	0.02	0.00	0.00	0.05	0.00	0.00	0.02	0.00	0.00	0.07	0.00	99.52	25
UBT-1 QTZ-991101-3	99.69	0.00	0.01	0.00	0.00	0.00	0.01	0.00	0.01	0.00	0.00	0.00	0.01	99.73	25
UBT-1 QTZ-991101-4	98.70	0.00	0.01	0.00	0.00	0.00	0.00	0.01	0.00	0.00	0.05	0.00	0.00	98.77	25
UBT-1 QTZ-991101-5	100.13	0.00	0.00	0.02	0.00	0.04	0.03	0.01	0.00	0.00	0.00	0.00	0.00	100.23	25
UBT-1 QTZ-991101-8	99.09	0.00	0.00	0.00	0.00	0.00	0.02	0.01	0.00	0.01	0.00	0.00	0.00	99.13	25
UBT-1 QTZ-991101-9	99.16	0.00	0.00	0.00	0.00	0.00	0.01	0.01	0.02	0.00	0.00	0.02	0.00	99.23	25
UBT-1 QTZ-991101-10	99.03	0.02	0.04	0.04	0.00	0.05	0.00	0.00	0.00	0.00	0.04	0.00	0.00	99.22	25
UBT-1 QTZ avg n=8	**99.25**	**0.01**	**0.01**	**0.01**	**0.00**	**0.02**	**0.01**	**0.01**	**0.01**	**0.00**	**0.01**	**0.01**	**0.00**	**99.35**	
Std. Dev.	**0.46**	**0.02**	**0.01**	**0.02**	**0.01**	**0.02**	**0.01**	**0.01**	**0.01**	**0.00**	**0.02**	**0.02**	**0.00**	**0.46**	
UBT-1 TMI-991101-13	72.04	0.04	11.71	0.04	1.38	0.00	0.22	3.99	4.16	0.00	0.02	0.26	0.33	94.19	25
UBT-1 TMI-000726-1	73.38	0.10	12.00	0.06	1.31	0.00	0.25	3.99	4.31	0.00	0.00	0.38	0.26	96.04	25
UBT-1 TMI-000726-2	74.14	0.00	11.63	0.01	1.26	0.00	0.22	4.02	4.33	0.00	0.00	0.39	0.29	96.30	25
UBT-1 TMI-000726-3	73.89	0.10	11.84	0.14	1.30	0.00	0.22	3.85	4.16	0.00	0.00	0.22	0.27	95.99	25
UBT-1 TMI-000726-4	73.65	0.08	11.70	0.00	1.32	0.00	0.23	3.92	4.24	0.05	0.00	0.41	0.27	95.87	25
UBT-1 TMI-000726-5	73.55	0.07	12.03	0.04	1.22	0.00	0.27	4.22	4.14	0.02	0.00	0.28	0.26	96.11	25
UBT-1 TMI-000726-6	72.83	0.05	12.27	0.09	1.24	0.01	0.28	4.26	4.36	0.01	0.01	0.23	0.30	95.95	25
UBT-1 TMI-000726-7	73.36	0.05	11.91	0.04	1.40	0.00	0.27	4.22	4.23	0.00	0.00	0.32	0.31	96.11	25
UBT-1 TMI-000726-8	74.03	0.03	11.79	0.01	1.35	0.00	0.22	4.10	4.36	0.03	0.01	0.40	0.28	96.62	25
UBT-1 TMI-000726-9	74.04	0.03	11.86	0.06	1.43	0.00	0.23	4.04	4.22	0.00	0.01	0.33	0.26	96.50	25
UBT-1 TMI-000726-10	72.83	0.03	11.77	0.09	1.33	0.00	0.25	3.97	4.26	0.01	0.00	0.30	0.27	95.12	25
UBT-1 TMI-000726-11	73.59	0.05	11.81	0.08	1.38	0.01	0.20	3.92	4.29	0.04	0.00	0.16	0.27	95.79	25
UBT-1 TMI avg n=12	**73.44**	**0.05**	**11.86**	**0.05**	**1.33**	**0.00**	**0.24**	**4.04**	**4.25**	**0.01**	**0.00**	**0.31**	**0.28**	**95.88**	
Std. Dev.	**0.62**	**0.03**	**0.17**	**0.04**	**0.07**	**0.00**	**0.02**	**0.13**	**0.08**	**0.02**	**0.01**	**0.08**	**0.02**	**0.65**	
UBT-1 EMI-000726-2	73.30	0.01	11.92	0.01	1.25	0.00	0.25	4.43	4.23	0.00	0.00	0.26	0.28	95.95	25
UBT-1 EMI-000726-3	72.50	0.02	11.79	0.00	1.23	0.02	0.28	3.93	4.64	0.00	0.03	0.39	0.25	95.07	25
UBT-1 EMI-000726-4	73.00	0.03	11.98	0.13	1.31	0.01	0.27	3.96	4.53	0.06	0.00	0.20	0.28	95.76	25
UBT-1 EMI-000726-5	74.45	0.09	11.94	0.07	1.32	0.02	0.25	4.41	4.04	0.01	0.01	0.27	0.25	97.11	25
UBT-1 EMI-000726-6	73.70	0.04	11.82	0.00	1.37	0.00	0.24	4.22	4.21	0.01	0.01	0.20	0.26	96.07	25
UBT-1 EMI-000726-7	72.60	0.06	11.74	0.09	1.32	0.01	0.29	4.28	4.18	0.06	0.02	0.26	0.28	95.18	25
UBT-1 EMI-000726-8	73.99	0.06	11.94	0.00	1.36	0.01	0.27	4.42	4.28	0.00	0.02	0.38	0.27	96.98	25
UBT-1 EMI-000726-9	73.42	0.06	11.86	0.15	1.37	0.00	0.20	4.41	4.26	0.00	0.00	0.30	0.29	96.30	25
UBT-1 EMI-000726-10	73.71	0.06	11.81	0.02	1.29	0.01	0.25	4.20	4.19	0.00	0.00	0.32	0.25	96.10	25
UBT-1 EMI-000726-11	72.82	0.04	11.86	0.00	1.43	0.01	0.26	4.25	4.19	0.01	0.00	0.26	0.30	95.42	25
UBT-1 EMI-000726-12	72.72	0.02	11.87	0.08	1.40	0.02	0.24	4.33	4.30	0.00	0.00	0.17	0.28	95.43	25
UBT-1 EMI-000726-13	74.05	0.03	11.80	0.00	1.30	0.01	0.27	4.22	4.17	0.01	0.02	0.35	0.25	96.47	25
UBT-1 EMI avg n=12	**73.36**	**0.04**	**11.86**	**0.05**	**1.33**	**0.01**	**0.26**	**4.26**	**4.27**	**0.01**	**0.01**	**0.28**	**0.27**	**95.99**	
Std. Dev.	**0.61**	**0.02**	**0.07**	**0.05**	**0.06**	**0.01**	**0.02**	**0.16**	**0.16**	**0.02**	**0.01**	**0.07**	**0.02**	**0.63**	

Appendix A. Results of MIBQ electron microprobe analyses.

Sample	SiO_2	TiO_2	Al_2O_3	MnO	FeO	MgO	CaO	Na_2O	K_2O	P_2O_5	SO_2	F	Cl	Total	Beam Size (µm)
Lower Bandelier Tuff															
LBT-1 QTZ-991101-1	99.08	0.02	0.00	0.02	0.03	0.03	0.02	0.00	0.03	0.02	0.02	0.21	0.00	99.47	25
LBT-1 QTZ-991101-2	99.84	0.01	0.01	0.00	0.03	0.07	0.01	0.02	0.00	0.00	0.02	0.00	0.00	100.00	25
LBT-1 QTZ-991101-9	99.28	0.03	0.00	0.00	0.01	0.00	0.03	0.00	0.01	0.02	0.00	0.03	0.00	99.42	25
LBT-1 QTZ-991101-13	100.05	0.03	0.02	0.00	0.00	0.00	0.00	0.00	0.01	0.00	0.00	0.03	0.00	100.13	25
LBT-1 QTZ-991101-16	99.71	0.02	0.01	0.01	0.00	0.01	0.02	0.00	0.01	0.00	0.00	0.06	0.00	99.86	25
LBT-1 QTZ-991101-17	99.55	0.00	0.01	0.04	0.00	0.00	0.01	0.02	0.00	0.01	0.05	0.09	0.00	99.77	25
LBT-1 QTZ-991101-18	99.44	0.00	0.02	0.00	0.02	0.00	0.00	0.00	0.01	0.00	0.00	0.00	0.02	99.50	5
LBT-1 QTZ-991101-19	99.85	0.03	0.01	0.00	0.00	0.00	0.01	0.00	0.00	0.04	0.00	0.00	0.02	99.96	25
LBT-1 QTZ-991101-21	100.02	0.00	0.01	0.00	0.00	0.03	0.00	0.00	0.00	0.00	0.01	0.14	0.00	100.20	25
LBT-1 QTZ-991101-22	99.68	0.00	0.02	0.00	0.00	0.06	0.02	0.00	0.01	0.00	0.04	0.00	0.01	99.84	25
LBT-1 QTZ-991101-24	99.36	0.02	0.02	0.00	0.00	0.00	0.00	0.01	0.02	0.01	0.00	0.00	0.01	99.46	25
LBT-1 QTZ avg n=11	**99.62**	**0.01**	**0.01**	**0.01**	**0.01**	**0.02**	**0.01**	**0.00**	**0.01**	**0.01**	**0.01**	**0.05**	**0.01**	**99.78**	
Std. Dev.	**0.31**	**0.01**	**0.01**	**0.01**	**0.01**	**0.03**	**0.01**	**0.01**	**0.01**	**0.01**	**0.02**	**0.07**	**0.01**	**0.28**	
LBT-1 TMI-991101-3	72.51	0.00	11.93	0.07	1.20	0.11	0.22	4.08	4.21	0.00	0.00	0.13	0.25	94.73	25
LBT-1 TMI-991101-4	72.25	0.03	11.86	0.02	1.12	0.01	0.25	4.02	4.06	0.00	0.01	0.33	0.23	94.19	25
LBT-1 TMI-991101-5	72.43	0.04	11.85	0.10	1.31	0.00	0.23	4.06	4.11	0.01	0.00	0.14	0.21	94.49	25
LBT-1 TMI-991101-7	72.86	0.01	12.05	0.05	1.18	0.01	0.21	3.78	4.21	0.02	0.00	0.22	0.22	94.81	20
LBT-1 TMI-991101-8	74.29	0.03	11.73	0.10	1.24	0.00	0.28	3.89	4.02	0.03	0.02	0.20	0.18	96.00	20
LBT-1 TMI-991101-12	72.90	0.05	11.90	0.00	1.13	0.00	0.26	4.09	4.07	0.02	0.03	0.41	0.22	95.07	25
LBT-1 TMI-991101-14	73.36	0.06	11.83	0.04	1.16	0.00	0.23	4.07	4.12	0.02	0.02	0.23	0.18	95.31	25
LBT-1 TMI-991101-15	72.94	0.04	11.89	0.10	1.12	0.02	0.24	4.04	4.16	0.00	0.02	0.09	0.20	94.87	25
LBT-1 TMI-000726-1	73.48	0.07	11.85	0.03	1.22	0.00	0.19	3.49	4.13	0.00	0.00	0.27	0.22	94.96	25
LBT-1 TMI-000726-2	73.41	0.05	11.90	0.02	1.18	0.00	0.21	3.49	3.98	0.01	0.01	0.25	0.20	94.70	25
LBT-1 TMI-000726-3	73.10	0.05	11.80	0.09	1.20	0.00	0.20	3.22	3.90	0.01	0.01	0.32	0.23	94.12	25
LBT-1 TMI-000726-4	73.31	0.05	11.86	0.00	1.20	0.00	0.23	4.03	3.99	0.05	0.01	0.21	0.21	95.15	25
LBT-1 TMI-000726-5	72.93	0.05	11.84	0.03	1.17	0.00	0.21	3.87	4.10	0.00	0.01	0.37	0.23	94.83	25
LBT-1 TMI-000726-6	72.96	0.00	11.67	0.01	1.20	0.00	0.26	4.01	4.07	0.02	0.00	0.31	0.20	94.72	25
LBT-1 TMI-000726-7	74.09	0.12	11.84	0.03	1.14	0.00	0.22	3.16	3.95	0.00	0.02	0.28	0.20	95.05	25
LBT-1 TMI avg n=15	**73.12**	**0.04**	**11.85**	**0.05**	**1.19**	**0.01**	**0.23**	**3.82**	**4.07**	**0.01**	**0.01**	**0.25**	**0.21**	**94.87**	
Std. Dev.	**0.56**	**0.03**	**0.09**	**0.04**	**0.05**	**0.03**	**0.02**	**0.32**	**0.09**	**0.01**	**0.01**	**0.09**	**0.02**	**0.45**	
LBT-1 EMI-000726-1	74.07	0.04	11.93	0.13	1.20	0.01	0.20	4.49	3.62	0.03	0.00	0.35	0.22	96.28	25
LBT-1 EMI-000726-3	74.02	0.00	11.97	0.02	1.19	0.01	0.21	4.48	3.84	0.00	0.00	0.29	0.21	96.22	25
LBT-1 EMI-000726-2	73.93	0.06	11.92	0.02	1.20	0.00	0.25	4.57	3.84	0.00	0.02	0.24	0.22	96.27	25
LBT-1 EMI-000726-4	72.95	0.06	11.94	0.06	1.15	0.00	0.25	3.38	3.71	0.00	0.01	0.12	0.22	93.85	25
LBT-1 EMI-000726-5	75.08	0.08	12.23	0.04	1.21	0.00	0.21	4.62	4.00	0.04	0.02	0.33	0.23	98.08	25
LBT-1 EMI-000726-6	74.52	0.04	12.10	0.00	1.22	0.00	0.24	4.38	3.88	0.00	0.01	0.07	0.23	96.68	25
LBT-1 EMI-000726-7	74.45	0.05	11.79	0.11	1.26	0.00	0.23	4.49	3.94	0.00	0.03	0.45	0.22	97.00	25
LBT-1 EMI-000726-8	74.34	0.02	11.99	0.11	1.24	0.01	0.25	4.51	3.78	0.02	0.01	0.28	0.23	96.79	25
LBT-1 EMI-000726-9	74.64	0.03	12.17	0.09	1.31	0.00	0.21	4.32	3.93	0.00	0.01	0.32	0.20	97.24	25
LBT-1 EMI-000726-10	74.43	0.06	11.83	0.07	1.21	0.00	0.23	4.14	4.08	0.00	0.00	0.28	0.23	96.57	25
LBT-1 EMI-000726-11	74.84	0.05	12.16	0.00	1.21	0.00	0.26	4.37	4.08	0.00	0.00	0.35	0.22	97.56	25
LBT-1 EMI-000726-12	74.74	0.00	11.94	0.06	1.25	0.00	0.25	4.62	4.11	0.00	0.00	0.25	0.18	97.39	25
LBT-1 EMI-000726-13	74.50	0.01	11.71	0.08	1.30	0.00	0.20	4.26	4.18	0.00	0.00	0.35	0.19	96.79	25
LBT-1 EMI-000726-14	73.88	0.07	11.86	0.08	1.24	0.00	0.22	4.44	4.10	0.00	0.02	0.03	0.19	96.12	25
LBT-1 EMI avg n=14	**74.31**	**0.04**	**11.97**	**0.06**	**1.23**	**0.00**	**0.23**	**4.36**	**3.94**	**0.01**	**0.01**	**0.27**	**0.21**	**96.63**	
Std. Dev.	**0.53**	**0.03**	**0.15**	**0.04**	**0.04**	**0.00**	**0.02**	**0.31**	**0.17**	**0.01**	**0.01**	**0.12**	**0.02**	**0.98**	

Appendix A. Results of MIBQ electron microprobe analyses.

Sample	SiO_2	TiO_2	Al_2O_3	MnO	FeO	MgO	CaO	Na_2O	K_2O	P_2O_5	SO_2	F	Cl	Total	Beam Size (μm)
Glass Standard															
vg-568-1	76.33	0.11	12.32	0.00	1.13	0.00	0.44	4.14	5.14	0.03	0.01	0.21	0.09	99.96	
vg-568-2	77.04	0.02	12.60	0.00	1.15	0.02	0.42	3.61	4.95	0.00	0.01	0.25	0.09	100.17	
vg-568-3	76.16	0.08	12.60	0.04	1.13	0.01	0.40	3.80	5.01	0.00	0.02	0.37	0.11	99.72	
vg-568-4	76.98	0.09	12.54	0.05	1.06	0.02	0.43	4.56	5.05	0.01	0.00	0.25	0.10	101.12	
vg-568-5	76.56	0.09	12.46	0.00	1.01	0.04	0.42	4.36	5.01	0.00	0.00	0.17	0.10	100.21	
vg-568-6	76.29	0.08	12.38	0.02	1.12	0.04	0.43	4.75	5.10	0.00	0.03	0.17	0.09	100.48	
vg-568-7	76.55	0.08	12.51	0.05	1.20	0.04	0.45	4.50	4.95	0.00	0.00	0.27	0.09	100.68	
vg-568-8	77.32	0.08	12.50	0.01	1.18	0.02	0.45	3.35	5.07	0.00	0.02	0.29	0.08	100.35	
vg-568-9	76.39	0.09	12.56	0.03	1.16	0.02	0.43	4.65	5.18	0.02	0.00	0.30	0.11	100.93	
vg-568-10	76.38	0.05	12.59	0.00	1.09	0.01	0.42	4.67	5.02	0.04	0.03	0.13	0.11	100.53	
vg-568-11	75.01	0.10	12.47	0.00	1.11	0.09	0.43	5.36	5.09	0.00	0.01	0.19	0.09	99.95	
vg-568-12	75.87	0.12	12.56	0.02	1.20	0.05	0.44	5.04	5.15	0.00	0.05	0.11	0.10	100.72	
vg-568 avg *n* =12	**76.41**	**0.08**	**12.51**	**0.02**	**1.13**	**0.03**	**0.43**	**4.40**	**5.06**	**0.01**	**0.02**	**0.23**	**0.10**	**100.40**	
Std. Dev.	**0.60**	**0.03**	**0.09**	**0.02**	**0.06**	**0.03**	**0.01**	**0.59**	**0.07**	**0.01**	**0.02**	**0.08**	**0.01**	**0.42**	
vg-568 certified value	76.71	0.12	12.06	0.03	1.23		0.50	3.75	4.89						

Notes:
Major element chemical data collected with an CAMECA SX-100 electron microprobe operating with a beam current of 20 nA and an acceleration voltage of 15 kV.
Details of analytical methods and reproduceability provided in text.

Appendix B. Results of $^{40}Ar/^{39}Ar$ MIBQ laser step-heating analyses.

Run ID	Power (Watts)	$^{40}Ar/^{39}Ar$	$^{37}Ar/^{39}Ar$	$^{36}Ar/^{39}Ar$ (x 10^{-3})	$^{39}Ar_K$ (x 10^{-16} mol)	K/Ca†	Cl/K§ (x 10^{-3})	$^{40}Ar^*$ (%)	^{39}Ar (%)	Age (Ma)	±2σ (Ma)
BT-1-MT; Bishop Tuff Minimally Treated Step-Heated Qtz, NM-109, L#=50401; J=0.000154254±0.12%, D=1.00531±0.00097											
50401-04A	1	1708.29	0.0478	5757.10	0.252	10.7	27.3	0.4	1.1	1.96	54.98
50401-04B	3	337.36	0.0349	1112.89	2.723	14.6	21.6	2.5	13.4	2.36	1.66
50401-04C	5	34.66	0.0379	96.84	6.356	13.5	24.0	17.4	42.1	1.68	0.11
50401-04D	7	12.93	0.0377	21.01	7.194	13.5	22.9	51.8	74.5	1.86	0.07
50401-04E	9	12.94	0.0357	19.15	3.535	14.3	23.4	56.1	90.4	2.02	0.13
50401-04F	10	15.23	0.0319	25.41	0.981	16.0	23.6	50.5	94.8	2.14	0.47
50401-04G	12	17.22	0.0324	32.52	0.650	15.7	26.3	44.1	97.8	2.11	0.71
50401-04H	13	18.14	0.0444	36.60	0.207	11.5	26.0	40.3	98.7	2.03	2.24
50401-04I	15	16.10	0.0649	22.40	0.177	7.9	31.5	58.7	99.5	2.63	2.63
50401-04J	15	13.55	0.1008	23.10	0.113	5.1	33.7	49.5	100.0	1.87	4.12
total gas age			n=10		22.188	13.8				1.90	1.00
plateau			n=10	steps A-J	22.188	13.8			100.0	1.85	0.06
MSWD=2.10											
BT-1-MG; Bishop Tuff 1 Hour Mill Grinder, Step-Heated Qtz, NM-109, L#=50584; J=0.000148751±0.12%, D=1.00977±0.00095											
50584-01A	1	8.86	0.0000	360.50	0.001	-	-	-	0.0	-26.41	329.05
50584-01B	3	15.59	0.0000	-	0.004	-	-	-	0.0	26.71	100.19
50584-01C	5	549.40	0.0000	1752.55	0.077	-	-	5.7	0.5	8.43	21.02
50584-01D	6	432.73	0.0393	1425.68	0.607	13.0	16.9	2.6	4.1	3.06	3.39
50584-01E	7	98.30	0.0490	301.74	1.927	10.4	20.7	9.3	15.7	2.45	0.39
50584-01F	8	26.58	0.0355	60.68	3.721	14.4	22.6	32.4	38.1	2.31	0.12
50584-01G	9	16.52	0.0388	24.93	7.831	13.1	23.0	55.3	85.3	2.45	0.05
50584-01H	*12*	*25.06*	*0.0219*	*45.89*	*2.083*	*23.3*	*22.5*	*45.8*	*97.8*	*3.08*	*0.18*
50584-01I	*14*	*46.37*	*0.0000*	*119.16*	*0.262*	-	*18.9*	*24.0*	*99.4*	*2.98*	*1.35*
50584-01J	*15*	*83.36*	*0.0000*	*214.02*	*0.104*	-	*7.1*	*24.1*	*100.0*	*5.38*	*3.66*
total gas age			n=10		16.617	14.1				2.58	0.43
plateau			n=7	steps A-G	14.168	13.1			85.3	2.43	0.05
MSWD=0.79											
BT-1-HF; Bishop Tuff 1 Hour Hydrofluoric Acid, Step-Heated Qtz, NM-109, L#=50582; J=0.000152447±0.12%, D=1.00977±0.00095											
50582-01A	1	23.56	0.1483	96.85	0.044	3.4	5.2	-	1.2	-1.40	6.21
50582-01B	3	26.10	0.4929	101.59	0.032	1.0	-	-	2.1	-1.07	8.33
50582-01C	5	40.65	0.7016	145.22	0.040	0.7	20.1	-	3.3	-0.62	7.32
50582-01D	6	210.59	0.0000	649.70	0.265	-	4.1	8.8	10.7	5.10	4.92
50582-01E	7	17.71	0.0503	14.88	0.878	10.2	20.3	75.1	35.2	3.65	0.28
50582-01F	8	15.68	0.0556	10.09	0.829	9.2	20.7	80.9	58.4	3.48	0.29
50582-01G	9	16.01	0.0468	6.25	0.686	10.9	25.3	88.3	77.6	3.89	0.34
50582-01H	12	19.76	0.0493	17.99	0.565	10.4	24.3	73.0	93.4	3.96	0.42
50582-01I	14	22.49	0.0798	27.59	0.141	6.4	21.9	63.7	97.3	3.93	1.67
50582-01J	15	87.39	0.1616	235.86	0.096	3.2	12.0	20.2	100.0	4.86	4.12
total gas age			n=10		3.576	9.4				3.70	1.00
plateau			n=10	steps A-J	3.576	9.4			100.0	3.70	0.16
MSWD=1.24											

Appendix B. Results of $^{40}Ar/^{39}Ar$ MIBQ laser step-heating analyses.

Run ID	Power (Watts)	$^{40}Ar/^{39}Ar$	$^{37}Ar/^{39}Ar$	$^{36}Ar/^{39}Ar$ (x 10^{-3})	$^{39}Ar_K$ (x 10^{-16} mol)	K/Ca†	Cl/K§ (x 10^{-3})	$^{40}Ar^*$ (%)	^{39}Ar (%)	Age (Ma)	±2σ (Ma)
UBT-1-MT; Upper Bandelier Tuff Minimally Treated Step-Heated Qtz, NM-109, L#=50402; J=0.000116717±0.15%, D=1.00531±0.00097											
50402-01A	1	1342.85	0.0311	4557.66	0.225	16.4	36.4	-	0.7	-0.84	36.05
50402-01B	3	235.68	0.0325	738.12	3.458	15.7	109.7	7.4	11.6	3.69	0.86
50402-01C	5	85.87	0.0288	224.60	11.432	17.7	118.5	22.7	47.5	4.10	0.14
50402-01D	*7*	*32.30*	*0.0291*	*35.28*	*11.446*	*17.5*	*118.8*	*67.7*	*83.4*	*4.60*	*0.04*
50402-01E	*9*	*37.62*	*0.0267*	*35.17*	*3.511*	*19.1*	*114.1*	*72.3*	*94.4*	*5.72*	*0.12*
50402-01F	*10*	*43.20*	*0.0184*	*40.68*	*0.662*	*27.7*	*105.6*	*72.1*	*96.5*	*6.55*	*0.56*
50402-01G	*12*	*46.40*	*0.0132*	*33.46*	*0.548*	*38.7*	*114.1*	*78.6*	*98.2*	*7.67*	*0.68*
50402-01H	*13*	*43.84*	*0.0000*	*37.16*	*0.220*	-	*120.2*	*74.9*	*98.9*	*6.90*	*1.65*
50402-01I	*15*	*42.23*	*0.0000*	*22.64*	*0.233*	-	*108.7*	*84.1*	*99.7*	*7.46*	*1.53*
50402-01J	*15*	*40.78*	*0.0000*	*13.75*	*0.107*	-	*95.6*	*90.0*	*100.0*	*7.71*	*3.28*
total gas age			n=10		31.843	17.8				4.54	0.48
plateau			n=3	steps A-C	15.116	17.2			47.5	4.09	0.07
MSWD=0.47											
UBT-1-MG; Upper Bandelier Tuff 1 Hour Mill Grinder, Step-Heated Qtz, NM-109, L#=50601; J=0.000132426±0.14%, D=1.01049±0.00145											
50601-01A	1	19.60	0.0000	-	0.008	-	-	-	0.1	17.46	40.05
50601-01B	3	22.03	0.0000	-	0.004	-	238.6	-	0.2	15.30	70.39
50601-01C	5	982.31	0.1659	3037.94	0.034	3.1	47.6	8.6	0.8	20.10	60.86
50601-01D	6	447.06	0.0345	1370.61	0.578	14.8	93.7	9.4	11.0	10.01	3.07
50601-01E	7	79.87	0.0348	147.45	1.854	14.7	110.6	45.4	43.8	8.65	0.27
50601-01F	*8*	*48.91*	*0.0240*	*58.78*	*2.122*	*21.3*	*111.4*	*64.4*	*81.3*	*7.51*	*0.18*
50601-01G	*9*	*59.57*	*0.0143*	*58.53*	*0.606*	*35.6*	*109.3*	*70.9*	*92.0*	*10.07*	*0.55*
50601-01H	*12*	*69.21*	*0.0257*	*101.95*	*0.363*	*19.8*	*103.3*	*56.4*	*98.4*	*9.31*	*0.92*
50601-01I	*14*	*96.95*	*0.1278*	*203.51*	*0.064*	*4.0*	*99.1*	*38.0*	*99.5*	*8.77*	*5.39*
50601-01J	*15*	*91.11*	*0.2754*	*134.77*	*0.028*	*1.9*	*80.2*	*56.3*	*100.0*	*12.21*	*12.04*
total gas age			n=10		5.662	19.5				8.70	1.20
plateau			n=5	steps A-E	2.479	14.5			43.8	8.66	0.14
MSWD=0.29											
UBT-1-HF; Upper Bandelier Tuff 1 Hour Hydrofluoric Acid, Step-Heated Qtz, NM-109, L#=50600; J=0.000128187±0.14%, D=1.00977±0.00095											
50600-01A	*1*	*4.17*	*0.0000*	-	*0.006*	-	*168.8*	-	*0.2*	*26.62*	*52.31*
50600-01B	*3*	-	*0.0000*	-	*0.005*	-	-	-	*0.4*	*24.79*	*58.77*
50600-01C	*5*	*89.81*	*0.0000*	*248.28*	*0.015*	-	-	*18.3*	*0.9*	*3.79*	*20.29*
50600-01D	*6*	*117.42*	*0.0422*	*114.81*	*0.144*	*12.1*	*49.7*	*71.1*	*5.7*	*19.20*	*2.41*
50600-01E	7	50.21	0.0012	4.05	0.849	428.1	102.5	97.6	34.0	11.29	0.27
50600-01F	8	51.09	0.0028	2.93	1.038	181.0	103.1	98.3	68.6	11.57	0.23
50600-01G	9	49.36	0.0000	6.79	0.471	-	102.3	95.9	84.3	10.91	0.48
50600-01H	12	53.87	0.0379	9.53	0.282	13.5	104.2	94.7	93.7	11.76	0.81
50600-01I	*14*	*43.61*	*0.0457*	*26.44*	*0.128*	*11.2*	*67.3*	*82.0*	*98.0*	*8.25*	*1.67*
50600-01J	*15*	*41.71*	*0.0000*	*48.64*	*0.060*	-	*18.6*	*65.5*	*100.0*	*6.31*	*3.59*
total gas age			n=10		2.997	188.2				11.54	0.87
plateau			n=4	steps E-H	2.639	210.6			88.1	11.41	0.16
MSWD=2.63											

Appendix B. Results of $^{40}Ar/^{39}Ar$ MIBQ laser step-heating analyses.

Run ID	Power (Watts)	$^{40}Ar/^{39}Ar$	$^{37}Ar/^{39}Ar$	$^{36}Ar/^{39}Ar$ (x 10^{-3})	$^{39}Ar_K$ (x 10^{-16} mol)	K/Ca†	Cl/K§ (x 10^{-3})	$^{40}Ar^*$ (%)	^{39}Ar (%)	Age (Ma)	±2σ (Ma)
LBT-1-MT; Lower Bandelier Tuff Minimally Treated Step-Heated Qtz, NM-109, L#=50400; J=0.000118166±0.15%, D=1.00531±0.00097											
50400-01A	1	1979.63	0.0381	6751.27	0.382	13.4	26.3	-	1.3	-3.29	41.66
50400-01B	3	424.18	0.0321	1392.56	3.180	15.9	66.3	3.0	12.4	2.70	1.69
50400-01C	5	51.75	0.0278	91.49	7.278	18.3	86.6	47.7	37.7	5.26	0.09
50400-01D	7	39.25	0.0267	25.80	11.048	19.1	90.1	80.5	76.0	6.73	0.05
50400-01E	9	43.70	0.0274	27.94	4.898	18.6	86.8	81.1	93.0	7.54	0.09
50400-01F	10	43.49	0.0190	24.41	1.238	26.9	80.0	83.4	97.3	7.71	0.30
50400-01G	12	52.54	0.0050	38.60	0.415	101.7	83.8	78.2	98.8	8.74	0.90
50400-01H	13	49.22	0.0348	30.74	0.154	14.7	81.7	81.5	99.3	8.53	2.37
50400-01I	15	67.41	0.0014	59.08	0.135	372.8	88.5	74.1	99.8	10.61	2.92
50400-01J	15	78.37	0.0000	107.95	0.061	-	65.5	59.3	100.0	9.87	6.93
total gas age			n=10		28.789	21.5				6.02	0.86
no plateau											
LBT-1-MG; Lower Bandelier Tuff 1 Hour Mill Grinder, Step-Heated Qtz, NM-109, L#=50593; J=0.000135605±0.13%, D=1.00977±0.00095											
50593-01A	1	24.68	0.0000	-	0.010	-	6.5	-	0.2	6.13	29.53
50593-01B	3	13.11	0.2823	12.84	0.009	1.8	0.4	71.0	0.3	2.28	31.87
50593-01C	5	746.06	0.0000	2396.60	0.076	-	7.8	5.1	1.6	9.23	25.83
50593-01D	6	432.20	0.0653	1318.92	0.777	7.8	67.8	9.8	14.8	10.35	2.87
50593-01E	7	89.01	0.0338	136.75	2.266	15.1	83.4	54.6	53.3	11.85	0.23
50593-01F	8	68.90	0.0236	72.72	1.805	21.6	81.5	68.8	83.9	11.56	0.22
50593-01G	*9*	*87.76*	*0.0000*	*105.64*	*0.460*	-	*73.3*	*64.4*	*91.7*	*13.77*	*0.79*
50593-01H	*12*	*98.46*	*0.0000*	*133.01*	*0.374*	-	*66.1*	*60.1*	*98.0*	*14.41*	*0.99*
50593-01I	*14*	*142.54*	*0.0000*	*280.11*	*0.079*	-	*59.6*	*41.9*	*99.4*	*14.56*	*4.92*
50593-01J	*15*	*207.46*	*0.0000*	*421.77*	*0.038*	-	*41.9*	*39.9*	*100.0*	*20.14*	*12.69*
total gas age			n=10		5.893	13.7				11.90	1.20
plateau			n=6	steps A-F	4.943	16.3			83.9	11.69	0.16
MSWD=0.94											
LBT-1-HF; Lower Bandelier Tuff 1 Hour Hydrofluoric Acid, Step-Heated Qtz, NM-109, L#=50591; J=0.000128352±0.14%, D=1.00977±0.00095											
50591-01A	*1*	*28.59*	*0.0000*	-	*0.005*	-	*176.0*	-	*0.2*	*23.52*	*54.91*
50591-01B	*3*	*20.47*	*0.0000*	-	*0.006*	-	-	-	*0.5*	*11.47*	*36.65*
50591-01C	*5*	*185.76*	*0.0000*	*577.05*	*0.032*	-	*2.6*	*8.2*	*2.1*	*3.52*	*18.38*
50591-01D	*6*	*122.48*	*0.1015*	*338.08*	*0.173*	*5.0*	*6.2*	*18.4*	*10.7*	*5.22*	*2.68*
50591-01E	7	66.44	0.0264	8.28	0.594	19.3	65.6	96.3	40.4	14.75	0.44
50591-01F	8	73.37	0.0051	2.97	0.755	99.3	75.6	98.8	78.0	16.70	0.35
50591-01G	9	73.08	0.0061	7.87	0.209	83.3	61.9	96.8	88.4	16.30	1.17
50591-01H	12	69.35	0.0000	10.65	0.136	-	52.4	95.4	95.1	15.26	1.77
50591-01I	14	59.41	0.0000	7.80	0.072	-	62.4	96.1	98.8	13.17	3.07
50591-01J	15	79.56	0.0000	142.13	0.025	-	38.4	47.2	100.0	8.67	10.64
total gas age			n=10		2.007	53.3				14.60	1.50
plateau			n=6	steps E-J	1.792	58.0			89.3	15.92	0.87
MSWD=10.77#											

Notes:

Isotopic ratios corrected for blank, radioactive decay, and mass discrimination, not corrected for interferring reactions.

Individual analyses show analytical error only; mean age errors also include error in J and irradiation parameters.

Analyses in italics are excluded excluded from plateau age calculations.

J-factors determined to a precision of ± 0.10% by CO_2 laser-fusion of 4 single crystals from each of 4 or 6 radial positions around the irradiation tray.

Age selection criteria: Plateaus are selected as the flattest portion of the age spectra that meet or approach the MSWD (mean standard weighted deviates) criteria of Mahon (1996). Plateau ages are calculated by weighting each analysis by the inverse of its variance. Errors are assigned to ages using the calculations of Taylor (1982). Where MSWD values lie outside the 95% confidence limits for n-1 degrees of freedom, the error is multiplied by the square root of the MSWD (Mahon, 1996).

Correction factors for interfering nuclear reactions were determined using K-glass and CaF_2 and are as follows:

$(^{39}Ar/^{37}Ar)_{Ca} = 0.00070 \pm 0.00005$

$(^{36}Ar/^{37}Ar)_{Ca} = 0.00026 \pm 0.00002$

$(^{38}Ar/^{39}Ar)_K = 0.0119$

$(^{40}Ar/^{39}Ar)_K = 0.0250 \pm 0.0050$.

Total system blank values: 2.9 x 10^{-16}, 4.8 x 10^{-18}, 7.0 x 10^{-19}, 2.1 x 10^{-18}, 2.7 x 10^{-18} at masses 40, 39, 38, 37, and 36 respectively.

†K/Ca=molar ratio calculated from reactor produced $^{39}Ar_K$ and $^{37}Ar_{Ca}$.

§Cl/K=molar ratio calculated from reactor produced $^{39}Ar_K$ and $^{38}Ar_{Cl}$.

#MSWD outside of 95% confidence interval.

n=number of analyses used for age calculations.

Appendix C. Results of $^{40}Ar/^{39}Ar$ MIBQ single-crystal laser-fusion analyses.

Run ID	$^{40}Ar/^{39}Ar$	$^{37}Ar/^{39}Ar$	$^{36}Ar/^{39}Ar$ (x 10^{-3})	$^{39}Ar_K$ (x 10^{-15} mol)	K/Ca†	Cl/K§ (x 10^{-3})	$^{40}Ar^*$ (%)	Age (Ma)	±2σ (Ma)
BT-1-MT; Bishop Tuff Minimally Treated Single Crystal Laser Fusion Qtz; NM-109, L#=50588; J=0.000137134±0.13%, D=1.00468±0.00093									
50588-05	27.48	0.0905	73.25	0.139	5.6	21.9	21.2	1.44	0.21
50588-11	60.64	0.1077	179.09	0.085	4.7	23.2	12.7	1.90	0.39
50588-14	41.12	0.1227	112.36	0.049	4.2	19.7	19.2	1.96	0.55
50588-12	76.28	0.1007	229.28	0.034	5.1	20.2	11.2	2.10	0.93
50588-03	17.99	0.0983	31.30	0.095	5.2	24.1	48.5	2.16	0.26
50588-15	40.61	0.0911	107.64	0.159	5.6	24.2	21.6	2.17	0.21
50588-04	62.02	0.1465	179.39	0.034	3.5	24.2	14.5	2.22	0.83
50588-13	23.77	0.3766	49.88	0.051	1.4	20.4	38.0	2.23	0.52
50588-07	25.41	0.0802	55.24	0.083	6.4	23.4	35.7	2.24	0.31
50588-09	19.03	0.1273	31.67	0.035	4.0	23.2	50.7	2.39	0.71
50588-10	32.64	0.0496	76.14	0.030	10.3	28.9	31.0	2.50	0.83
50588-01	68.38	0.0890	194.53	0.068	5.7	20.9	15.9	2.69	0.48
50588-02	46.84	0.2407	114.12	0.068	2.1	21.0	28.0	3.24	0.46
50588-08	124.07	0.1521	375.21	0.017	3.4	28.0	10.6	3.26	2.13
50588-06	89.53	0.1057	229.86	0.024	4.8	28.9	24.1	5.34	1.34
weighted mean ± Taylor error			n=15		4.8 ±4.1			2.52	0.27
MSWD=7.11#									
UBT-1-MT; Upper Bandelier Tuff Minimally Treated Single Crystal Laser Fusion Qtz; NM-109, L#=50606; J=0.000148929±0.12%, D=1.00468±0.00093									
50606-14	25.41	0.0785	57.01	0.032	6.5	99.8	33.6	2.29	0.87
50606-07	19.14	0.0102	28.09	0.054	50.0	101.3	56.5	2.90	0.50
50606-10	19.32	0.2330	24.68	0.074	2.2	90.8	62.2	3.23	0.39
50606-05	25.85	0.0675	45.95	0.062	7.6	99.2	47.4	3.29	0.44
50606-03	19.17	0.0807	21.80	0.049	6.3	101.7	66.3	3.41	0.55
50606-11	1345.98	0.3406	4510.38	0.057	1.5	71.0	1.0	3.53	22.05
50606-04	40.30	0.4031	88.90	0.011	1.3	90.7	34.8	3.77	2.48
50606-02	27.81	0.1066	42.09	0.051	4.8	104.3	55.2	4.12	0.53
50606-12	26.31	0.0936	31.52	0.035	5.4	96.4	64.5	4.56	0.79
50606-09	19.83	0.0261	5.43	0.030	19.5	93.9	91.8	4.88	0.89
50606-06	27.08	0.0321	14.42	0.042	15.9	115.0	84.2	6.12	0.65
50606-01	28.23	0.0735	16.39	0.093	6.9	101.2	82.8	6.27	0.30
50606-15	39.73	0.0539	44.25	0.053	9.5	100.1	67.0	7.14	0.56
50606-13	38.53	0.0537	9.23	0.091	9.5	100.6	92.9	9.59	0.32
50606-08	54.17	0.1018	21.03	0.061	5.0	96.4	88.5	12.83	0.48
weighted mean ± Taylor error			n=15		10.1 ±24.2			5.20	0.64
MSWD=12.33#									
LBT-1-MT; Lower Bandelier Tuff Minimally Treated Single Crystal Laser Fusion Qtz; NM-109; L#=50597; J=0.000146346±0.12%, D=1.00468±0.00093									
50597-06	50.36	0.0410	129.34	0.023	12.4	74.7	24.1	3.20	1.32
50597-07	61.80	0.2147	153.80	0.044	2.4	84.6	26.4	4.31	0.75
50597-13	116.55	0.0398	322.83	0.044	12.8	80.8	18.1	5.57	1.00
50597-10	59.66	0.0764	128.09	0.033	6.7	86.2	36.5	5.75	0.94
50597-15	105.72	0.1835	282.89	0.020	2.8	83.2	20.9	5.83	1.85
50597-12	115.51	0.0992	315.47	0.067	5.1	83.2	19.3	5.87	0.72
50597-14	39.93	0.0566	50.30	0.031	9.0	86.5	62.7	6.60	0.89
50597-05	39.28	0.0961	40.14	0.080	5.3	88.1	69.8	7.22	0.37
50597-01	57.44	0.3824	101.28	0.040	1.3	79.8	47.9	7.25	0.86
50597-08	84.08	0.1491	190.58	0.066	3.4	82.1	33.0	7.31	0.59
50597-04	46.07	0.1185	60.58	0.062	4.3	79.9	61.1	7.42	0.49
50597-02	84.73	0.2006	189.69	0.033	2.5	73.9	33.8	7.55	1.13
50597-03	85.99	0.2882	191.11	0.050	1.8	80.7	34.3	7.78	0.82
50597-11	73.95	0.1085	143.19	0.047	4.7	83.6	42.8	8.33	0.69
50597-09	56.10	0.0479	75.68	0.047	10.6	82.8	60.1	8.88	0.64
weighted mean ± Taylor error			n=15		5.7 ±7.7			6.59	1.59
MSWD=147.9#									

Appendix C. Results of $^{40}Ar/^{39}Ar$ MIBQ single-crystal laser-fusion analyses.

Notes:
Isotopic ratios corrected for blank, radioactive decay, and mass discrimination, not corrected for interferring reactions.
Individual analyses show analytical error only; mean age errors also include error in J and irradiation parameters.
Analyses in italics are excluded excluded from plateau age calculations.
J-factors determined to a precision of ± 0.10% by CO_2 laser-fusion of 4 single crystals from each of 4 or 6 radial positions around the irradiation tray.
Age selection criteria: Weighted mean ages are calculated by weighting each analysis by the inverse of its variance. Errors are assigned to ages using the calculations of Taylor (1982). Where MSWD values lie outside the 95% confidence limits for n-1 degrees of freedom, the error is multiplied by the square root of the MSWD (Mahon, 1996).
Correction factors for interfering nuclear reactions were determined using K-glass and CaF_2 and are as follows:
$(^{39}Ar/^{37}Ar)_{Ca}$ = 0.00070±0.00005
$(^{36}Ar/^{37}Ar)_{Ca}$ = 0.00026±0.00002
$(^{38}Ar/^{39}Ar)_{K}$ = 0.0119
$(^{40}Ar/^{39}Ar)_{K}$ = 0.0250±0.0050.
Total system blank values: 2.9 x 10^{-16}, 4.8 x 10^{-18}, 7.0 x 10^{-19}, 2.1 x 10^{-18}, 2.7 x 10^{-18} at masses 40, 39, 38, 37, and 36 respectively.
†K/Ca=molar ratio calculated from reactor produced $^{39}Ar_K$ and $^{37}Ar_{Ca}$.
§Cl/K=molar ratio calculated from reactor produced $^{39}Ar_K$ and $^{38}Ar_{Cl}$.
#MSWD outside of 95% confidence interval.
n=number of analyses used for age calculations.

Appendix D. Results of $^{40}Ar/^{39}Ar$ sanidine single-crystal laser-fusion analyses.

Run ID	$^{40}Ar/^{39}Ar$	$^{37}Ar/^{39}Ar$	$^{36}Ar/^{39}Ar$ (x 10^{-3})	$^{39}Ar_K$ (x 10^{-15} mol)	K/Ca †	$^{40}Ar^*$ (%)	Age (Ma)	±2σ (Ma)
BT-2; Bishop Tuff Plinian Sanidine, Single Crystal Laser Fusion San; NM-93, L#=9487; J=0.00077758±0.10%, D=1.00292±0.00118								
9487-07	0.7089	0.0066	0.5993	7.18	77.6	75.1	0.746	0.020
9487-01	0.7099	0.0071	0.5854	9.30	72.0	75.7	0.753	0.038
9487-03	0.7859	0.0089	0.8376	25.02	57.0	68.6	0.756	0.009
9487-02	0.6667	0.0071	0.4145	11.28	72.1	81.7	0.764	0.014
9487-12	0.6613	0.0072	0.3842	20.97	71.0	82.9	0.769	0.008
9487-05	0.7481	0.0066	0.6775	7.12	77.6	73.3	0.769	0.019
9487-09	0.8334	0.0128	0.9555	8.77	39.9	66.2	0.774	0.018
9487-08	0.7179	0.0098	0.5604	14.71	52.1	77.0	0.775	0.011
9487-14	0.6860	0.0068	0.4332	6.94	75.0	81.4	0.783	0.020
9487-10	0.8840	0.0068	1.0923	8.29	74.7	63.5	0.788	0.019
9487-13	0.8688	0.0068	1.0337	8.12	74.7	64.9	0.790	0.018
weighted mean ± Taylor error			n=11		67.6 ±24.7		0.768	0.004
MSWD=2.81#								
UBT-2, Upper Bandelier Tuff Plinian Sanidine, Single Crystal Laser Fusion San; NM-98, L#=9775; J=0.000765523±0.10%, D=1.00361±0.00157								
UBT-2, Upper Bandelier Tuff Plinian Sanidine, Single Crystal Laser Fusion San; NM-98, L#=9776; J=0.000763713±0.10%, D=1.00361±0.00157								
9776-07	0.9652	0.0091	0.2635	10.78	55.8	92.0	1.223	0.040
9776-02	1.2320	0.0087	1.1430	12.77	58.6	72.6	1.232	0.041
9775-02	0.9127	0.0093	0.0669	9.40	55.1	97.9	1.233	0.045
9775-01	0.9200	0.0086	0.0839	8.35	59.6	97.4	1.237	0.052
9776-06	1.1090	0.0091	0.6818	11.80	56.2	81.9	1.251	0.039
9776-08	0.9735	0.0090	0.1824	17.53	56.6	94.5	1.267	0.027
9776-03	1.3459	0.0089	1.4274	13.22	57.1	68.7	1.273	0.042
9775-12	1.0192	0.0111	0.3102	14.13	46.0	91.1	1.281	0.030
9775-06	1.0092	0.0089	0.2339	8.25	57.6	93.2	1.299	0.049
9775-09	0.9723	0.0083	0.0978	8.89	61.8	97.1	1.303	0.046
9775-04	0.9662	0.0090	0.0454	8.86	57.0	98.7	1.316	0.046
9775-10	1.1601	0.0085	0.6933	7.70	60.1	82.4	1.319	0.052
9775-05	1.0146	0.0092	0.1747	9.56	55.7	95.0	1.330	0.043
9775-03	0.9996	0.0092	0.1128	9.09	55.2	96.7	1.335	0.047
9776-05	1.1120	0.0090	0.4786	11.19	56.4	87.3	1.337	0.040
9776-04	1.0164	0.0095	0.1530	12.18	53.6	95.6	1.338	0.038
9776-09	1.0773	0.0086	0.3364	10.94	59.1	90.8	1.348	0.043
9775-11	0.9848	0.0092	-0.0182	6.26	55.6	100.6	1.368	0.063
9776-01	1.2454	0.0097	0.8109	11.66	52.8	80.8	1.386	0.042
9775-08	*1.1694*	*0.0099*	*0.2017*	*8.31*	*51.3*	*95.0*	*1.533*	*0.053*
weighted mean ± Taylor error			n=19		56.3 ±6.7		1.294	0.010
MSWD=5.19#								

Appendix D. Results of $^{40}Ar/^{39}Ar$ sanidine single-crystal laser-fusion analyses.

Run ID	$^{40}Ar/^{39}Ar$	$^{37}Ar/^{39}Ar$	$^{36}Ar/^{39}Ar$ (x 10^{-3})	$^{39}Ar_K$ (x 10^{-15} mol)	K/Ca †	$^{40}Ar^*$ (%)	Age (Ma)	±2σ (Ma)
LBT-2, Lower Bandelier Tuff Pumice Clast Conglomerate, Single Crystal Laser Fusion San; NM-98, L#=9778; J=0.00076167±0.10%, D=1.00361±0.00157								
LBT-2, Lower Bandelier Tuff Pumice Clast Conglomerate, Single Crystal Laser Fusion San; NM-98, L#=9779; J=0.00076196±0.10%, D=1.00361±0.00157								
LBT-2, Lower Bandelier Tuff Pumice Clast Conglomerate, Single Crystal Laser Fusion San; NM-98, L#=9780; J=0.000763018±0.10%, D=1.00361±0.00157								
9780-13	1.2191	0.0192	0.3857	8.64	26.6	90.8	1.522	0.046
9780-24	1.2237	0.0156	0.3483	4.37	32.7	91.7	1.543	0.090
9780-16	1.2050	0.0137	0.2791	3.59	37.1	93.2	1.546	0.109
9779-03	1.3854	0.0168	0.8831	7.63	30.3	81.2	1.546	0.053
9780-06	1.1983	0.0179	0.2468	6.23	28.6	94.0	1.550	0.063
9780-15	1.2444	0.0151	0.4001	2.16	33.7	90.6	1.551	0.182
9780-04	1.2372	0.0149	0.3713	4.36	34.3	91.2	1.553	0.090
9779-05	1.2305	0.0158	0.3359	5.33	32.2	92.0	1.556	0.073
9780-05	1.4205	0.0166	0.9785	3.33	30.8	79.7	1.558	0.118
9780-09	1.2073	0.0152	0.2541	8.80	33.6	93.9	1.559	0.046
9780-12	1.1987	0.0171	0.2140	3.27	29.9	94.8	1.564	0.120
9780-08	1.2710	0.0152	0.4548	1.52	33.6	89.5	1.565	0.254
9780-22	1.2112	0.0149	0.2368	8.33	34.3	94.3	1.571	0.047
9780-19	1.2673	0.0161	0.4246	7.82	31.7	90.2	1.572	0.051
9780-20	1.2760	0.0172	0.4533	8.36	29.6	89.6	1.573	0.048
9778-03	1.2578	0.0116	0.3708	5.49	43.8	91.3	1.578	0.082
9780-02	1.4140	0.0149	0.9053	4.50	34.3	81.1	1.579	0.088
9780-23	1.1797	0.0147	0.1066	6.26	34.6	97.4	1.581	0.063
9780-11	1.5784	0.0171	1.4533	7.26	29.9	72.9	1.582	0.057
9778-01	1.2499	0.0160	0.3046	8.47	31.9	92.9	1.594	0.052
9780-17	1.5372	0.0147	1.2782	2.38	34.8	75.5	1.597	0.166
9780-01	1.2481	0.0144	0.2828	3.65	35.4	93.4	1.604	0.107
9778-07	2.4149	0.0112	4.2129	12.85	45.7	48.5	1.608	0.056
9780-10	1.2888	0.0152	0.3982	1.81	33.6	90.9	1.613	0.218
9778-04	1.2302	0.0103	0.1825	6.83	49.7	95.7	1.617	0.062
9780-21	1.2077	0.0145	0.0901	2.69	35.1	97.9	1.626	0.143
9778-08	1.4269	0.0144	0.8149	13.18	35.3	83.2	1.630	0.035
9780-14	1.8802	0.0208	2.3574	3.62	24.6	63.0	1.631	0.111
9779-04	1.2354	0.0182	0.1596	2.69	28.0	96.3	1.634	0.144
9778-15	1.2595	0.0097	0.2055	9.78	52.6	95.2	1.647	0.045
9778-13	1.5108	0.0112	1.0471	11.62	45.5	79.6	1.651	0.043
9778-06	1.2334	0.0168	0.0613	14.16	30.3	98.6	1.671	0.031
9778-14	1.4201	0.0162	0.6916	9.43	31.5	85.7	1.671	0.048
9779-02	1.4815	0.0155	0.9006	3.08	32.9	82.1	1.671	0.153
9778-02	1.2657	0.0135	0.1391	10.57	37.9	96.8	1.683	0.042
9778-05	*1.9629*	*0.0206*	*2.3333*	*12.45*	*24.8*	*64.9*	*1.751*	*0.044*
9780-03	*1.3685*	*0.0158*	*0.2942*	*3.56*	*32.4*	*93.7*	*1.765*	*0.111*
9778-12	*1.6986*	*0.0176*	*1.2131*	*8.42*	*29.0*	*79.0*	*1.842*	*0.058*
weighted mean ± Taylor error			n=35		34.5 ±12.4		1.607	0.011
MSWD=2.66#								

Appendix D. Results of $^{40}Ar/^{39}Ar$ sanidine single-crystal laser-fusion analyses.

Notes:

Isotopic ratios corrected for blank, radioactive decay, and mass discrimination, not corrected for interferring reactions.

Individual analyses show analytical error only; mean age errors also include error in J and irradiation parameters.

Analyses in italics are excluded excluded from plateau age calculations.

J-factors determined to a precision of ± 0.10% by CO_2 laser-fusion of 4 single crystals from each of 4 or 6 radial positions around the irradiation tray.

Age selection criteria: Weighted mean ages are calculated by weighting each analysis by the inverse of its variance. Errors are assigned to ages using the calculations of Taylor (1982). Where MSWD values lie outside the 95% confidence limits for n-1 degrees of freedom, the error is multiplied by the square root of the MSWD (Mahon, 1996).

Correction factors for interfering nuclear reactions were determined using K-glass and CaF_2 and are as follows:

$(^{39}Ar/^{37}Ar)_{Ca} = 0.00070 \pm 0.00005$

$(^{36}Ar/^{37}Ar)_{Ca} = 0.00026 \pm 0.00002$

$(^{38}Ar/^{39}Ar)_{K} = 0.0119$

$(^{40}Ar/^{39}Ar)_{K} = 0.0002 \pm 0.0003$

Total system blank values: 2.9 x 10^{-16}, 4.8 x 10^{-18}, 7.0 x 10^{-19}, 2.1 x 10^{-18}, 2.7 x 10^{-18} at masses 40, 39, 38, 37, and 36 respectively.

†K/Ca=molar ratio calculated from reactor produced $^{39}Ar_K$ and $^{37}Ar_{Ca}$.

#MSWD outside of 95% confidence interval.

n=number of analyses used for age calculations.

Appendix E. Suggestions for future work.

The work presented here identifies more problems and poses more questions than are able to be solved or addressed within the scope of a single masters thesis. In this appendix, I have outlined several broad questions requiring the attention of future research and then subsequently propose a number of experiements that may help provide answers to these questions. All of the proposed studies involve the Bishop and Bandelier deposits, though additional silicic systems could certainly be added to provide independent constraints and demonstrate potential variable argon isotopic behavior from one magmatic system to another.

Questions:

1. What, if any, are the differences in $^{40}Ar/^{39}Ar$ distribution within MIBQ from plinian vs. ignimbrite deposits?

2. What are the $^{40}Ar/^{39}Ar$ compositions of matrix pumice?

3. What, if any, are the differences in $^{40}Ar/^{39}Ar$ distribution within sanidines from plinian vs. ignimbrite deposits?
   And, do sanidines from ignimbrite deposits have less $^{40}Ar_E$ in them than those in plinian deposits?

4. How heterogeneous are the TMI in MIBQ?

Potential Experimental Methods:

1. An answer to this question can potentially provide a key piece of information with which to test the MIBQ eruption degassing model I have presented here. Ignimbrites (particularly welded ignimbrites) should equilibrate $^{40}Ar_E$ with $^{40}Ar_{atm}$ to a higher degree as a result of heating in a post-eruptive volcanic pile. MIBQ separated from ignimbrite deposits should therefore more closely record eruption ages than those from plinian deposits. Preliminary results of J. Boyce (2000, pers. comm.) show that MIBQ from the Bishop Tuff ignimbrite yield apparent ages >9 Ma. This contrasts expectations based on the degassing model of this study. It is possible that this preliminary data may have problems with a phenomena referred to as "furnace memory." I suggest that laser step-heating and furnace step-heating studies be performed on MIBQ from ignimbrite deposits to test if these preliminary data are artifacts of "furnace memory." Such an experiment will also provide a critical test of the degassing model as mentioned previously. Lastly, the furnace step-heating data (performed under the right experimental condtions, i.e., clean crucible liner), because of precise temperature control, can be used to define Arrhenius arrays that should reproduce the data of Boyce et al. (2000). It is suggested that these step-heating experiments be performed on both MT- and HF-style aliquots of MIBQ.

2. It would be prudent to establish the $^{40}Ar/^{39}Ar$ compositions of matrix pumice. This might provide constraints on the $^{40}Ar/^{39}Ar$ compositions of the EMI end-member which were unobtainable from the data of this study. Laser step-heating (as opposed to laser-fusion) is recommended for this because if heterogeneous isotopic distribution should exist within matrix glass, it can be better characterized by step-heating. Also perhaps with a two- or three-step heating schedule, atmospheric argon associated with glass hydration might be removed early in the analysis. Moreover, laser step-heating is less time consuming than furnace step-heating and experimental conditions will be characterized by lower blanks.

3. The suggestion that sanidines from ignimbrite deposits might contain a more homogeneous argon isotopic distribution devoid of melt inclusion hosted $^{40}Ar_E$, when compared to sanidines from plinian deposits, should be statistically and quantitatively evaluated. All of the following single-crystal laser-fusion experiments should be performed at a constant and large n (~30). As a first step, I would suggest separating melt inclusion-free sanidines from both ignimbrite and plinian deposits.

It would also be useful to perform single-crystal laser-fusion studies on sanidines selected at random from both plinian and ignimbrite deposits. Such a random selecton would help to ensure a random distribution of melt inclusions throughout the analytical population in question. Comparisons can then be made between these separates, with respect to their weighted mean and/or isochron ages, to quantitatively and statistically assess the effects of $^{40}Ar_E$. It is stressed that irradiating these sanidine separates at a reactor which does not shield thermal neutrons will provide a more versatile dataset in the context of these experiments. One of the problems with irradiating sanidines at the University of Texas (as was done in this study) is the difficulty in estimating Cl concentrations. Esser et al. (1997) showed that melt inclusions from Mt. Erebus anorthoclase released nearly homogeneous $^{40}Ar_E/^{38}Ar_{Cl}$ ratios in vacuum step-heating experiments. These $^{40}Ar_E/^{38}Ar_{Cl}$ ratios are available for the MIBQ data of this study (as MIBQ were irradiated at the University of Michigan which does not shield thermal neutrons), and should sanidines contain similar $^{40}Ar_E/^{38}Ar_{Cl}$ concentrations, it would be possible to post analytically correct for excess argon. The potential problems with such a correction are: a) due to differences between MIBQ and sanidine retentivities, $^{40}Ar_E/^{38}Ar_{Cl}$ ratios and concentrations from MIBQ are not necessarily directly applicable to sanidine; and b) given that TMI are heterogeneous with repsect to $^{40}Ar_E$ as described in the text of this manuscript, such an $^{40}Ar_E/^{38}Ar_{Cl}$ ratio from MIBQ would only give a broad and mixed characterization of what melt inclusion hosted-$^{40}Ar_E$ compositions in sanidines might potentially be. Nevertheless this would be an interesting experiment that might yield a "$^{40}Ar_E$-corrected weighted-mean age" that could be statistically compared to sanidines from plinian and ignimbrite deposits. This data could also be compared to selected populations of sanidine without melt inclusions to test the hypothesis that such sanidines might be truly representative of an eruption age.

4. The degree of heterogeneity of $^{40}Ar_E$ among TMI can provide insights regarding the degassing behavior of MIBQ upon eruption. It can also, to some extent, test the reliability of a post analytically "$^{40}Ar_E$-corrected weighted mean age" which would be based on the assumption of a relatively homogeneous $^{40}Ar_E/^{38}Ar_{Cl}$ ratio from MIBQ TMI (as outlined in #3). To perform such a study requires an extremely low-blank, in-situ, microanalytical technique which is capable of extracting argon from individual trapped melt inclusions in MIBQ. Preliminary attempts have been made with a Nd-YAG UV laser at the NMGRL that show some promise. I suggest that future experiments with the UV laser might provide key answers and constraints regarding the problem of melt inclusion hosted-$^{40}Ar_E$.